ARMY RESEARCH LABORATORY

Volume I: Select Papers

ARL Summer Student Research Symposium

NOTICES

Disclaimers

The findings in this report are not to be construed as an official Department of the Army position unless so designated by other authorized documents.

Citation of manufacturer's or trade names does not constitute an official endorsement or approval of the use thereof.

Destroy this report when it is no longer needed. Do not return it to the originator.

Army Research Laboratory

Volume I: Select Papers

ARL Summer Student Research Symposium

REPORT DOCUMENTATION PAGE

Form Approved
OMB No. 0704-0188

1. REPORT DATE *(DD-MM-YYYY)*	2. REPORT TYPE	3. DATES COVERED (From - To)
August 2010	Final	

4. TITLE AND SUBTITLE	5a. CONTRACT NUMBER
Volume I: Select Papers	
	5b. GRANT NUMBER
	5c. PROGRAM ELEMENT NUMBER

6. AUTHOR(S)	5d. PROJECT NUMBER
ARL Summer Student Research Symposium	
	5e. TASK NUMBER
	5f. WORK UNIT NUMBER

7. PERFORMING ORGANIZATION NAME(S) AND ADDRESS(ES)	8. PERFORMING ORGANIZATION REPORT NUMBER
U.S. Army Research Laboratory 2800 Powder Mill Road Adelphi, MD 20783-1197	ARL-TM-2010

9. SPONSORING/MONITORING AGENCY NAME(S) AND ADDRESS(ES)	10. SPONSOR/MONITOR'S ACRONYM(S)
	11. SPONSOR/MONITOR'S REPORT NUMBER(S)

12. DISTRIBUTION/AVAILABILITY STATEMENT

Approved for public release; distribution unlimited.

13. SUPPLEMENTARY NOTES

14. ABSTRACT

The ARL Summer Student Research Symposium is an ARL Director's Award Program for all the students participating in various summer scholarship and contract activities across ARL. The goal of the program is to recognize and publicize exceptional achievements made by the students and their mentors in the support of Army science.

All college undergraduate and graduate students receiving research appointments and conducting summer studies at ARL are automatically enrolled in the symposium program. As an integral part of their summer study, all students are required to write a paper on their work which summarizes their major activity and its end product.

The program is conducted on two separate competitive levels: undergraduate and graduate. The format of the paper in both levels is the same. However, the evaluation will take into consideration the difference in the academic level of the students.

All students submitted their research paper for directorate review. Directorate judging panels selected one or two papers from each competition category for the laboratory-wide competition at the Summer Student Symposium on 10 August 2010.

Students selected by their directorate for competition participated in the one-day Summer Student Symposium on 10 August 2010. At the symposium the students presented their papers to the ARL Director and an ARL Fellows panel.

This volume of the Summer Student Symposium Proceedings contains the papers presented at the symposium.

15. SUBJECT TERMS

16. SECURITY CLASSIFICATION OF:			17. LIMITATION OF ABSTRACT	18. NUMBER OF PAGES	19a. NAME OF RESPONSIBLE PERSON
a. REPORT	b. ABSTRACT	c. THIS PAGE	UU	210	Vallen Emery
Unclassified	Unclassified	Unclassified			19b. TELEPHONE NUMBER *(Include area code)* (301) 394-3585

Contents

INTENTIONALLY LEFT BLANK.

Director's Foreword

The U.S. Army Research Laboratory (ARL) mission is to "Provide innovative science, technology, and analyses to enable full spectrum operations." As the Army's corporate laboratory, we provide the technological underpinnings critical to providing capabilities required by our current and future Soldiers.

Our nation is projected to experience a shortage of scientists and engineers. ARL recognizes the criticality of intellectual capital in generating capabilities for the Army. As the Army's corporate laboratory, addressing the projected shortfall is a key responsibility for us. We have, therefore, identified the nation's next generation of scientists and engineers as a key community of interest and have generated a robust educational outreach program to strengthen and support them. We have achieved many successes with this community. We believe that the breadth and depth of our outreach programs will have a significant positive effect on the participants, facilitating their journey toward becoming this Nation's next generation of scientists and engineers.

A fundamental component of our outreach program is to provide students research experiences at ARL. During the summer of 2010, we supported research experiences at ARL for over 150 undergraduate and graduate students. Each of these students writes a paper describing the results of the work they performed while at ARL. All of the papers were of high quality, but only a few could be presented at our student symposium. The abstracts for all papers prepared this summer are contained in this volume of the proceedings and they indicate that there were many excellent research projects with outstanding results. It is unfortunate that there was not enough time for us to have all of the papers presented. We would have enjoyed hearing them all.

We are very pleased to have hosted this outstanding group of students for the summer. It is our hope that they will continue their pursuit of technical degrees and will someday assist us in providing critical technologies for our Soldiers.

INTENTIONALLY LEFT BLANK.

Introduction

The ARL Summer Student Research Symposium is an ARL Director's Award Program for all the students participating in various summer scholarship and contract activities across ARL. The goal of the program is to recognize and publicize exceptional achievements made by the students and their mentors in the support of Army science.

All college undergraduate and graduate students receiving research appointments and conducting summer studies at ARL are automatically enrolled in the symposium program. As an integral part of their summer study, all students are expected to write a paper on their work which summarizes their major activity and its end product.

The program is conducted on two separate competitive levels: undergraduate and graduate. The format of the paper in both levels is the same. However, the evaluation will take into consideration the difference in the academic level of the students.

All students submitted their research paper for directorate review. Directorate judging panels selected one or two papers from each competition category for the laboratory-wide competition at the Summer Student Symposium on 10 August 2010.

Students selected by their directorate for competition participated in the one-day Summer Student Symposium on 10 August 2010. At the symposium, the students presented their papers to an audience of ARL scientists and engineers, including the ARL Director and an ARL Fellows panel.

This volume of the Summer Student Symposium Proceedings contains the papers presented at the symposium.

INTENTIONALLY LEFT BLANK.

Computational & Information Sciences Directorate (CISD)

INTENTIONALLY LEFT BLANK.

U.S. Army Research Laboratory
SUMMER RESEARCH TECHNICAL REPORT

Molecular Dynamics Study of the Orientation Dependence of Phase Transitions and Deformation Mechanisms in RDX

LYNN MUNDAY
PETER W CHUNG
CISD-CIH-C, ABERDEEN PROVING GROUNDS

Contents

List of Figures

List of Tables

Abstract

The concentration of energy and creation of hot spots in crystalline hexahydro-1,3,5-trinitro-1,3,5-s-triazine (RDX) is influenced by localized deformation features. This work presents results from molecular dynamics simulations of RDX using a flexible molecule potential energy function to elucidate the formation of these localized features. Equilibration simulations are used to validate the orthotropic α- and γ-RDX crystal structure and properties to experiment. The competition between cleavage fracture and dislocation nucleation at a crack tip in α-RDX is then evaluated using Rice's continuum formulation. Rice's analysis leads to a new material parameter, the unstable stacking fault energy, which is the maximum energy encountered for sliding on a slip plane from molecular dynamics simulations. This work determines the gamma surface, or stacking energy, on the (010) and (001) slip planes. Maximum saddle points from the gamma surface are compared to the free surface energy to determine the likely nature of deformation on these planes.

Acknowledgments

I wish to acknowledge the mentorship of Peter Chung.

1. Introduction/Background

The first step towards developing insensitive munitions is uncovering and understanding the subcontinuum features and mechanisms of the constituent materials that make up the energetic fill. Identifying structure-property relationships and mechanisms associated with inelastic response due to loads is critical for building up a first-principles description of initiation and failure, which, in turn, can help designers and engineers develop munitions that are more effective in their missions but safer to handle. Today, owing to the confluence of high rate physics, interdisciplinary effects, and the imperfections of the material at atomistic scales, it still remains unknown precisely what leads to initiation of energetic materials. Though many events, both deterministic and stochastic, are believed to be involved, their precise sequence and relative contributions to the final outcome are still largely unknown.

The energetic fill is a composite structure of energetic crystals, such as crystalline hexahydro-1,3,5-trinitro-1,3,5-s-triazine (RDX), encased in a plastic binder material. It is generally agreed upon that decomposition of the energetic fill is the culmination of micron-sized reactions, called hot spots, that result from shockwave interactions and dynamic localization phenomena in the heterogeneous composition of the explosive fill. Heterogeneities in the fill and its composite structure come in the form of voids, grain boundaries, multimaterial interfaces, and crystal orientation mismatches. The mechanism leading to localization of energy and decomposition in single crystals of energetic material free of heterogeneities is unclear. Armstrong (*3*) proposes that pile-ups of dislocations are suddenly released as an avalanche of localized deformation and available energy for adiabatic heating, leading to the nucleation of hot spots. For the energetic crystal pentaerythritol tetranitrate (PETN), Dick and Ritchie (*4*) suggested that the complex structure of the molecule sterically hindered displacement on slip planes and led to deformed molecules, whose bonds were easily broken. Both models are not mutually exclusive: steric hindrance may aid in the pile up of dislocations where the result could be dislocation avalanches and fracture, or planes of highly resolved shear stresses and deformed molecules. However, there is a lack of experimental observations made of the deformation mechanisms in molecular crystals to provide conclusive evidence as to which mechanism is dominant.

In this work, molecular dynamics will be used to study the atomistic deformation features of RDX to provide a mechanistic basis for its brittle nature and a description of operable deformation mechanisms. We will present calculations and their analyses that clarify the competitive balance between dislocation nucleation and cleavage at crack tips in RDX. Dislocation emission competes with Griffith cleavage near crack tips in much the same way as ductility and brittleness in metals have long been studied. Limited dislocation activity at the crack tip becomes entangled by the low symmetry crystal, and complex molecule shape and subsequent deformation may lead to an avalanche of localized dislocations and fracture or large

shear stresses sufficient for molecule conformational changes. Using nanoindentation, Ramos et al. (*5*) made experimental observations of limited plastic slip on the slip plane, followed by fracture at low loads. From their work, they were able to determine the slip systems, but the cause of the low fracture threshold was unresolved. Atomistic level simulations of these experimental slip and cleavage planes will provide missing information on the mechanism of slip and the low fracture strength. The atomistic information will be described in a continuum context developed by Rice (*2*) to evaluate the competition between cleavage fracture and dislocation nucleation at crack tips. The model uses an interplanar potential to relate the continuum shear stress to the atomic displacement as the boundary condition to be satisfied in an elastic solution of a traction free crack. Rice's analysis leads to a new material parameter, the unstable stacking fault energy, which is the maximum energy encountered for sliding blocks of material past one another on a slip plane. The unstable stacking fault energy cannot be directly measured by experiment, but is derivable from atomistic simulations of stacking faults. Rice's model will provide a mechanistic description for RDX's observed brittle nature.

The anisotropic material properties and unstable stacking fault energies for RDX will be determined from molecular dynamics simulations using a potential energy function developed by Smith and Bharadwaj (SB) (*6*) for similar nitramines such as HMX. The SB potential describes intramolecular bonded atomic interactions and nonbonded interactions for repulsion/dispersion and electrostatics. The potential is validated by reproducing experimental RDX material properties and structural information for the ambient condition α-RDX phase and the high pressure γ-RDX phase. Aided by high performance computing, these calculations will yield for the first time categorical information about the slip systems likely to be activated during plastic deformation, thereby providing basic material understanding of processes that may lead to hot spot formation and initiation of RDX.

2. Calculations

Smith et al. (*6*) used quantum mechanics calculations to parameterize nitramide and dimethylnitramine (DMNA) shown in figure 1(a) and (b) to develop classical intramolecular bond potentials commonly used in molecular dynamics. Nitramide and DMNA are similar in structure to the nitroamino functional group shown in figure 1(a) that makes up both HMX and RDX. Due to these similarities, a flexible potential developed for DMNA provides a building block to a flexible molecular potential for the more complex RDX and HMX molecules.
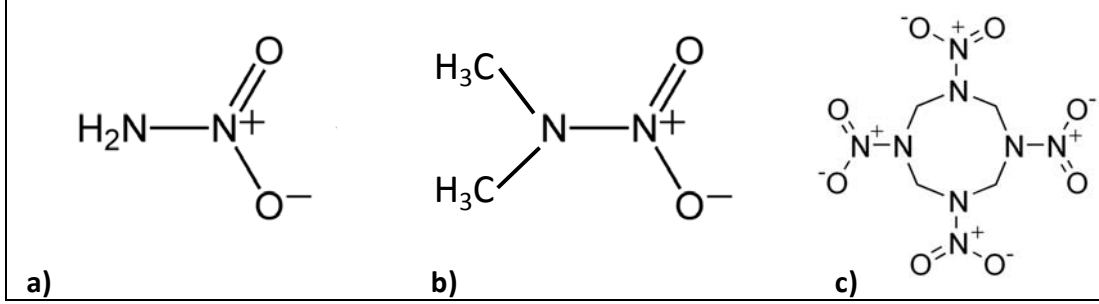
Figure 1. Chemical structure representation of (a) nitramide (b) dimethylnitramine, and (c) HMX.

The quantum mechanics data for DMNA was used to fit a bonded potential energy function containing harmonic bond forces, harmonic bending forces, cosine series torsion/dihedral forces, and out-of-plane bending forces of the O-N-O group, with the N-N bond modeled as a harmonic improper dihedral. The improper dihedral relates the motion of the two nitrogens by harmonic torsion about an axis between the two oxygen atoms, which works to keep the N-N bond in-plane with the O-N-O group. The nonbonded atomic interactions were modeled with an exponential-6 repulsion/dispersion model, with parameters given in other work. The partial charges for Coulombic interactions were found by fitting an electrostatic potential at a grid of point values from the quantum mechanics simulations. Simulations using the DMNA potential are shown to reproduce experimental gas phase peaks on the radial distribution function for atomic pairs and liquid phase vapor pressure, volume, and temperature properties. The liquid phase simulations required the partial charges to be increased by 25% to reproduce experimental results.

SB (*1*) assumed that all valence and dispersion/repulsion terms found for the much simpler DMNA molecule were directly transferable to the potential used for HMX. Additional valence parameters were then determined for HMX bonds that do not occur in DMNA, namely the N-C-N bend and C-N-C-N dihedral angles of the ring. The potential includes nonbonded coulombic and dispersion/repulsion interactions between all atoms separated by three or more bonds, including those connected by 1-4 dihedrals. Partial charges for the HMX model were refit to reproduce a grid of quantum mechanics data points for HMX, with the constraint that "like" atoms have equal charges. The SB flexible molecule potential was used to find the experimentally unavailable thermal conductivity, shear viscosity, and self-diffusion coefficients for the liquid HMX temperature domain $550 < T < 800$ K, which are all important material properties for large length and time scale constitutive models used in continuum hydrodynamic codes (*7*). The SB potential was then used to model crystalline HMX in the β-, α-, and δ-phases stable at ambient conditions, which differ by molecular packing and molecule conformation (*8*). Bedrov et al. give the full potential, U, used for crystalline HMX as

$$U = 0.5K_{ij}^{S}\left(r_{ij} - r_{ij}^{0}\right)^{2} + 0.5K_{ijk}^{B}\left(\theta_{ijk} - \theta_{ijk}^{0}\right)^{2} + 0.5K_{ijkl}^{T}\left[1 - cos\left(n\varphi_{ijkl}\right)\right]$$

$$+0.5K_{ijkl}^{D}\varphi_{ijkl}^{2} + A_{ij}exp\left(-B_{ij}r_{ij}\right) - \frac{C_{ij}}{r_{ij}^{6}} + k_{e}\frac{q_{i}q_{j}}{r_{ij}} \tag{1}$$

with parameters listed in table 1. This exact form of the SB potential and parameter set from table 1 is used to model crystalline RDX in this work.

Table 1. Smith and Bharadwaj potential parameters for HMX/RDX.

Bond stretches, $U = 0.5K_{ij}^S\left(r_{ij} - r_{ij}^0\right)^2$		
Bond type	K_{ij}^S (kcal/mol/Å^2)	r_{ij}^0 (Å)
O-N	1990.1	1.23
N-N	991.7	1.36
N-C	672.1	1.44
C-H	641.6	1.09
Valence Bends, $U = 0.5K_{ijk}^B\left(\theta_{ijk} - \theta_{ijk}^0\right)^2$		
Bend type	K_{ijk}^B (kcal/mol/rad^2)	θ_{ijk}^0 (rad)
O-N-O	125.0	2.1104
O-N-N	125.0	1.8754
N-N-C	130.0	1.6723
C-N-C	70.0	1.843
N-C-H	86.4	1.8676
H-C-H	77.0	1.8938
N-C-N	70.0	1.9289
Torsions, $U = 0.5K_{ijkl}^T\left[1 - \cos\left(n\phi_{ijkl}\right)\right]$		
Torsion Type	K_{ijkl}^T (kcal/mol)	n
O-N-N-C	8.45	2
O-N-N-C	0.79	4
O-N-N-C	0.004	8
H-C-N-C	-0.16	3
C-N-C-N	3.30	1
C-N-C-N	-1.61	2
C-N-C-N	0.11	3

Out of plane bends $U = 0.5K_{ijk}^D\phi_{jikl}^2$			
Out-of-plane bend type	K_{ijk}^D (kcal/mol/rad^2)		
C-N-C…*N	8.0	Where …*N is the atom kept in-plane	
O-N-O…*N	89.3		
van-der-Waals interactions, $U = A_{ij}\exp\left(-B_{ij}r_{ij}\right) - C_{ij}/r_{ij}^6$			
Atoms pair type	A_{ij} (kcal/mol)	B_{ij} (Å^{-1})	C_{ij} (kcal/mol Å^6)
C⋯C	14976.0	3.090	640.8
C⋯H	4320.0	3.415	138.2
C⋯N	30183.57	3.435	566.03
C⋯O	33702.4	3.576	505.6
H⋯H	2649.7	3.740	27.4
H⋯N	12695.88	3.760	116.96
H⋯O	14175.97	3.901	104.46
N⋯N	60833.9	3.780	500.0

N···O	67925.95	3.921	446.6
O···O	75844.8	4.063	398.9

Atomic partial charges	
Atom type	*Q*
C	-0.5400
N(amine)	0.056375
N(nitro)	0.860625
O	-.458500
H	0.270000

Cawkwell et al. (*9*) demonstrate the transferability of the SB potential given in table 1 by applying it directly to simulations of α-RDX under shock loading. The ambient condition thermomechanical properties, like the coefficient of thermal expansion, bulk modulus, and elastic constants for α-RDX, are not calculated, but the ambient lattice constants are reported and shown to be within 1.7% of experimental. The simulations use a shock front absorbing boundary layer to model viscous heating in shear bands, molecule structure, and crystal order in the amorphous shear band region. The simulations of Cawkwell et al. are compared to RDX simulations by Bedrov et al. (*10*) using the SB potential with a modified thermostat and barostat that enforce the Hugoniot shock conditions of a stationary shock wave for an applied uniaxial pressure.

The molecular dynamics package DL-Poly 2.20 (*11*) was used in this work to test the application of the SB Flexible Molecular potential (*1*) for the crystalline phases of α-RDX. We performed simulations to check that the potential recreated the proper crystal structure of α-RDX by comparing time averaged atomic position data from the simulations to experimental structural data given by Choi and Prince (*12*). The initial atomic coordinates for the α-RDX simulations were found by applying the Pbca space group symmetry operations to the asymmetric molecule coordinates given by Choi and Prince. The initial configurations for the γ-RDX simulations are those given by Davidson et al. for γ-RDX unit cell (*13*). The unit cell was then copied and translated to create a 2x3x3 crystal lattice in the (a, b, c) directions, respectively. The 2x3x3 RDX crystal contains 18 unit cells, 144 molecules, and 3,024 atoms. Parallelepiped periodic boundary conditions are used in the simulations, which allow for non-orthogonal lattice vectors of different lengths. Periodic boundary conditions are used to simulate an infinite crystal in all directions in order to get bulk thermodynamic properties free from the effects of surfaces.

The real space cut-off for the non-bonded Van der Waals and electrostatic interactions was set to 10 Å, which is large enough to allow for interactions between nearest neighbor molecules. The smallest simulation cell dimension must be at least twice as large as the 10 Å real space cut-off requiring a 2x3x3 unit cell crystal. In DL-POLY, a long range correction to the potential energy is applied to the short range van der Waals interactions to account for the attractive forces between atoms at distances greater than the real space cut-off. The long-range electrostatic

interactions are calculated using the Ewald sum method, which splits the potential up into two parts: atoms separated by a distance less than the cut-off are treated using a direct Coulomb sum, and atoms separated at distances larger than the cut-off are treated using a Fourier series sum in reciprocal space. In this work, DL-POLY is used to automatically set the Ewald parameters by specifying the precision of the relative error in the convergence of the real space sum to 0.3e-6. DL-POLY uses the relative error to automatically optimize the reciprocal space **k** vectors and the Ewald convergence parameter. In these simulations, the Ewald sum is shown to be adequately converged by checking that the Coulombic virial is the negative of the Coulombic energy.

The simulations were run using the verlet leapfrog time integrator. The highest vibrational frequency in the crystal is the C-H bond stretch, which has a period of approximately 12fs. In order to conserve the total system energy, approximately 10 integration steps should be taken per period, and in this work, a 0.75-fs timestep was used. This integration step could have been increased by treating the C-H bond as rigid, which may be done in future work.

All simulations in this work use the Nose-Hoover thermostat to control the simulation temperature. The Nose-Hoover thermostat functions by scaling the velocity using a scalar friction-like term that is coupled to an outside heat bath. For these simulations the temperature is set to T=300K. The coupling time constant for the thermostat in these simulations is 1.0 ps, which is related to the thermostat's "effective" mass.

This work contains both constant pressure/temperature (NPT) and constant volume/temperature (NVT) simulations. In the constant pressure simulations, the pressure is controlled with a barostat coupled to the thermostat through a modification of the equations of motion. The barostat controls the size and shape of the simulation cell to maintain the prescribed pressure. The barostat is applied as a friction-like term that scales the velocity and simulation cell size and shape. In an isobaric-isothermal simulation (NPT), the pressure is controlled by a scalar friction term scaling the cell shape. This work uses an iso-stress barostat (NST), which uses a second order tensor friction term that scales the shape and size of the simulation cell independently. The NST with the parallelepiped periodic boundary conditions allows for the simulation to proceed under the least geometrically constrained boundary conditions, and to reach an equilibrated structure predicted by the molecular potential at the applied temperature and pressure. The barostat coupling time in these simulations is set to 1.0 ps, which is related to the barostat's "effective" mass.

All simulations are started with an initial 7.5 ps equilibration period, where the random velocities used to seed the simulation are scaled every five integration steps to maintain the correct temperature. Total system energy is not conserved during this part of the simulation. After equilibration, the temperature scaling is turned off and the system evolves according to the equations of motions in their respective ensembles. This period is referred to as thermalizing in this work, and during this period the ensemble energy is conserved, and meaningful time averaged values and standard deviations are collected.

We performed two separate sets of NST simulations, starting at two different states to study effect of pressure on RDX. The first set started in the ambient α-RDX crystal configuration given by Choi and Prince (12) at P=1 atm and T=300 K, and the pressure is incrementally increased from 0.0–5.2 GPa in increments of 0.5GPa. The second set of simulations starts in the γ-RDX configuration given by Davidson et al. (13) at P=5.2 GPa and T=300 K, and the pressure is incrementally decreased from 5.2–0.0 GPa in increments of 0.5 GPa. The final atomic configuration and lattice vectors from the subsequent pressure simulation are used as the initial conditions at the new pressure. Each simulation is equilibrated for 7.5 ps and thermalized for 100 ps.

Isostrain NVT simulations were also performed here to study the orientational dependence of the system state to applied uniaxial strain. The system was strained by applying displacements to molecule centers of mass and lattice vectors according to the Lagrange strain description. The strain components, E_{11}, E_{22} and E_{33}, were incremented individually, requiring three separate sets of simulations. The thermalized average lattice vectors and atomic configuration from the NST simulations for T=300 K and P=0 for α-RDX, or P=5.2 GPa for γ-RDX, were used as the initial zero-strained configuration. The strain was incrementally increased from the subsequent steps final atomic configuration in strain increments of 1% up to 10% strain. Each simulation is equilibrated for 7.5 ps and thermalized for 75 ps.

A third set of NVT annealing simulations were done to study the effect of atomic disregistry or stacking mismatch on α-RDX slip planes. During the NVT annealing process, the system was thermalized to 25 K for 100 timesteps, after which the force is minimized using conjugate gradient, and then re-thermalized and minimized. This thermalize-minimize process is done 20 times, and the minimum energy configuration of these cycles is used for postprocessing. The initial configurations for these simulations come from annealing a 3x3x3 α-RDX system with initial coordinates from Choi and Prince (12). The 3x3x3 a-RDX lattice is then used to create a sandwich structure containing 30 unit cells in the direction normal to the slip plane, with the atomic positions of the top 14 and bottom 14 unit cells frozen in place. A 4 nm vaccum layer is added to the top of the 30 unit cells. The atomic positions of the unit cells above the slip plane are then shifted by increments of $1/10^{th}$ of a unit cell to create a grid of 100 configurations shifted in the slip plane. The simulation uses three-dimensional (3-D) orthorhombic periodic boundary conditions. The single layers of flexible cells above and below the slip plane are allowed to rotate and translate, and their intramolecular degrees of freedom are allowed to relax during the thermalization and minimization procedure, hopefully not getting trapped in a local minimum and relaxing to the global minimum. The frozen cells are used simulate bulk material by shielding the flexible unit cells from the free surfaces, and also to constrain the molecule center of mass motion to be mostly normal to the slip plane.

3. Results and Discussion

3.1 NST Pressurization Simulations

The NST simulations in this work are used to study the effect of pressure on the bulk crystal at constant temperature. Experiments and simulations run under these conditions are used to find the bulk modulus, B, of the material given by

$$B = -V \left(\frac{\partial P}{\partial V} \right)_T,$$

(2)

where V is the volume, P is the pressure, and T is the temperature. The bulk modulus is an intensive thermodynamic material property that provides a scalar measure of the crystal's volumetric response to pressure. In this work, the isothermal pressure versus volume data from simulation, shown in figure 2, is fit to the third order Birch-Murnaghan equation of state (BMEOS) to find the bulk modulus and its derivative (*14*) given by

$$P(V) = \frac{3B_o}{2} \left[\left(\frac{V_o}{V} \right)^{7/3} - \left(\frac{V_o}{V} \right)^{5/3} \right] \left\{ 1 + \frac{3}{4} (B'_o - 4) \left[\left(\frac{V_o}{V} \right)^{-2/3} - 1 \right] \right\},$$

(3)

where V_o is the volume at zero pressure, and B_o and B'_o are the bulk modulus and its derivative at zero pressure. This method gives the bulk modulus at zero pressure and is only applied to α-RDX data shown by the filled symbols. Values for B_o and B'_o are given in table 2, and are shown to be in agreement with experimental values.
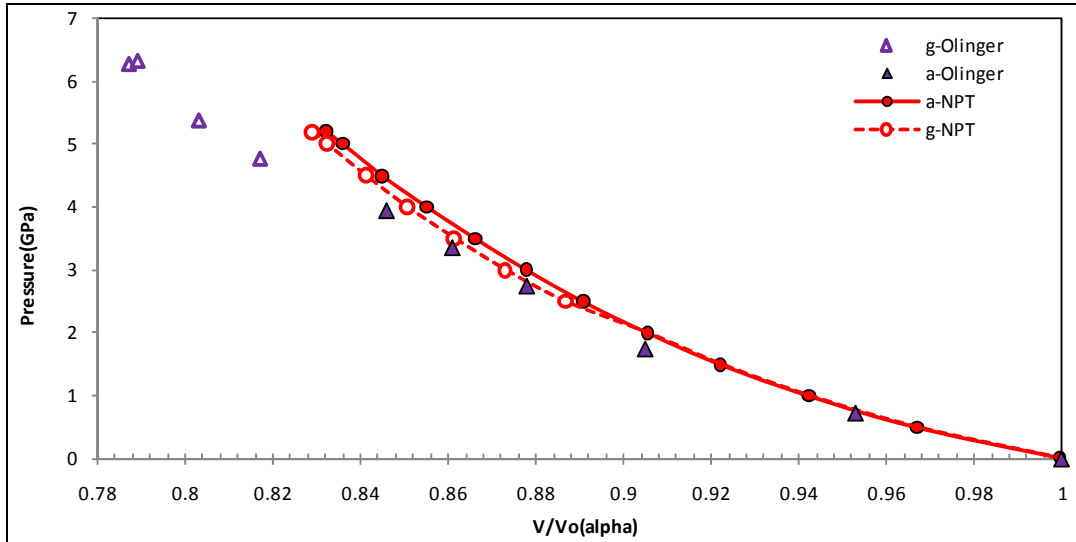
Figure 2. Pressure versus normalized volume. Circles are simulation results, triangles are experimental results experiement (*15*). Filled symbols are for α–RDX and unfilled symbols are for γ–RDX. Lines connecting simulation data points are only to highlight the phase transition for γ– to α–RDX.

18

Table 2. Birch-Murnaghan equation of state parameters.

α-RDX 3rd order BMEOS parameters

	P range (Gpa)	B_o(GPa)	B_o'	V_o(Å^3)
This work	0-15	13.0	9.2	1634.4
Olinger[a]	0-3.95	12.1	8.6	1641
Davidson[b]	--	9.8	11.4	1614.1

[a]Olinger et al. Ref. (15) [b]Davidson et al. Ref. (13)

A phase transition from α- to γ-RDX is reported by Davidson et al. (*13*) to occur at 3.9 GPa. The experimental isothermal compression data of Olinger et al. (*15*), highlighted by the triangle data points in figure 2, show the phase transition to occur between 4 and 5 GPa. Two separate curves develop for the simulation data in figure 2 for pressures above 2GPa. The compression simulation of α-RDX, shown by the solid line and filled circles, does not show a kink in the volumetric compression data, and a phase transition is likely not occuring. A small kink develops in the decompression simulation of γ-RDX, shown by the converging of the hollow circles and dashed line with the solid line of α-RDX, between 2.5 and 2 GPa. The kink signifies the phase transition between the thermalized γ- and α-RDX phases found from simulation. A much larger volume change occurs experimentally than that observed from the simulations.

The accuracy with which the SB potential predicts the lattice constants for the α- and γ-RDX phases is presented in figure 3 and tabulated in table 3. The point of comparison for α-RDX is the ambient state at P=0 and T=300 K, which was the state measured experimentally by Choi and Prince (*12*). The γ-RDX point of comparison is P=5.2 and T=300 K, the experimental conditions for the reported γ-RDX structure of Davidson et al. (*13*).
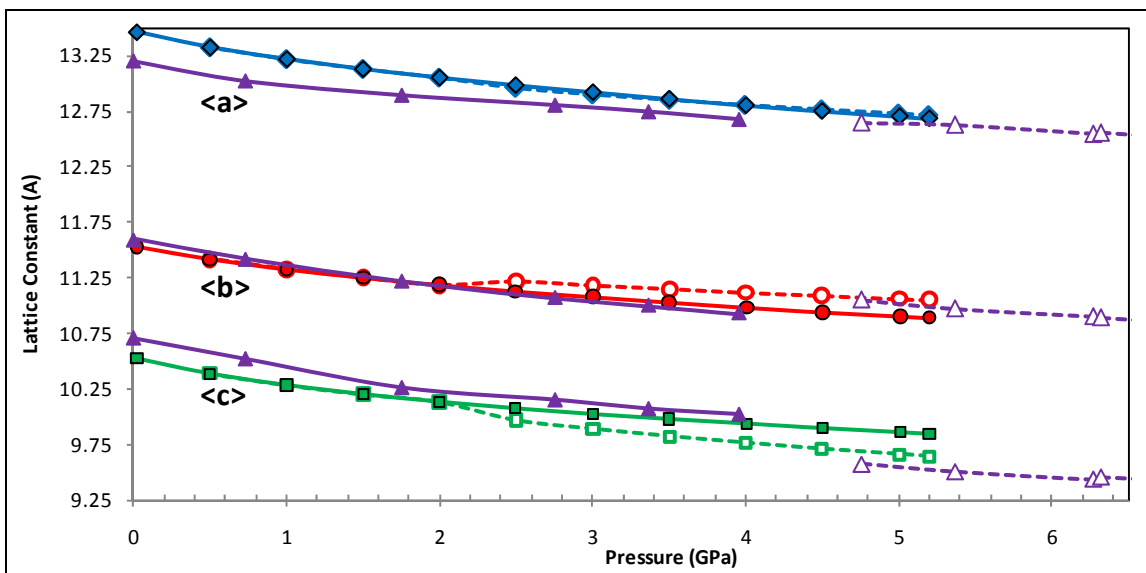
Figure 3. Lattice constants versus pressure. Diamonds (a), circles (b), and squares (c) are results from simulations; triangles are from experiment (*15*). Filled symbols are for α−RDX and unfilled symbols are for γ−RDX. Lines connecting simulation data points are only to highlight the phase transition for γ− to α−RDX.

Table 3. Average lattice constants and volume. Percent error compared to experiment in parentheses.

	Lattice Dimensions			
	$<a>$ (A)	$<b>$ (A)	$<c>$ (A)	$<V>$ (A^3)
-Exptl[a]	13.182	11.574	10.709	1633.8
-This work	13.446 (2.00%)	11.531 (-0.37%)	10.534 (-1.63%)	1633.3 (-0.03%)
-SAPT[b](298)	13.259 (0.58%)	11.634 (0.52%)	10.754 (0.42%)	1658.9 (1.54%)
-Exptl[c]	12.565	10.930	9.477	1301.5
-This work	12.685 (1.0%)	11.063 (1.2%)	9.644 (-1.8%)	1353.3 (4.0%)

[a]Choi, Prince (*12*)   [b]Podesczwa, Rice, Szalewicz (*16*) [c]Davidson et al. (*13*)

The α-RDX lattice constants, shown by the filled symbols and solid line, are overpredicted in the a-direction, but, volumetrically, this is balanced out by the underprediction in the c-direction. There is also not a sharp kink in the a-RDX lattice constants, signifying the lack of a phase transition. The phase transition in γ-RDX simulations, shown by the unfilled symbols and dashed lines, is apparent in the lattice constants by the divergence of the dashed and solid lines at P > 2 GPa. The γ-RDX phase more closely matches the experimental data points than the α-RDX simulations. Across the phase transition, the γ-RDX simulations show a decrease in the c-direction, an increase in the b-direction, and little change in the a-direction, all of which are observed experimentally. The inability of the SB potential to capture the large volume change across the phase transition in figure 2 is caused by the errors in α-RDX lattice constants.

The Radial Distribution Function (RDF) is also used here to determine the phase of the simulations due to uncertainty seen in volumetric data in figure 2 and lattice constants in figure 3 for the α- and γ-RDX phases. The RDF is used to plot the molecular density as a function of distance from a particular atom. The RDF is scaled by the molecule density and, so, will approach unity at large distances. Spikes in the RDF signify atoms. The RDF in this work was created from 30 realizations of the configuration during the thermalization. The experimental RDFs shown by the dashed lines in figure 4 show sharp peak because the molecules lack thermal vibrations. Thermalizations of the states that the α- and γ-RDX crystal structure were experimentally determined at are shown by the solid colored line, T=300K, P=0 for α-RDX; by the solid blue line at the bottom; and, P=5.2GPa for γ-RDX, shown by the solid red line at the top. Figure 4 shows the RDFs for the pressure data points plotted in figures 2 and 3 for the pressurization of α-RDX. The pressure of each RDF is labeled in figure 4.
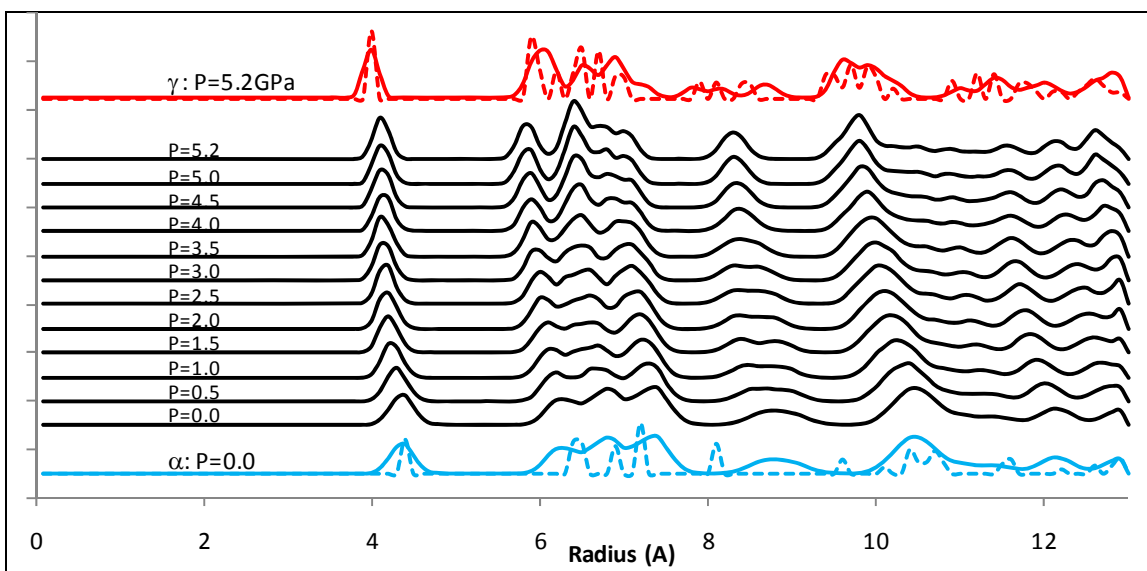
Figure 4. Scaled molecule center of mass RDF for compression simulations of α-RDX. Each RDF is at a different pressure shown by labels. Top and bottom thermalized (solid line) and experimental (dashed line) (12) RDF's in blue (α-RDX) and red (γ-RDX) shown for reference.

The experimental RDF of α-RDX is compared to its thermalized RDF at the same state, T=300 K, P=1 atm, shown by the blue dashed and solid line, respectively. The first four peaks of the experimental data are accurately captured by the thermalized data. Two distinct peaks in the 8-10 A region join into one broad peak in the simulation data. Molecules within 10 A make up the first set of nearest neighbors, and this distance is specified as the real space cut-off of nonbonded interactions in the simulation set-up. Beyond about 12 A, the RDF approaches unity. The sequence of pressurization simulations for α-RDX, shown in figure 4, start in the blue configuration of α-RDX, shown at the bottom of the plot. The solid blue line is the same RDF as the black line labeled P=0.0. The pressure is then increased, and the peaks of the RDFs move closer to the origin as the molecules are squeezed closer together. During pressurization, peaks narrow and separate as the thermal vibrations are reduced. At around P=4 GPa, the peaks begin to sharpen in the 5-8 A region, and the broad peak from 8-10 A narrows, but this is result of the reduced molecular mobility as the pressure is increased, and not a phase transition. The top solid black line labeled P=5.2 GPa is not representative of the of the solid red line of the thermalized γ-RDX phase at 5.2 GPa. There is a difference in the number of peaks in the 8-10 A region (3 for γ-RDX, 1 for α−RDX), the relative size of peaks from 6-10 A (first peak is largest for γ-RDX, first peak is smallest for α-RDX), and the location of the first peak at 4 A.

The RDF for g-RDX decompression with the same reference state for a- and g-RDX in blue and red, respectively, is shown in figure 5. In these simulations the pressure is reduced and starts in the configuration labeled P=5.2. As the pressure is reduced, a noticeable change occurs at P=2.0 GPa, which is also the pressure that kinks in the volume, and lattice constants were seen in figures 2 and 3. For P < 2 GPa, the system goes to the thermalized α-RDX configuration.
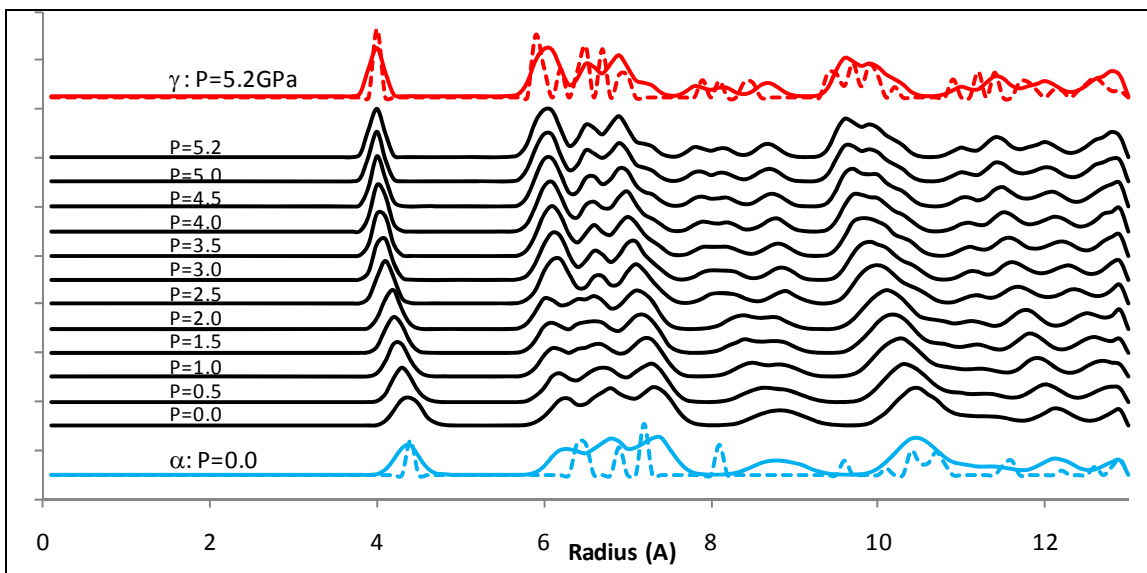
Figure 5. Scaled molecular center of mass RDF for decompression simulations of γ-RDX. Each RDF is at a different pressure shown by labels. Top and bottom thermalized (solid line) and experimental (dashed line) (*13*) RDF's in blue (α-RDX) and red (γ-RDX) shown for reference.

A phase transition determined by the locations of peaks in the RDF can be summarized by a single data point determined by the time-averaged mean square displacement (MSD) of atoms. The MSD compares the current atomic location to the initial atomic location at the start of the simulation. In this work, the MSD is averaged for each atomic species—carbon (C), nitrogen (N), oxygen (O), and hydrogen (H). The MSD of the carbon atoms contained in the ring is plotted in figure 6 and provides a good approximation to the MSD of the molecule center of mass. Since each set of compression or decompression simulations is done incrementally, a large spike in the MSD will occur when the molecules shift from the phase they are started in to a new one, as is shown for the γ-RDX simulation data at P=2 GPa. The time-averaged MSD for α-RDX does not show a spike in figure 6, and it can be concluded that a phase transition does not occur during the pressurization of α-RDX in these simulations, even though the reverse transition from γ- to α-RDX readily occurs at ~2 GPa. The difference between the α- and γ-RDX MSD at pressures below 2 GPa could be caused by a rotation in the molecule. The MSD is a measure of the fluctuations in atomic positions. Other fluctuation formulas exist for energy terms that can be used to determine thermodynamic properties, such as the heat capacity, which can also be used to provide evidence of a phase transition.
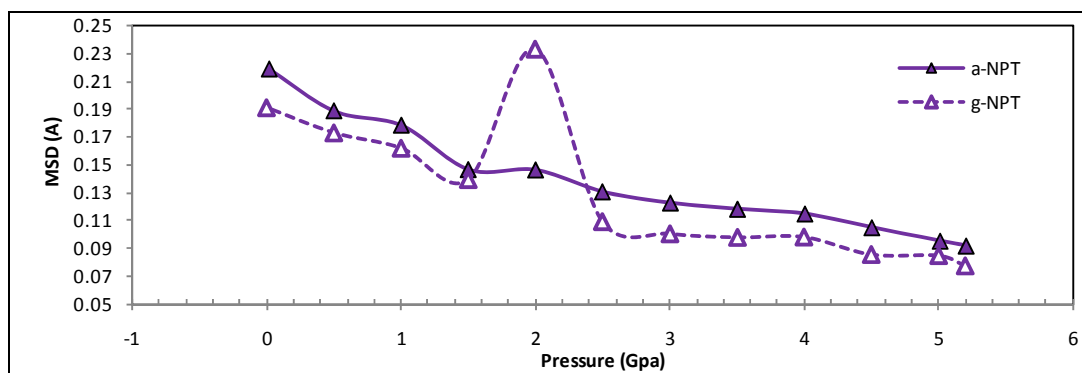
Figure 6. Time averaged MSD for a- and g-RDX versus pressure.

Up to this point, the determination of the crystal structure has been based on intermolecular properties, such as molecule-to-molecule spacing, lattice constants, and volume. None of these measures highlight the main difference between the α- and γ-RDX crystals, which is contained in the molecule conformation and the orientation of the nitro groups with respect to the central amine ring. This orientation is referred to as the wag angle and is shown below in figure 7. The orientation of the N-N bond with the C-N-C plane is the wag angle, δ, shown in figure 7. Wag angles in this work are referenced by their respective nitro groups based on the numbering shown for a right handed molecule in figure 7(b).
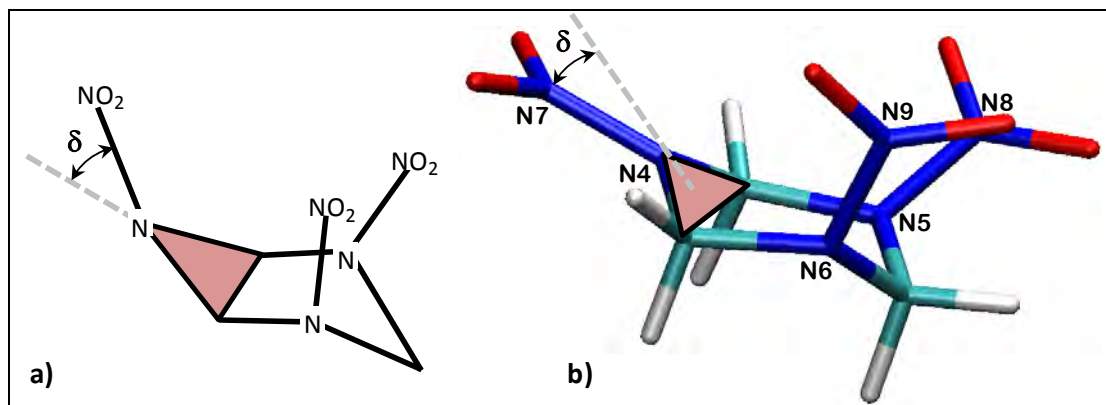
Figure 7. (a) Wag angle, δ, used to describe nitro group orientation. (b) N4-N7 wag angle shown on thermalized right handed molecule.

RDX molecules are described by δ for each N-N group—Equatorial (E) for $\delta<0°$, Axial (A) for $\delta>10°$, and Intermediate (I) for $0°<\delta<10°$. These definitions of A, E, and I are based on somewhat arbitrary values of δ that only apply to RDX. Choi and Prince (12) determined the α-RDX unit cell to belong to the Pbca space group and contain eight symmetrically equivalent molecules with nitro groups in the Axial, Axial, Equatorial (AAE) positions. Davidson et al. (13) determined the γ-RDX unit cell to belong to the Pca2$_1$ space group, with four symmetrically equivalent sites, and each site containing two separate molecules in two different configurations, AAE and AAI.

In this work, instantaneous wag angles are determined for every N-N group in the simulation cell at 30 different instantaneous atomic configurations separated by 0.75ps. Each wag angle type is then summed according to which of the eight molecule types of the unit cell it belongs to. Histogram data of each wag angle type for each of the eight molecules of the unit cell is then plotted to determine the conformation of the molecule, as is shown in figures 8(a)–(c) for α-RDX, and in figures 9(a)–(c) for γ-RDX. Only the outline of the histogram data is plotted in figure 8.
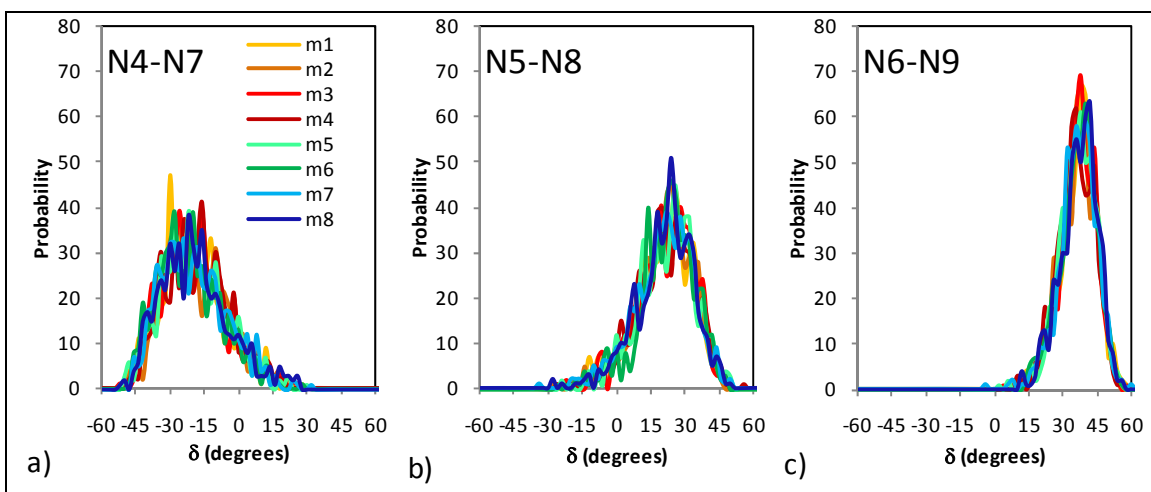
Figure 8. α-RDX AAE conformation determined from Wag angle histograms at T=300K, P=0, for (a) N4-N7, (b) N5-N8, and (c) N6-N9 for each molecule type in the unit cell.
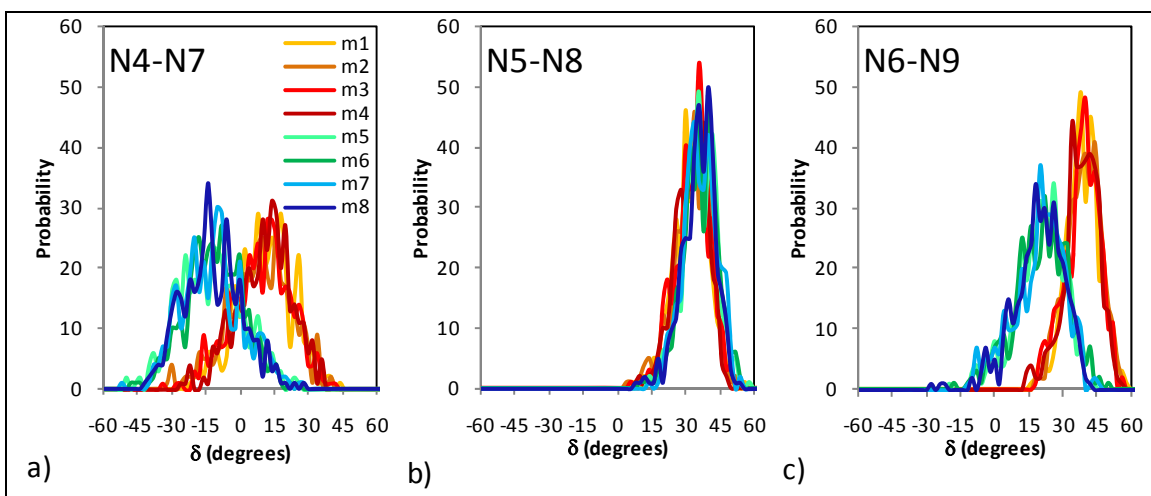
Figure 9. γ-RDX AAE & AAI conformations determined from Wag angle histograms at T=300K, P=5.2GPa, for (a) N4-N7, (b) N5-N8, and (c) N6-N9 for each molecule type in the unit cell.

The difference between the α- and γ-RDX phase is highlighted by the separation of the histogram data for the N4-N7 and N6-N9 wag angles in figure 9(a) and (c), signifying two distinct molecule conformations in the unit cell. The peak thermalized/experimental wag angles for α-RDX are 25°/34°, 45°/33°, and –20°/–20° for the N5-N8 axial (A), N6-N9 axial (A), and

24

N4-N7 equatorial (E), respectively. The peak thermalized/experimental wag angles for type 1 molecules of γ-RDX are 36°/36°, 40°/36°, and 8°/10° for the N5-N8 axial (A), N6-N9 axial (A), and N4-N7 equatorial (I), respectively. The peak thermalized/experimental wag angles for type 2 molecules of γ-RDX are 38°/40°, 20°/17°, and –14°/–2° for the N5-N8 axial (A), N6-N9 axial (A), and N4-N7 equatorial (E), respectively. The unit cell of for α-RDX is shown in figure 10(a)–(c), and using the same basis molecules, the unit cell of γ-RDX is shown in figure 10(d)– (f).
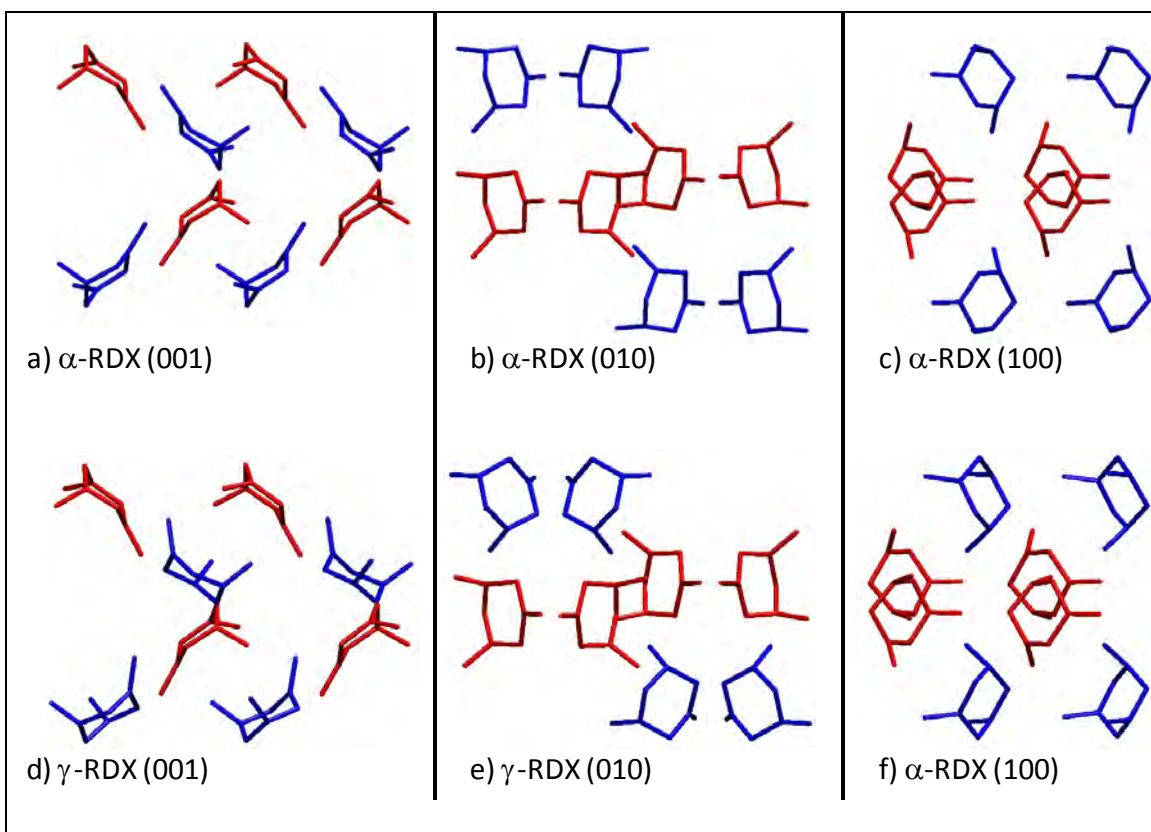
Figure 10. RDX unit cells with H and O atoms removed projected onto crystal planes (shown in parentheses). Molecules colored according to γ-RDX molecule type. Type 1 AAI molecules shown in blue and type 2 AAE molecules shown in red.

The AAE molecules shown in red undergo very little change in lattice location or conformation, as shown by comparing the α- to γ-RDX unit cells in figure 10. The change between an AAE and AAI molecule is shown by comparing the blue molecules in figures 10(a) and (d). The rotation required to allow for the AAI conformation is shown by comparing the blue molecules in figures 10(b) and (e). The AAI or type 2 molecules undergo a ~20° rotation about an axis oriented normal to the amine ring when compared to the orientation in α-RDX. This molecule rotation seems to be essential to the phase transition, and isotropically stressing the α-RDX simulation cell may not allow this rotation to occur. The pressurization simulations starting in α-RDX may not go through a phase transition due to some type of artificial constraint on molecule

rotation caused by the simulation cell or boundary conditions. The α- to γ-RDX phase transition may be possible to recreate by applying non-hydrostatic states of stress or strain, which could free up rotational degrees of freedom in the molecule.

3.2 NVT Uniaxial Strain Simulations

The orientation dependence of the RDX crystal response to uniaxial loading will be studied in this work by using NVT simulations of uniaxially strained RDX lattices in the α- and γ-RDX phases. We will determine the orthotropic elastic constants for linear elasticity for these phases and the dependence of strain on the phase transition. The strain orientation dependence of the phase transition will elucidate the mechanism to which it occurs and possibly provide an explanation of why it does not occur under isotropic NPT pressurization. The uniaxial strain simulations here will provide insight into highly constrained deformation that could be caused by high pressure shock fronts and rigid boundary conditions.

The initial configurations for the NVT simulations come from NST simulations of the α- and γ-RDX, thermalized at the experimental states at which they were measured—T=300 K, P=0 for α-RDX, and T=300 K and P=5.2 GPa for γ-RDX. The b- and c-axes for γ-RDX have been switched from those given by Davidson et al. (*13*) in order for them to correspond to the α-RDX crystal axes given by Choi and Prince (*12*). The thermalized α- and γ-RDX crystals were isostrained by each strain component in compression and tension, respectively. These strained configurations were then thermalized in the NVT ensemble. Ten strain increments of 0.1% were applied to the initial configurations up to 1.0% stain. The time-averaged stress tensor from these simulations was used to determine the relationship between stress and applied strain. Assuming the strain increments are small, and the material is orthotropic due to the symmetry of the α- and γ-RDX space groups, the material can be approximated as an orthotropic linear elastic material with the strain relationship given in Voight notation as

$$
\begin{Bmatrix} \sigma_{11} \\ \sigma_{22} \\ \sigma_{33} \\ \sigma_{23} \\ \sigma_{31} \\ \sigma_{12} \end{Bmatrix} = \begin{bmatrix} C_{11} & C_{12} & C_{13} & 0 & 0 & 0 \\ C_{21} & C_{22} & C_{23} & 0 & 0 & 0 \\ C_{31} & C_{32} & C_{33} & 0 & 0 & 0 \\ 0 & 0 & 0 & C_{44} & 0 & 0 \\ 0 & 0 & 0 & 0 & C_{55} & 0 \\ 0 & 0 & 0 & 0 & 0 & C_{66} \end{bmatrix} \begin{Bmatrix} e_{11} \\ e_{22} \\ e_{33} \\ 2e_{23} \\ 2e_{31} \\ 2e_{12} \end{Bmatrix}, \tag{4}
$$

where C_{ij} are the elastic constants, and the a-, b-, and c-directions are given by the $\mathbf{e}_1$, $\mathbf{e}_2$, and $\mathbf{e}_3$ Cartesian coordinates. Orthotropic elastic constants from these simulations are given in table 4, and compared to α-RDX experimental elastic constants and other simulation data. The γ-RDX elastic constants are measured from P=5.2 GPa and, therefore, are much more compressed and stiffer than the α-RDX elastic constants. When atoms are brought closer together due to large compressions, the atoms repel one another—caused by Pauli exclusion principle—which is captured in the SB potential function by the exponential term of the Buckingham potential. Both sets of elastic constants show similar trends, and the ordering of stiffest directions stays constant

between phase, $C_{11}>C_{22}>C_{33}$. The largest increase is in the coupling or Poisson terms affecting the extensional strains, C_{23}, C_{31}, and C_{12}. There is not experimental data to verify the γ-RDX elastic constants, but the α-RDX elastic constants compare well to other α-RDX simulations by Sewell et al. (*17*) using a different potential and the experimental data.

Table 4. Elastic tensor: b- and c-axes of γ-RDX have been switched from
that given by Davidson et al. (*13*) in order to correspond to α-RDX
coordinates given by Choi and Prince (*12*).

Orthotropic elastic constants (GPa)

	(γ)NVT	(α)NVT	(α)Sewell[a]	(α)Haycraft[b]	(α)Schwarz[c]
C_{11}	80.28	25.04	26.87	36.67	25.60
C_{22}	67.02	23.80	24.08	25.67	21.30
C_{33}	57.85	23.35	17.69	21.64	19.00
C_{44}	11.95	3.12	8.40	11.99	5.38
C_{55}	16.30	7.69	5.30	2.72	4.27
C_{66}	13.43	5.18	7.60	7.68	7.27
C_{23}	45.56	6.26	6.32	9.17	6.40
C_{31}	36.95	7.59	5.68	1.67	5.72
C_{12}	37.83	11.24	6.27	1.38	8.67

[a]Sewell et al. (*17*), [b]Haycraft et al. (*18*), [c]Schwarz et al. (*19*)

The orthotropic elastic constants are accurately predicted using uniaxially strained lattices and the NVT ensemble for the α-RDX thermalized crystal. This method should be extendable to larger strains where the stress/strain relationship becomes nonlinear. The diagonal strain components between α-RDX at P=0 and γ-RDX at P=5.2 GPa are 6%, 4%, and 10% for E_{11}, E_{22}, and E_{33}, respectively. The strain components for α-RDX at P=2GPa, the simulated α- to γ-RDX phase transition pressure, are –3%, –3%, and –4% for E_{11}, E_{22}, and E_{33}, respectively. From the strain found for the NST simulations, it is determined that the system should be strained up to 10% in compression for α-RDX and 10% extension for g-RDX.

The simulation procedure uses the final atomic coordinates of the previous strained simulation and deforms them by 1.0%. Deformation is determined using the deformation gradient, F_{ij}, given by

$$\underline{\underline{F}} = [h][h_o]^{-1},\tag{5}$$

where [h] and [h$_o$] are tensors containing column wise lattice vectors. The configuration to be strained is given by [h$_o$] and the final configuration for the new simulation is [h]. The Lagrange strain, E_{ij}, for this is given by

$$\underline{\underline{E}} = \tfrac{1}{2}\left(\underline{\underline{F}}^T\underline{\underline{F}} - \underline{\underline{I}}\right) = \tfrac{1}{2}\left([h_o]^{-T}[h]^T[h][h_o]^{-1} - \underline{\underline{I}}\right),\tag{6}$$

where I is the identity tensor. The system is incrementally strained so $[h_o]$ changes to the subsequent strained configuration that $[h]$ is calculated from. F_{ij} is taken to be

$$\underline{\underline{F}} = \begin{bmatrix} 1+\alpha & 0 & 0 \\ 0 & 1+\beta & 0 \\ 0 & 0 & 1+\gamma \end{bmatrix}, \qquad (7)$$

where α, β, and γ are applied individually and are set to a constant value of 0.1. The new configuration, $[h]$, is given by

$$[h] = \underline{\underline{F}}[h_o] \qquad (8)$$

The molecule centers of mass are displaced according to F_{ij}, and all atoms of the molecule are moved as a rigid body so as not to strain the intramolecular bonds. Each simulation is equilibrated for 7.5 ps and thermalized for 75 ps. Time-averaged values from the thermalization portion are used in this analysis, and all values are offset so that the values for α-RDX at P=0.0 are zero. All energies are given per mole of RDX molecules. Only the results for the α-RDX uniaxial strain simulations will be presented. Some difficulties were found in determining a common reference state between the α- and γ-RDX uniaxial strained states.

Final strained α-RDX unit cells for E_{ii}=-9.1% are shown in figure 11. The projection axis of each figure is labeled at the tops of the columns, and the strain direction is labeled to the left of each row. The top row is the unstrained, thermalized α-RDX configuration. The second row is for E_{11}=-9.1%, and very little change is observed. The third row is for E_{22}=-9.1%, and the location of the two central molecules shift in the b-direction shown for the (001) projection. The fourth row is for E_{33}=-9.1%; the (010) project shows the AAI and AAE molecule conformations, and the (001) project shows the rotation of the AAI molecules as is seen in γ-RDX.

For all of the cases of uniaxial strain, phase transitions are observed in the E_{22} and E_{33} direction, and only the E_{33} strain produces the phase transition to γ-RDX. Straining in the E_{33} or along the c-direction while holding the a- and b-lattices fixed must provide the required molecule mobility needed for the α- to γ-RDX phase transition. Uniaxial straining along the different crystal axes activates different terms of the SB potential. The overall value of the SB potential energy is plotted in figure 12 for each strain direction. The large grouping of data points near the origin is for the linear elastic strain calculations used to find the elastic constants presented in table 4. The other large grouping of points for the E_{22} and E_{33} curves are in the region of the phase transition. The curvature of the potential energy versus strain changes at the phase transition. The magnitude of the potential energy for the E_{22} and E_{33} strain directions are of similar value, which is not surprising because they have similar stiffness values for C_{22} and C_{33} in table 4. The potential energy for the E_{11} direction is the highest and it is also the stiffest direction. The RDF and wag angles used to determine the γ- to α-RDX transition for the NST decompression simulations verify that the phase from E_{33} strain is the γ-RDX phase.
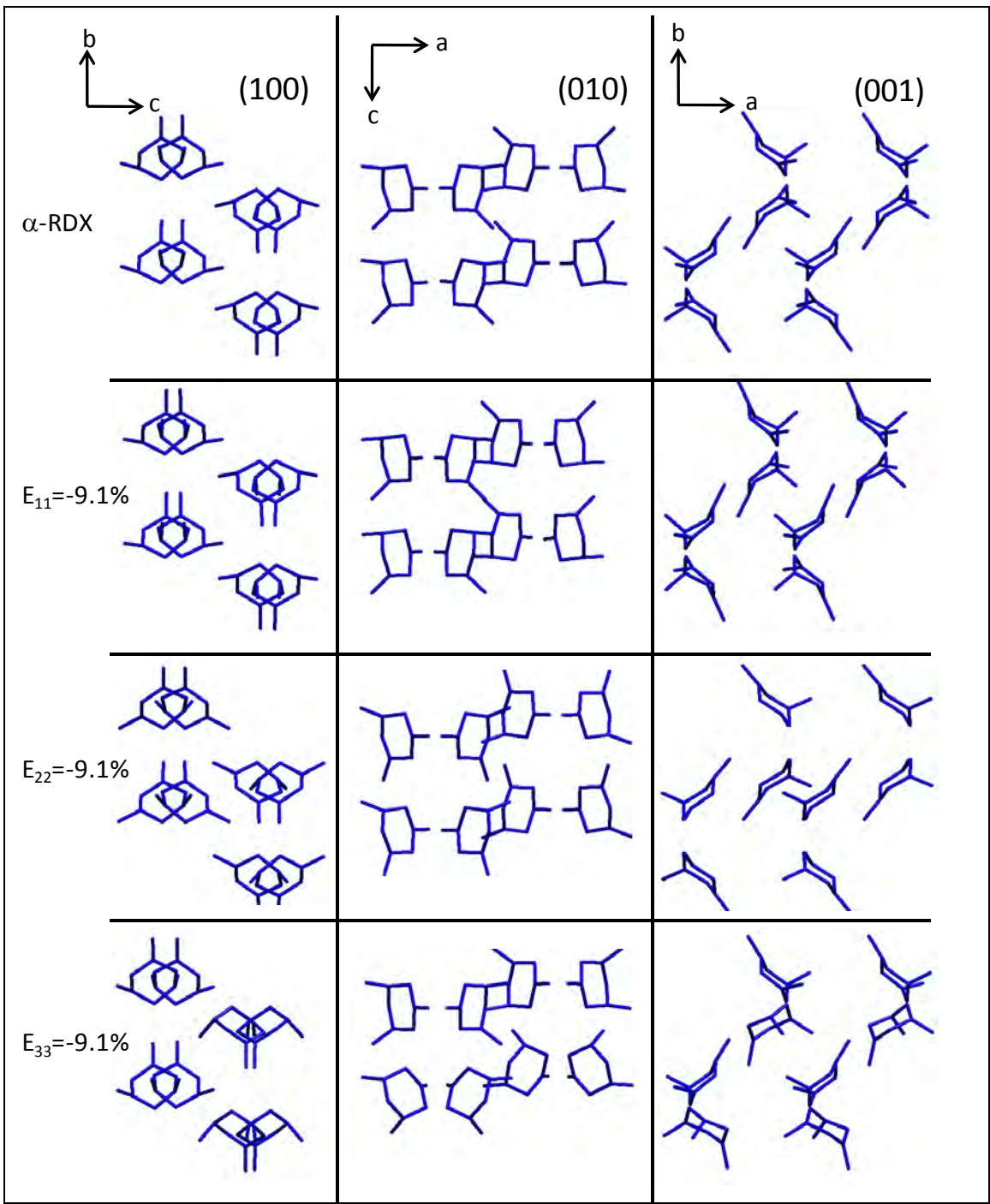
Figure 11. Final strained a-RDX unit cells. Projection planes common for each column and listed at the top. Strain direction common for each row and listed to on the left.
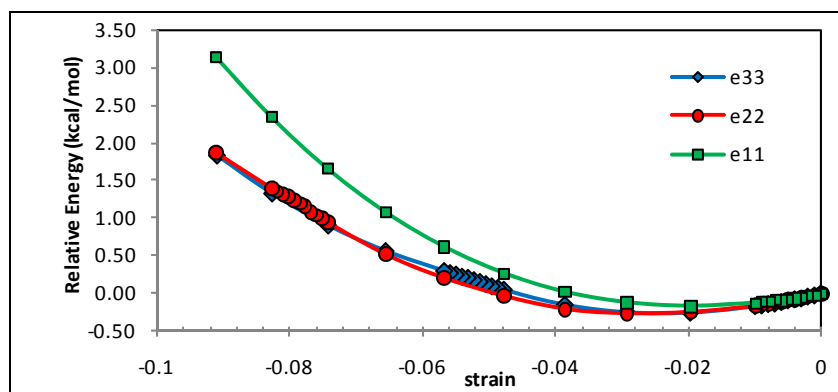
Figure 12. Relative potential energy per mol of molecules for α-RDX for the three cases of uniaxial strain.

Each component of the SB potential energy function is explored individually to determine which energy components are activated by each of the uniaxial strains in figures 13 and 14. The phase transition from these plots is apparent by the sharp discontinuity in the curves. The phase transition induced by E_{22} leads to a large increase in electrostatic energy, shown in figure 13(a). The large change in nonbonded energy for the phase transition occurring for E_{22} approximately balance each other out, and the potential energy in figure 12 does not show a large break in energy. It is interesting to note that in figure 14, the change in angle and dihedral energy for E_{22} is initially opposite to that of both E_{11} and E_{33}. The bond energy was not plotted because it is a stiff harmonic potential energy function and does not change noticeably across the phase transition.
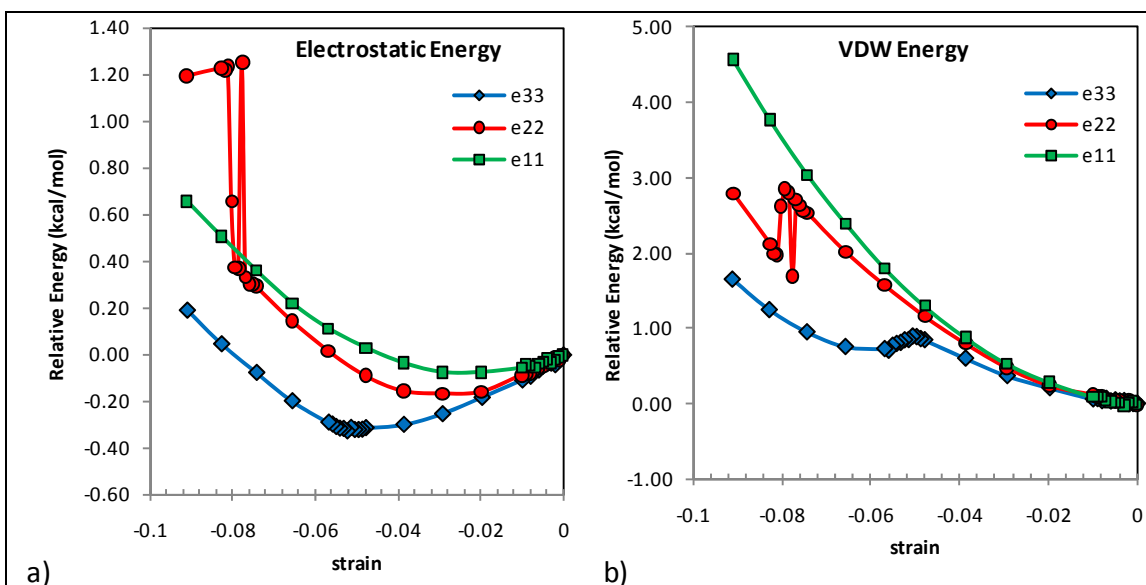
Figure 13. (a) Electrostatic and (b) van der Waals energy per mol of RDX molecules for α-RDX.

30
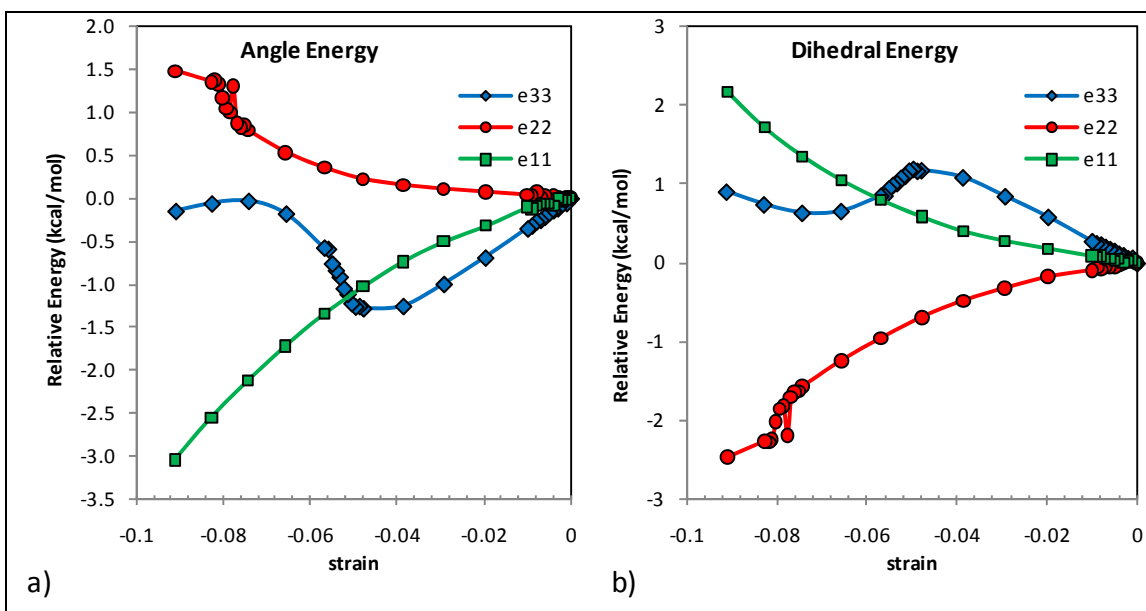
Figure 14. (a) Angle and (b) dihedral energy per mol of RDX molecules for α-RDX.

3.3 Stacking Mismatch Simulations

One of the main goals of this research is to develop a continuum model of the deformation features in RDX and other energetic crystals to determine the conditions favorable to dislocation emission and brittle fracture. Dislocation emission leads to plastic behavior, and brittle fracture leads to the creation of new surface area. Both of these mechanisms affect the subsequent response of the material to continued loading. Dislocation emission provides a means for dislocations to build up at obstacles, as proposed by Armstrong (*3*). The obstacles may be the result of limited available slip systems proposed by Ramos et al. (*5*). The dislocations could also get tangled up in the complex structure of the molecules, as in the steric hindrance model of Dick and Ritchie (*4*). All of these theories agree on the ability of the material to emit dislocations, so it is important to understand theoretically under what conditions RDX will emit a dislocation and under what conditions it will fracture.

Brittle versus ductile fracture is studied using energy release rates of cleavage, G_{cleav}, and dislocation emission, G_{disl}. The energy release rate for brittle fracture is understood in terms of the Griffith criterion, if $G_{cleav} > 2\gamma_s$, fracture occurs where γ_s is the energy of a free surface, and the factor of 2 comes from the creation of two surfaces (*20*). Ductile behavior is more complex, requiring a dislocation to nucleate at a crack tip and then be driven away from the crack tip. A material behaves in a ductile manner if $G_{disl} < G_{cleav}$.

Rice (*2*) developed a method of determining G_{disl} by using the Pierls concept of creating a shear stress-atomic displacement interplanar potential that could be applied as a boundary condition to the elasticity solution for a traction free crack loaded in mode II. Rice determined G_{disl} to be equal to a new solid state parameter called the unstable stacking fault energy γ_{us}. Within this

model, the stress intensity factor, K_{II}, is found to be proportional to $\sqrt{\gamma_{us}}$. This parameter cannot be directly determined experimentally but is readily available at the saddle points of the energy contours shown in figures 17 and 19. Rice also developed the theory to deal with partial and mixed mode dislocations, both of which will be important for the RDX crystal. Rice's model is shown to provide accurate estimates for fcc crystals and metals loaded in pure mode II. An approximate expression is provided for mixed mode loading.

Analysis using Rice's model will incorporate atomistic effects into the continuum description of the material's deformation. This will provide the ability to predict the deformation mechanism in RDX based on a variety of loading conditions. Rice's model can also incorporate temperature dependence to predict the temperature at which the deformation mechanism under an applied mode of loading switches from brittle to ductile.

The SB potential will be used to determine the generalized stacking-mismatch energy contours, or γ-surface, for the crystallographic planes of α-RDX. The γ-surface refers to an energy contour and is not related to the γ-RDX phase. The planes to be studied are the experimentally determined slip planes (*5*). The γ-surface will be used to determine parameters for continuum level models of fracture and dislocation emission, such as Rice's dislocation nucleation model (*2*). This section will provide details of the stacking fault simulations that have been done for the (010) and (001) planes.

Figure 15(a) shows the initial crystal lattice used to create stacking faults on the (010) slip plane. The lattice shown contains 3x30x3 unit cells of α-RDX. This lattice will be used to create a stacking fault on the (010) plane by displacing the top half of the lattice by a vector **u=u_a+u_c** relative to the bottom half along the (010) slice plane shown in figure 15(b). The purpose of the simulations is to create a single infinite stacking mismatch across the slip plane surrounded by the bulk material. The infinite slip plane is created using periodic orthorhombic boundary conditions in the a- and c-directions. Creating a single stacking mismatch across the slip plane surrounded by bulk material in the b-direction is more difficult and requires the creation of a sandwiched structure of active molecules surrounded by frozen molecules to simulate the bulk. A vacuum is created at the top of the structure so as to not create a second stacking fault due to periodic boundary condition in the b-direction. The frozen atoms shield the effect of the free surface from the active molecules at the slip plane and also constrain the motion of active molecules. A similar sandwich structure and simulation procedure was used by Bedrov et al. to study the development of γ-RDX in the vicinity of shock loads (*10*).

The stacking mismatches for the (010) plane are created by the following procedure:

- Anneal 3x3x3 lattice using NPT ensemble at P=0 and T=25K. NPT ensemble with orthorhombic boundary conditions is used to constrain lattice vectors to remain orthogonal during simulation. Annealing process involves a series of 25K thermalizations followed by

conjugate gradient force minimizations. The minimum energy configuration from the annealing process is used in the remainder of steps.

- Anneal minimized configuration from step 1 using an NVT ensemble and keep minimum energy configuration.

- Use the averaged 3x3x3 system to construct a 3x30x3 crystal lattice by repeating it 10 times in the b-direction.

- In the new 3x30x3 superlattice, freeze the atomic positions of the top 14 and bottom 14 unit cells in the b-direction

- Add a 4 nm vacuum region to the top of the simulation cell by increasing the b-lattice by 4 nm.

- Apply strain in the b-direction to the layer of flexible molecules on top of and below the stacking fault to displace them away from each other along the stacking fault. This is done to keep the atomic coordinates of the molecules from coinciding at the start of the simulation from the displacements applied in the next step.

- Displace the top half of molecules by a fraction of the |a| and |c| lattice lengths so as to create a grid of 100 displaced configurations on the (010) plane.

- Run NVT annealing simulations at T=25 K for each new stacking mismatch configuration.

- For each simulation, the minimum potential energy provides a single scalar energy value on the 10x10 γ-surface plotted in figure 17.

- The minimized atomic coordinates of the flexible layers are used to find the structure and molecule conformation of the stacking mismatches.

Note: The same procedure is used to create the (001) stacking mismatches, except that unit cells are stacked in the (001) direction.
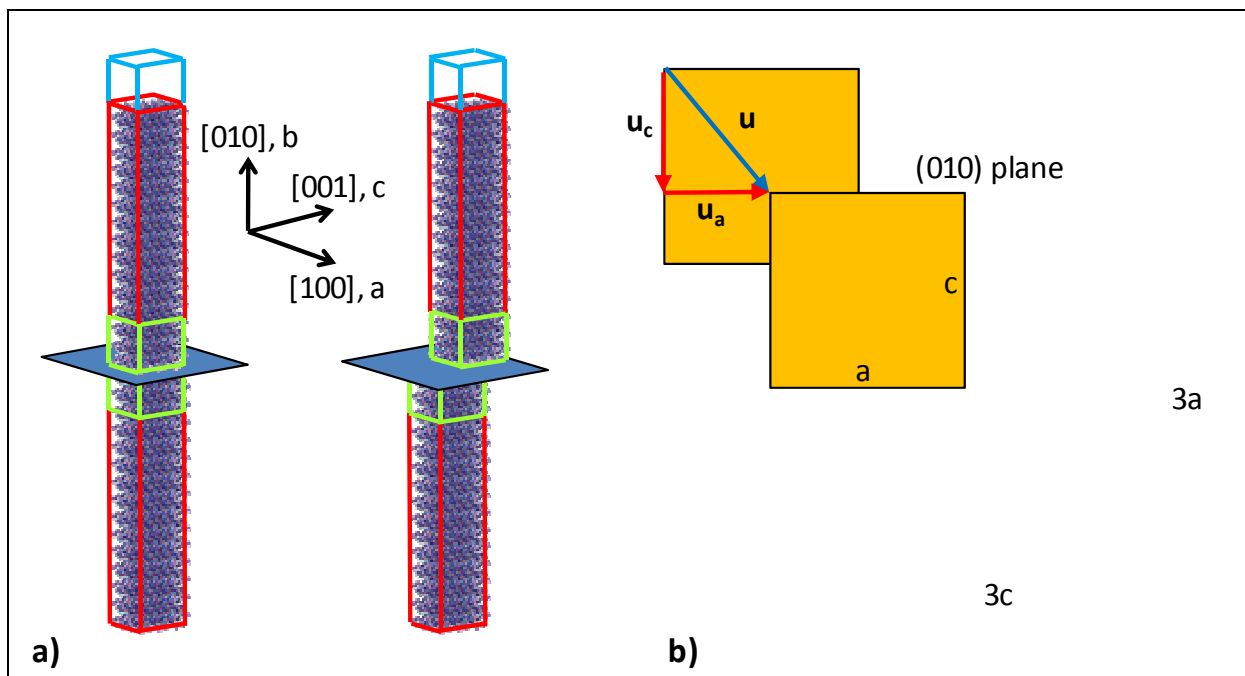
Figure 15. (a) 3x30x3 α-RDX sandwich structure where the blue region is 4-nm vacuum, red are frozen atoms, and green are fully flexible molecules with slice plane through center of green. (b) Schematic of displacement, u = u_a + u_c, of upper lattice on glide plane.

The cut plane for the (010) stacking fault is shown in figure 16. For displacement in the a-direction, no molecules come into contact with each other. Displacement in the c-direction requires the molecules across the slip plane to move in the b-direction in order to move out of each other's way. This strains the lattice locally, and potential energies for these stacking faults are large. This steric effect of large molecules blocking available slip systems is common to energetic crystals and molecular crystals in general.
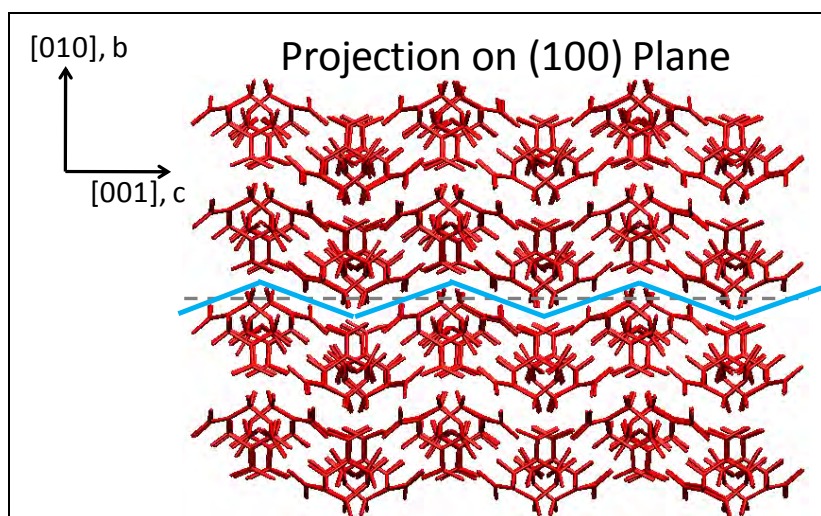
Figure 16. Side view of the stacking fault cut plane in blue for the (010) slip plane. Molecules above the blue line are moved in the c- and a-directions.

The γ-surface is shown in figure 17(a) for the (010) slip plane shown in figure 16. Large energy barriers are shown by the red contours for displacement in the c-direction, also shown by the red line in the energy plot in figure 17(b). A much smaller energy barrier is encountered for displacements in the a-direction, shown by the green line in figure 17(b). The dashed line in figure 17(b) is the free surface energy for the (010) plane multiplied by two.
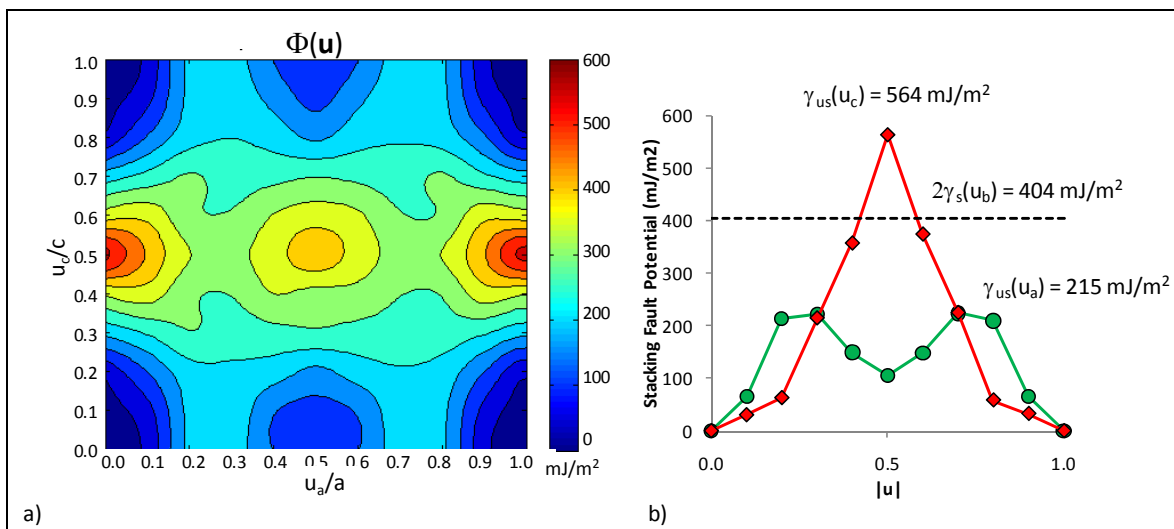
Figure 17. (Left) γ-surface for (010) stacking fault, and (right) slices of γ-surface along a- (green) and c-axis (red). Saddle point and free surface energies labeled

The cut plane for the (001) stacking fault is shown in figure 18. Again, for displacement in the a-direction, no molecules come into contact with each other. Displacement in the b-direction requires the molecules across the slip plane to move in the c-direction in order to move out of each other's way. This strains the lattice locally, and potential energies for these stacking faults are large.
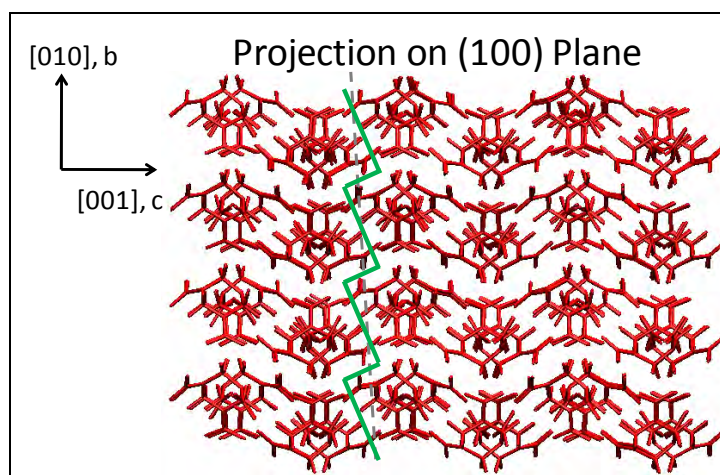
Figure 18. Side view of the stacking fault cut plane in green for the (001) stacking fault. Molecules above the right of the line are moved in the b- and a-directions.

The γ-surface is shown in figure 19(a) for the (010) slip plane shown in figure 18. Smaller energy barriers occur for the sterically hindered displacement in the b-direction on this slip plane than for the (001)[001] slip system shown by the red line in figure 17(a). A much smaller energy barrier is encountered for displacements in the a-direction, shown by the green line in figure 19(b). The dashed line in figure 19(b) is the free surface energy for the (001) plane multiplied by two. Results for the (001) and (010) slip planes are summarized in table 5.
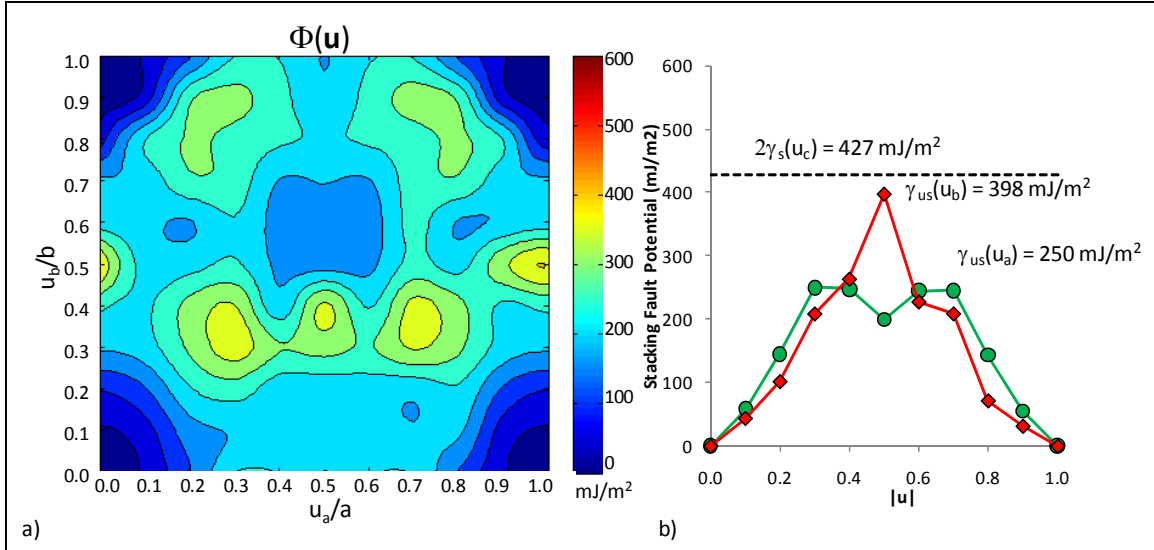
Figure 19. (Left) γ-surface for (001) stacking fault, and (right) slices of γ-surface along a- (green) and b-axis (red). Saddle point and free surface energies labeled

Table 5. Summary of slip systems and prediction of deformation mechanism based on Rice's analysis (2)

Summary of Slip Systems

Slip Systems	γ_{us} (mJ/m2)	$2\gamma_s$ (mJ/m2)	ratio	This Work	Experimental[a]
(010)[001]	564	404	1.40	Brittle	Cross-slip
(010)[100]	215	404	0.53	Ductile	Slip System
(001)[010]	398	427	0.93	Ductile	Cleavage Plane
(001)[100]	250	427	0.59	Ductile	Cleavage Plane

[a]Ramos et al. (5)

Table 5 also presents predictions based on Rice's analysis to determine the probable mode of deformation in pure mode II loading by comparing γ_{us} to $2\gamma_s$. Based on the γ-surfaces found in this work, only the (010)[001] slip system is found to be brittle. Ramos et al. (5) find this to be a cross-slip plane, meaning that it is experimentally ductile. The ductility Ramos et al. observe for this plane from nano-indentation could be due to cross slip after initial displacement to the stable stacking fault configuration at (010)[002] occurs. The (010)[001] system may also not evolve directly in the [001] direction and may vary slightly as to avoid the large energy barrier at [002], shown by the red contour in figure 17(a).

36

Ramos et al. also reported the (001) plane to be a cleavage plane, but in this work it is shown to be ductile. Ramos et al. cite other micro-indentation hardness studies as their source for cleavage on this plane. Microindentations studies on RDX crystals probably apply mixed mode loading, which would aid in the development of fracture. The ratio of γ_{us} to $2\gamma_s$ on this plane is also slightly larger than that found for the (010) plane, and it should be slightly more susceptible to brittle fracture.

Other experimental slip systems such as (021)[100] and (011)[100] reported by Ramos et al. need to be constructed and studied. One difficulty in these simulations is correctly determining the slip plane. The most probable slip plane for the (021)[100] slip system is shown in figure 20(a) by the box contained between the blue and green dashed lines. The dashed lines in figure 20 represent the slip planes. However, determining where these slip planes intersect unit cells, and which molecules lie on which side of the slip system, is difficult. This is the case for the (011)[100] slip system, and one possible unit cell is shown between the dashed lines in figure 20(b). All of the unit slip vectors activated experimentally by Ramos et al. are in the [100] direction, which is not surprising because this is the only Burgers vector for which slip can occur without the molecules running into one another—i.e., this is the least sterically hindered Burgers vector. Geometrically, dislocations favor the smallest lattice dimension because the dislocation energy scales by $|b|^2$, where $|b|$ is the length of the Burgers vector.

(021)[100] Slip System   (011)[100] Slip System

a)   b)
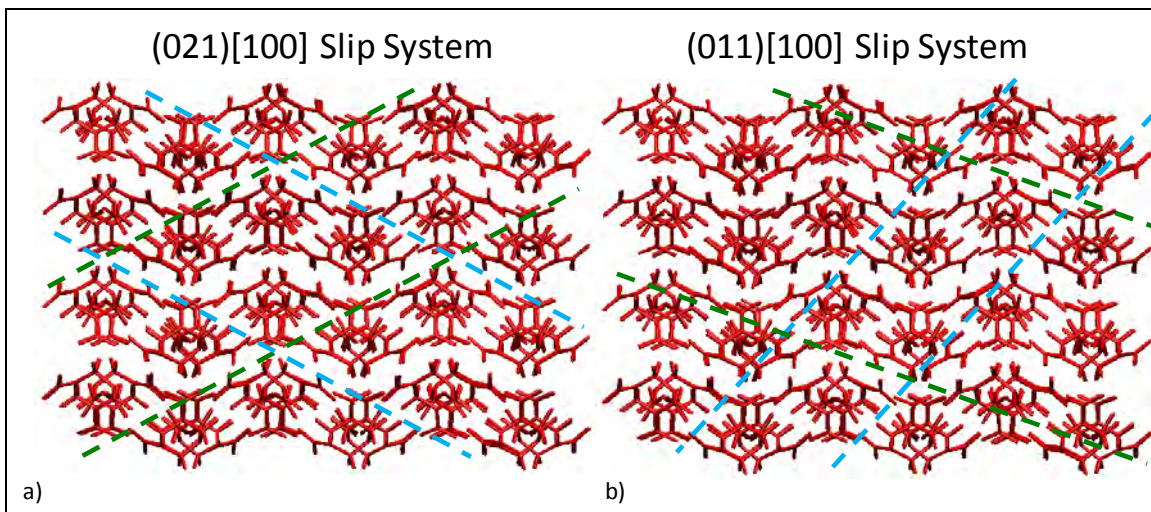
Figure 20. Other experimental α-RDX slip systems and with dashed representing slip planes.

4. Summary and Conclusions

The high pressures that occur in detonation fronts interacting with energetic crystals are in the pressure range where phase transitions may occur. The properties of these new solid phases are unlike those found at ambient conditions and may play a vital role in the development of hot

spots. This work used pressurization simulations to show the ability of the SB potential to predict both the high and low pressure (α and γ) phases of RDX and transition from the high pressure phase to the low pressures phase (γ- to α-RDX). The reverse phase transition was not observed using NPT simulations, and so NVT simulations of uniaxial strain were conducted for the low pressure α-RDX phase to determine if the phase transition was dependent on the load orientation. Applying uniaxial strain along the c-axis caused the material to convert from the α- to γ-RDX. This crystal dependence to load orientation is of interest because experimental data by Cawkwell et al. (*9*) show the orientation dependence of shock properties, and their simulation work determined that the dislocation structures involved the phase transition from α- to γ-RDX.

The deformation mechanisms of RDX are of interest to the energetic materials community because of their role as a localization feature in perfect crystals under low strain rate loading, which occurs during accidental mishandling. This work provides an initial estimate and method of predicting if dislocation nucleation or brittle fracture will occur based on the continuum level stress intensity factors using Rice's model. These atomistic level details of the deformation mechanism that are active for low strain rate loads are lacking in both simulation and experimental literature. Cawkwell et al. (*9*) report that according to the steric hindrance model, deformation along orientations containing active or inactive slip systems are either insensitive or sensitive, respectively. By determining the γ-surface for the different experimental and crystallographic planes, as was done in this work, Rice's analysis can be used to determine the active and inactive slip systems, and from that, determine orientations to which the material is most sensitive to shock.

The future work will provide a methodology for studying crack tip dislocation emission and brittle fracture of RDX, which is also applicable to other molecular crystalline materials held together by nonbonded forces. The future work will be useful to the modeling community by providing information on the deformation features that need to be captured in the continuum level hydrocodes. These hydrocodes are important to the development and testing of new military munitions to determine their effectiveness and safety. By better understanding the deformation and fracture process, the manufacturing process of munitions can be made safer and provide more effective munitions. Explosive fills are sometimes compressed or machined for munitions, and defects introduced during this stage may affect both their performance and safety. This is also true in the pharmaceutical industry, where several drugs of interest use molecular crystals as active ingredients. The molecular crystals are pressed into pill form, and fractures introduced during this step will affect the rate at which the body is able to break them down and absorb them.

5. References

1. Smith, G. D.; Bharadwaj, R. K. Quantum Chemistry Based Force Field for Simulations of HMX. *Journal of Physical Chemistry B* **1999**, *103*, 3570–3575.

2. Rice, J. R. Dislocation Nucleation from a Cracktip: An Analysis Based on the Peierls Concept. 2. *Journal of the Mechanics and Physics of Solids* **1992**, *40*, 239–271.

3. Armstrong, R. W. Dislocation Mechanics Aspects of Energetic Material Composites. *Reviews on Advanced Materials Science* **2009**, *19*, 13–40.

4. Dick, J. J.; Ritchie, J. P. Molecular Mechanics Modeling of Shear and the Crystal Orientation Dependence of the Elastic Precursor Shock Strength in Pentaerythritol Tetranitrate. *Journal of Applied Physics* **1994**, *76*, 2726–2737.

5. Ramos, K. J.; Hooks, D. E.; Bahr, D. F. Direct Observation of Plasticity and Quantitative Hardness Measurements in Single Crystal Cyclotrimethylene Trinitramine by Nanoindentation. *Philosophical Magazine* **2009**, *89*, 2381–2402.

6. Smith, G. D.; et al. Quantum-Chemistry-Based Force Field for Simulations of Dimethylnitramine. *Journal of Physical Chemistry B* **1999**, *103*, 705–713.

7. Bedrov, D.; Smith, G. D.; Sewell, T. D. Thermal Conductivity of Liquid Octahydro-1,3,5,7-tetranitro-1,3,5,7-tetrazocine (HMX) from Molecular Dynamics Simulations. *Chemical Physics Letters* **2000**, *324*, 64–68.

8. Bedrov, D.; et al. Molecular Dynamics Simulations of HMX Crystal Polymorphs using a Flexible Molecule Force Field. *Journal of Computer-Aided Materials Design* **2001**, *8*, 77–85.

9. Cawkwell, M. J.; et al. Homogeneous Dislocation Nucleation in Cyclotrmethylene Trinitramine Under Shock Loading. *Journal of Applied Physics* **2010**, *107*, 1–11.

10. Bedrov, D.; et al. Shock-induced Transformations in Crystalline RDX: A Uniaxial Constant-stress Hugoniotstat Molecular Dynamics Simulation Study. The Journal of Chemical Physics **2009**, *131*, 1–12.

11. Smith, W.; Forester, T. R.; Todorov, I. T. *The DLPOLY_2 User Manual Version 2.20*. Cheshire, UK: STFC Daresbury Laboratory, 2009.

12. Choi, C. S.; Prince, E. *The Crystal Structure of Cyclotrimethylene-trinitramine*. Acta Crystallographica **1972**, *B28*, 2857–2862.

13. Davidson, A. J.; et al. Explosives Under Pressure - The Crystal Structure of g-RDX as Determined by High-pressure X-ray and Neutron Diffraction. *Crystal Engineering Communication* **2008**, *10*, 162-165.

14. Birch, F. Finite Elastic Strain of Cubic Crystals. *Physical Review* **1947**, *71*, 809–824.

15. Olinger, B.; Roof, B.; Cady, H. *The Linear and Volume Compression of b-HMX and RDX to 9 GPa (90KiloBar).* Paris, France: Commissariat a l'Energie Atomique Centre d'Etudes de Vajours, Sevran, France, 1978. Symposium International Sur Le comportement Des Milieux Denses Sous Hautes Pressions Dynamiques. pp. 1–7.

16. Podeszwa, R., Rice, B. M. and Szalewicz, K. *Crystal Structure Prediction for Cyclotrimethylene Trinitramine (RDX) from First Principles. Physical Chemistry Chemical Physics* **2009**, *11*, 5512–5518.

17. Sewell, T. D.; Bennett, C. M. *Monte Carlo Calculations of the Elastic Moduli and Pressure-volume-temperature Equation of State for Hexahydro-1,3,5-trinitro-1,3,5-triazine.* Journal of Applied Physics **2000**, *88*, 88–95.

18. Haycraft, J. J.; Stevens, L. L.; Eckhardt, C. J. The Elastic Constants and Related Properties of the Energetic Material Cyclotrimethylene Trinitramine (RDX) Determined by Brillouin Scattering. *The Journal of Chemical Physics* **2006**, *124*, 1–11.

19. Schwarz, R. B.; et al.. Resonant Ultrasound Spectroscopy Measurement of the Elastic Constants of Cyclotrimethylene Trinitramine. *Journal of Applied Physics* **2005**, *98*, 1–3.

20. Haslach, H. W.; Armstrong, R. W. *Deformable Bodies and Their Material Behavior;* s.l. : John Wiley and Sons, 2004. pp. 383–427.

U.S. Army Research Laboratory
SUMMER RESEARCH TECHNICAL REPORT

Semi-Automated Methods for Refining a Domain-Specific Terminology Base

GABRIELLA ROSE
MELISSA HOLLAND
STEVE LAROCCA
ROBERT WINKLER
MULILINGUAL COMPUTING BRANCH, CISD, ADELPHI

Contents

List of Figures

List of Tables

Abstract

A domain-specific term base may be useful not only as a resource for written and oral translation, but also for Natural Language Processing (NLP) applications, text retrieval, document indexing, and other knowledge management tasks. The objective of this investigation was to explore the use of alternative terminology extraction methods to refine and validate an existing military-specific bilingual dictionary. A series of semi-automatic methods was implemented to distill the existing term list by removing redundancies, resolving spelling variations, and separating individual expressions. Once the internal clean-up was completed, we compared two methods drawn from the terminology extraction literature in order to validate terms as military-specific and to propose a candidate list of non-specific terms for exclusion—term frequency calculations and terminology extraction lists. In this investigation, we wanted to find the best procedure to extract domain-specific terms for a low-resource domain; to demonstrate that terminology extraction methods can be used to validate and refine a domain-specific dictionary; and to provide the final, refined dictionary as a term base to support customization of machine translation systems for the military domain.

1. Introduction

Especially since the 2001 entrance of the United States into the war in Afghanistan, foreign language translation has become increasingly necessary yet still is not sufficiently resourced. Although human translators often provide high-quality work, that work can be costly and time consuming given that it is difficult to find qualified bilingual language experts across all needed domains. This lack of quick translation along with advances in the information technology field has prompted research into and use of semi-automatic machine translation (MT) methods to support human translators. Whereas word-to-word translation in specialized domains may be straightforward (e.g., stethoscope-*estetocopio*) given a language expert or a bilingual dictionary, the difficulty lies with multi-word expressions—with recognizing phrases that are in fact technical terms ("field of fire") and need to be treated as entities, and with finding their counterparts in the other language, where the phrase may or may not have the equivalent number of words.

Over the last 10 years, tools to enable automatic extraction of term bases have been developed, which speed the process of deriving term bases from a collection of documents in a domain of interest. A domain-specific term base may be useful not only as a resource for written and oral translation, but also for Natural Language Processing (NLP) applications, text retrieval (*1*), document indexing, and other knowledge management tasks. The National Virtual Translation Center (NVTC), an organization under the Federal Bureau of Investigation, was established in February 2003 for the exact purpose of "providing timely and accurate translations of foreign intelligence for all elements of the intelligence community (*2*)." In September of that year, an electronic compilation of 8953 terms with their translations was published by M. Green for the NVTC, under the title *Iraqi Military English-Arabic Arabic-English Dictionary*. While the sources of these translated terms and the purpose of the dictionary are unclear, it has been used successfully to support improved MT.

2. Examining the NVTC Bilingual Military Dictionary

Searching through the original term list, we found many internal discrepancies and inconsistencies that suggested that the term base may have been developed by several authors and provided rapidly to the field for urgent needs without opportunity for quality assurance. These internal issues would pose problems with its use in computational linguistics. The problems include the following:

1. Alignment and spacing errors

   a. White space preceding the expression alters its place when ordered alphabetically.

   b. White space trailing the expression can introduce two entries from the same expression:

      i. Example: One entry would be given as "Flank" while the other would be provided as "Flank" and they would have the same Arabic translation.

2. Thirty-three duplicate entries

   a. These entries are exactly the same in both Arabic and English; therefore, the duplicates can be removed.

3. Three variations of the same word

   a. The dictionary would include two non-identical English entries with the identical Arabic translation:

      i. Example: "Light antiaircraft" and "Light anti-aircraft" had the same Arabic translation "مقاومة طائرات خفيفة" and "مقاومة طائرات خفيفة".

   b. For the purposes of this project, both entries were used, but at the end of the investigation, only the most commonly used, grammatically correct entry was included in the dictionary.

4. Five misspellings

   a. Example: "Airconditioned shelter" should be "Air-conditioned shelter".

   b. When air-conditioned is listed as its own entry, it has the appropriate spelling, but when combined with another word, it is spelled incorrectly.

5. An unnecessary symbol, ۽, was included after three English entries.

6. For computational linguistic purposes, tokenizations would have to be performed on the following collections: parentheses (622), ampersands (15), and slashes (166). A blank space was inserted where the original character was located.

Arabic experts looked at a random sample of the existing terminology that I proposed as representative and noted that (1) the terminologies were of many cultural dialects, but mainly Standard Modern Arabic, and (2) the Arabic translation of general English words did not have a military-specific connotation, suggesting that the term does not belong in the dictionary. Since we are simply focusing on the English portion of the term base, its bilingual nature does not really enter into the processes used to refine the dictionary at this time. Further research is needed for the Iraqi-Arabic portion.

3. Internal Clean-Up

In order to make the existing term base ready for computer intervention, several changes had to be made (noted in figure 1). Using a Perl script, we found that the original NVTC term base had 8953 entries with the following breakdown:

WPL: 1	AOL: 1832	WPL: 9	AOL: 3
WPL: 2	AOL: 4795	WPL: 10	AOL: 3
WPL: 3	AOL: 1591	WPL: 11	AOL: 3
WPL: 4	AOL: 440	WPL: 13	AOL: 2
WPL: 5	AOL: 182	WPL: 14	AOL: 1
WPL: 6	AOL: 83	WPL: 16	AOL: 2
WPL: 7	AOL: 24	WPL: 18	AOL: 1
WPL: 8	AOL: 15	WPL: 19	AOL: 1

WPL: Words per Line

AOL: Amount of Lines
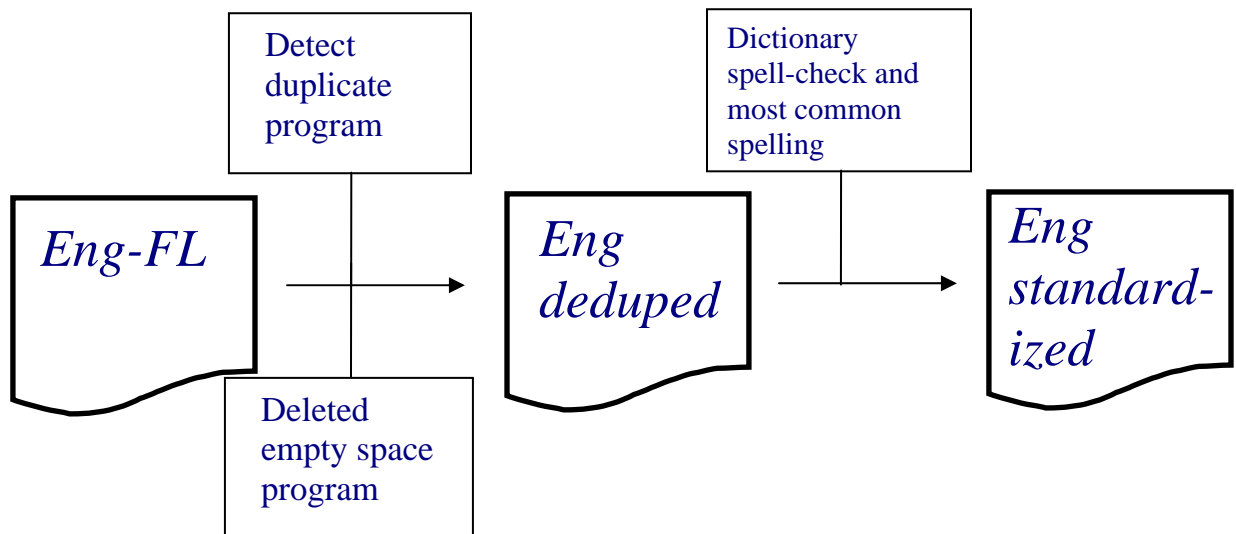
Figure 1. Internal correction process.

Once we became familiar with the term base, we determined that it had to be altered in order to accurately process the material. The list of problems identified in the introduction was used to refine existing text. First, the terms were alphabetized. Entries that had unnecessary preceding

white space were fixed. Microsoft Office was unable to remove trailing white spaces, so Perl was used for this purpose. The code removed all white space after each string in the text file and replaced the new entry in the dictionary.

Once the alignment and spacing errors were corrected, both a Perl script and Conditional Formatting within Microsoft Excel were used to identify all exact matches within the column of terms. Both methods identify a total of 331 duplicates in the English portion. Taking the entire dictionary into context, there were 33 duplicate entries (some entries were found three separate times); therefore, 37 entries were removed.

In response to the variations among words in the dictionary, we decided to include both entries to find the most common spelling in order to eliminate one of the entries later in the project. Misspellings were then corrected to help reinforce standardization of the term base. We also removed the unnecessary symbol following three of the entries.

Entries with two separate terms combined and submitted as one entry were noted (i.e., antiaircraft/artillery, director/directorate). These submissions should be separated into two entries for the purpose of accessibility in the field, and in our term frequency method, exact string matching is essential for accurate results. Therefore, all entries with gratuitous explanations and definitions following the term were removed. A Microsoft Excel macro was employed to eliminate all items within parentheses.

Once these alterations were completed, the new term base consisted of the following breakdown:

WPL: 1	AOL: 1832	WPL: 9	AOL: 3
WPL: 2	AOL: 4795	WPL: 10	AOL: 3
WPL: 3	AOL: 1591	WPL: 11	AOL: 3
WPL: 4	AOL: 440	WPL: 13	AOL: 2
WPL: 5	AOL: 182	WPL: 14	AOL: 1
WPL: 6	AOL: 83	WPL: 16	AOL: 2
WPL: 7	AOL: 24	WPL: 18	AOL: 1
WPL: 8	AOL: 15	WPL: 19	AOL: 1

WPL: Words per Line

AOL: Amount of Lines

4. Method One: Frequency Count

This proposed method to collection a set of domain-specific terminology is based on the principle of Term Frequency-Inverse Document Frequency (TF-IDF). As tested in *An Unsupervised Approach to Domain-Specific Term Extraction* (*3*), the principle behind frequency counting is the idea that certain terminology will generally occur with a higher frequency within domain-specific documents as opposed to in a general corpus. This theory, however, has its limitations. Single word terminology is much more difficult to access based on the occurrences of homographs. In the NVTC's dictionary for example, the entry "brief" could be found in several different contexts. In a military sense, the term can be used as a verb to summarize or give preparatory information to Soldiers, but in a general connotation, it could be used as an adjective or noun to describe duration and length.

4.1 Input

A domain-specific corpus of 2619 documents was then created by collecting various military documents from a variety of sources. The documents selected were chosen because of their translated nature; if a document was important enough to military use that it was translated into Arabic, then its extracted terminology is most likely vital to a bilingual dictionary. Thirteen items from the Ranger Handbook, one item from field manual 3-21.10, and five items from field manual 7-8 were selected, along with 93 documents from the Combating Terrorism Center's Harmony Database of Released Documents (CTC) and 2507 items from an Iraqi database from ARL's holdings. The CTC at West Point, dedicated to scholarly research and policy analysis to examine combat terrorism, published a series of letters, reports, and al-Qa'ida-related documents captured during the War on Terror for public access. This is important to our corpus as a first-hand account of events in Afghanistan, elucidating al-Qa'ida's actions and weaknesses. The Iraqi training material consists of PowerPoint training materials, scripts, and guides to a variety of field situations.

4.2 Output

The goal of this method was to take the internally cleaned dictionary and use exact string matching to search through the corpus for the number of occurrences of each term. Because of the extensive nature of the corpus, we used a Hadoop cluster, a programming framework designed for large-scale computational use, to expedite the process. Before processing the data, all the documents (Acrobat Reader, Microsoft Word, Microsoft Excel, and Microsoft PowerPoint) were converted into text files with the help of an online converter. The Iraqi training documents could not be easily converted, however, because of the high number of subfolders

within each main folder. Again using Perl, we renamed all documents, changing spaces to dashes and ampersands to underscores, and moved all documents to one large folder, which helped ease the conversion of the files.

Once all target files were converted, they were processed with the servers searching for exact string matches based on the dictionary's terms. The process resulted in two Excel files summarizing the findings. The first, "Word Count" (table 1), was a list of all keywords, the number of occurrences in the corpus, and on average how many times that keyword appeared per document. The second file, "Doc Count" (table 2), consisted of a list of each document, the number of key words in the document, and the average number of times a keyword appeared.

Table 1. Word Count chart excerpt.

Term	No. of Times Term Appears in Corpus
Map reconnaissance	16
Fallout	16
Psychological warfare	16
Stud	16
Barrel assembly	16
Medical unit	15

Table 2. Doc Count chart excerpt.

Document	No. of Terms in Dictionary that Appear in Corpus
Iraqi-Training-Disk_S3_MOUT_ Infantry-Rifleman-Course-Handout-Booklet-2003.txt	462
Iraqi-Training-Disk ca-documents_ instant-lessons-of-iraq-war.txt	458
AFGP-2002-600092-Trans-Meta.txt	448
Iraqi-Training-Disk_ca-documents_SASO-handbook.txt	434
AFGP-2002-600088-Trans-Meta.txt	371
AFGP-2002-600053-Trans-Meta.txt	361

The results from the TF method indicated that the most common terms were as follows:

One-word entries	Enemy	8622
	Support	5254
	Commander	4889
	Operations	4874
Two-word entries	First aid	448
	Armed forces	389
	Indirect fire	340
	Warning order	316
Three-word entries	Course of action	364
	Command and control	310
	Chain of command	306
	Concept of operations	216

The results support Zipf's Law (*4*) that term length is inversely proportional to its number of occurrences in a corpus. Zipf's Law will become an important factor in the term extraction process. We found 29.68% of all terms in the dictionary with a frequency of one or more in the corpus and 26.13% of those appeared more than once.

5. Method Two: Terminology Extraction

The goal of terminology mining or extraction is to collect a list of domain-pertinent terms from a given corpus. For the purposes of this investigation, the online extraction tool TermExtractor (*5*), developed by the Linguistic Computing Laboratory of the University of Roma, was used to determine what percentage of the extracted term list overlapped with the existing military bank.

The terms that appear in both corpora are then added to a proposed list of confirmed dictionary entries. Figure 2 shows the TermExtractor pipeline.
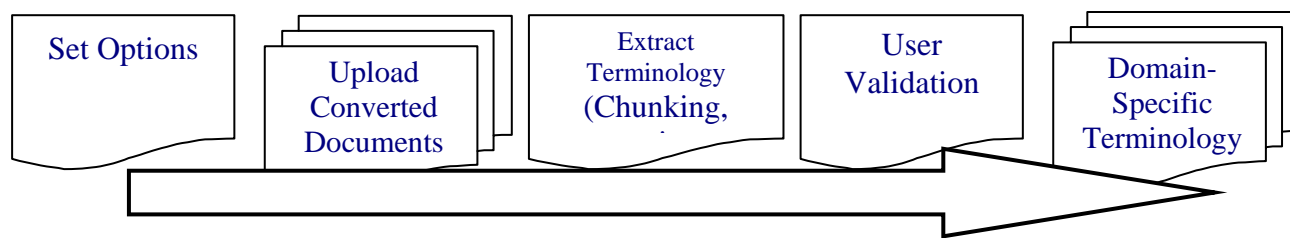
Figure 2. TermExtractor pipeline (*5*).

To ensure consistency in our results, we used the same corpus as a reference throughout the entire project. We submitted the same corpus of 2619 documents as in the TF method to be processed for specificity. TermExtractor uses input documentation to extract statistically relevant terminology through the use of chuncking and document parsing, as well as by filtering unecessary information. These filters eliminate stopwords such as "the, as, is, for" and general terminology that does not indicate domain-specificity. The extraction tool filters non-terminological strings through its evalution of the following:

- **Domain Pertinence**: High (numerical value) means a term is frequent in the domain of interest and is much less frequent in the other domains used for contrast (*6*):

$$DRDi\ (t) = -\sum P\hat{\ }(t\ /dk)\ \log(P\hat{\ }(t\ /dk\ )) = \sum norm\_freq(t,dk) \log(norm\_freq(t,dk))$$

- **Lexical Cohesion:** The degree to which the terms adhere to one another within a string. This proved more effective than other measures of cohesion (*6*). The resulting numerical value is high if the words within a string occur more often with one another rather than alone in a corpus. The minimum was set to 0.05.

- **Structural Relevance:** When a title or subtitle is composed of domain-specific terms, then its importance is increased by some factor *x*. Highlighted, bolded, and italicized items are also included *(x*=5 for highlighted, capitalized, underlined, colored, smallcaps, italicized, and bolded terms*, and x*=10 for titles and abstract content*)*.

- **Miscellaneous:** A set of heuristics are applied to increase computational performance by removing generic articles and terminology, detecting misspellings, distinguishing part of speech, extracting unigram terminology, and detecting abbreviations.

The extraction tool also sets up contrastive corpora to eliminate common terminology that may be relevant to the specific domain but not entirely of that domain. These corpora include the following:

- Brown Corpus (3634 terms)

- Medicine (2281 terms)

- Computer Networks (16335 terms)

- Sports (1020 terms)

- Tourism (55590 terms)

- Wall Street Journal—Economy (3606 terms)

Although these terminology banks are not specifically indentified, it is important to set up some contrasting corpora to eliminate general terminology and possibly create a proposed list of terms for expulsion.

5.1 First Investigation

In the first investigation, the corpus was submitted without any restrictive measures to find the percentage of extracted terminology that would overlap with the existing term bank. Given Zipf's Law (*4*), the frequency distribution of word length is exponential; this means that, in accordance with a general corpus, a unigram (one word term) is far more likely to occur than a bigram and a trigram, and so forth. Due to time constraints, this law was employed, so any term that exceeded three words was considered domain-specific because of its exclusivity to a particular domain. For all one- to three-word terms, 3605 words occurred in both the term extraction list and the NVTC dictionary. This indicates that 40.27% of the dictionary is supported by this method; 43.87% of all unigrams, bigrams, and trigrams.

5.2 Second Investigation

For the second investigation, we entered the corpus and entered the existing term bank as a restrictive option. The extracted terminology from this trial excludes all terms in the dictionary in its proposed terminology list. At this point in the process, a human validator is required to identify the reliability of the extracted list. I randomly sampled 10% of the terms (648 items) and a subject matter expert evaluated this list, indicating whether the term was military-unique (18.06% of the sample) and highlighting the spelling errors (24.07%). Table 3 is an excerpt of the described process, with its proposed spelling corrections in column four.

Table 3. Methods comparison to dictionary.

Term	Military Specific	Spelling Error	Possible Correction
improvised sling	Yes		
include-ytank crewmembers	Yes	Yes	"including tank crewmembers"
includingthe regulationsandlaws		Yes	"including the regulations and laws"
indecision recklessness			
index contour line	Yes		

This list will be used later as a basis for what could be added to the dictionary. In order to refine the extracted list of terms, the same course of action can be taken as for the NVTC dictionary. The possible list of terms can be evaluated for its frequency in a new corpus and a new list of terms can be extracted and compared for its similarities.

6. Results

Although time constraints did not allow the full investigation to be executed, the original term base can be successfully modified and refined after comparing the dictionary with a general corpus and using IDF. The first portion of figure 3 indictates the overlap between the orignial NVTC dictionary and the results of the two methods. It appears that the TF method produces a better comparison to refining an existing military term base, but the term extraction method contributed as well. The second portion of figure 3 indicates the overlap between the TF method and the term extraction method.

Pt. 2
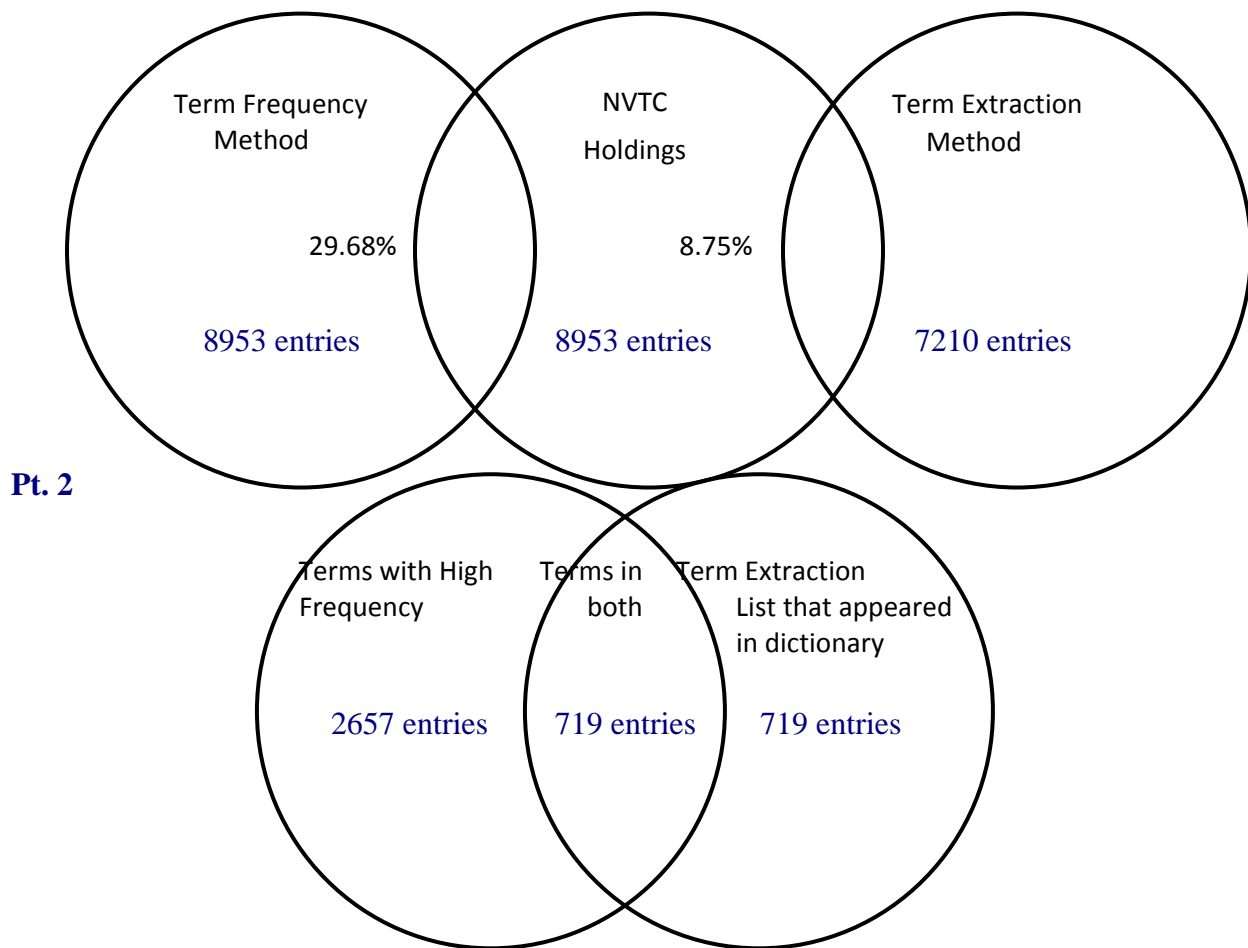
Figure 3. Comparison to dictionary.

In this study, 27.06% of terms that appeared with high frequency also appeared in the term extraction list.

In addition to assessing the term frequency of the dictionary when paired with a military-specific corpus, we also would like to compare the dictionary with a general corpus, such as English GigaWord. This process would not validate terms, but rather would propose a possible list for exclusion. By processing the dictionary with a general corpus, we would be able to eliminate general terms, but also single-word terms that occur frequently in both a general corpus and a military-corpus. These unigrams must be verfied with a human ground truth because of the appearance of homographs, as mentioned earlier.

The third proposed method that we plan to execute following this paper is IDF. The problem with TF measurements is that all documents and expressions are considered equally important in terms of assessing relevancy. IDF works to solve this problem along with TF by statistically identifying how important a word is to a corpus. If the TF-IDF is high, it indicates a rare term; it is considered low when terms occur frequently.

7.   Conclusion

As of the moment, we have 46.70% of the dictionary accounted for as a result of the TF/term extraction methods, as well as a portion dedicated to Zipf's Law (8.27%). After all the previously mentioned methods have been executed, we hope to have a refined, efficient dictionary that will be useful in the field as well as for more computational research.

8. References

1. Avancini, H.; Lavelli, A.; Magnini, B.; Sebastiani, F.; Zanoli, R. Expanding Domain-Specific Lexicons by Term Categorization, *Proceedings of SAC*, Melbourne, FL, 2003.

2. Jordan, Everette E. Congressional Testimony. Federal Bureau of Investigation, 25 Jan 2007. [ONLINE]. http://www.fbi.gov/congress/congress07/jordan012507.htm (accessed 23 Jun 2010).

3. Kim, S. N.; Baldwin, T.; Kan, M.-Y. An Unsupervised Approach to Domain-Specific Term Extraction, ALTA Workshop, 2009.

4. Pierce, J. R. *Introduction to Information Theory: Symbols, Signals, and Noise,* 2nd rev. ed.; New York: Dover, 1980, pp 86–87, 238–239.

5. Sclano, F.; Velardi, P. TermExtractor: a Web Application to Learn the Common Terminology of Interest Groups and Research Communities. *9th Conf. on Terminology and Artificial Intelligence TIA 2007*, Sophia Antipolis, France, October 2007.

6. Park, Y.; R. J. Byrd, R. J.; Boguraev, B. K. Automatic glossaryextraction: Beyond terminology identification. *Proceedings of the 19th International Conference on Computational Linguistics*, Taipei, Taiwan, 26–30 August 2002, 772–778, Association for Computational Linguistics (ACL), http://www.aclweb.org/anthology/C/C02/C02-1142.pdf.

Sensors and Electron Devices Directorate (SEDD)

INTENTIONALLY LEFT BLANK.

U.S. Army Research Laboratory
SUMMER RESEARCH TECHNICAL REPORT

Thermal Analysis and Novel On-Chip Velocity Characterization of Energetic Porous Silicon with Sodium Perchlorate Oxidizer

COLLIN BECKER
LUKE CURRANO
RDRL-SER-L, BUILDING 207, Z2A-46-12

Contents

List of Figures

Abstract

When a solution of sodium perchlorate (NaClO$_4$) in methanol is drop-cast onto porous silicon (PS) and dried under nitrogen (N$_2$), an explosive reaction can be initiated by heat, friction, or electrical spark. As a means to yield high-performing energetic porous silicon on-chip, a galvanic corrosion process is demonstrated. This is a major advancement for energetic porous silicon, offering a more flexible approach to integration than previous work using electrochemical etching. The new galvanic process has no requirement for electrical connection to the wafer during pore formation and is compatible with many more materials than the electrochemical etch process. Here, PS films up to 150 μm thick are fabricated on p-type Si wafers. Bomb calorimetry reveals PS-NaClO$_4$ to be a fuel-rich energetic material with a heat of reaction below the theoretical value. The reaction velocity is studied by pattering thin-film resistor wires across PS strips 3 mm wide and up to 75 mm in length. An oscilloscope monitors the wires during the energetic reaction, and the time to failure is used to determine the speed of the reaction. The results indicate that velocity is on average 2130 m/s but can fluctuate hundreds of m/s along the length of the chip.

Acknowledgments

INTENTIONALLY LEFT BLANK.

1. Introduction/Background

The development and tailoring of new energetic materials is critical to the success of explosives, propellants, micro-actuation, and power for next generation Department of Defense (DoD) weapons and microsystems. In particular, a material that is compatible with and integrated into microelectromechanical systems (MEMS) could greatly advance the current state of the art in MEMS fuzing, propulsion, and power applications. Advances in the relatively young field of nanoenergetics have begun to make this on-chip integration a reality (*1*). Nanothermites and energetic porous silicon (PS) are the two main focus areas in the field of nanoenergetics. Nanothermite work investigates the effects of scaling traditional thermite materials, generally aluminum and an oxidized metal, such as iron oxide, to the nanoscale. Current studies have shown improved reaction rate—i.e., increased burn rates—compared to macroscale thermite materials (*2, 3*). Additionally, a micro-heater has been realized using a nanothermite approach (*4*).

The work in this report focuses on energetic PS, a widely studied material that holds great potential in the realization of novel MEMS, including chemical and biological sensors, and optoelectronics. When impregnated with any one of a number of oxidizers, PS can function as an energetic material. Because silicon (Si) is widely used in micromachining and complimentary metal-oxide-semiconductor (CMOS) processes, PS can be integrated on-chip alongside a MEMS sensor. This new class of energetic material can be used for applications requiring on-chip power, propulsion, and fuzing. The strength of the energetic reaction is controlled by altering processing parameters to tune PS thickness, porosity, specific surface area, and surface terminations.

In general, PS begins as a single- or polycrystalline Si wafer and is anodically etched in a hydrofluoric (HF) acid environment by applying an electrical bias to the Si. The end result is a film that is a few hundred nanometers to several hundred microns thick and composed of a network of pores ranging from a few nanometers to several microns in diameter. Alternatively, the film can be classified as being composed of Si nanocrystals. The specific surface area of the material can be as high as $1000 \text{ m}^2/\text{cm}^3$.

For energetic PS, the pores are filled with a strong oxidizer, such as a perchlorate salt dissolved in methanol or molten sulfur. After the methanol evaporates or the sulfur dries, the pores are filled with the solid oxidizer. By applying heat, mechanical force, or a spark, the material readily ignites with a bright flash of light and a loud bang approaching 120 decibels (dB), for only a few milligrams of material.

Early reports on energetic PS were primarily qualitative in nature and proposed reaction mechanisms—i.e., the qualitative strength of the reaction (as judged by flame size and how loud

of bang is produced) with several solid oxidizers (*5, 6*). One report proposes an optimal pore size for the most energetic reaction (*5*). More recently, attempts at differential scanning calorimetry (*7*), traditional calorimetry (*8*), and Fourier transform infrared spectroscopy (FTIR) (*9*) have been made. Additionally, one report presents work on nanoporous Si particles of several microns in diameter and reports ignition by partial filling of pores with CuO nanoparticles (*10*). Most recently, from the U.S. Army Research Laboratory (ARL), on-chip integration of energetic PS with a MEMS sensor is reported (*11*).

In general, however, there is still very little quantitative work documenting energetic PS, and it is quite possible that the full potential of this material is not being realized. There are thousands of journal articles that document PS (interest peaked when it was found that PS photoluminesces), and these papers highlight dozens of characterization techniques, etch recipes, and material properties. The nanoenergetics field has to yet to truly apply this knowledge base to energetic PS. To this end, a focused research effort is being conducted at ARL to characterize nanoenergetic PS with a complete suite of investigations.

With the knowledge gained from the nanonergetic PS characterization, an on-chip integration of the material can be realized. Current work from ARL uses a process that can result in damage to the PS and other materials on the wafer during device fabrication. As a possible way of avoiding this damage, a galvanic cell composed of Si and platinum (Pt) in a hydrofluoric acid-based electrolyte is used to generate PS. While the galvanic cell method of PS formation is not new, we have been able to create films up to 50 microns thick that are stable, highly compatible with device fabrication steps, and suggest an energetic reaction that proceeds faster than in PS generated from a standard anodic etch process. This is also the first report of thick (tens of microns) galvanic PS in 10 ohm-cm Si wafers. We duplicated work that generated thick PS films in 0.01 ohm-cm wafers (*12*), but these show non-uniform etch rates across the exposed Si surface and yield qualitatively slower energetic reaction rates compared to the 10 ohm-cm wafers.

2.   Experiment/Calculations

Briefly, PS is typically made via an anodic etching process in a hydrofluoric (HF) acid-based electrolyte (*13*). A doped Si wafer of n- or p-type serves as the anode, and a metal electrode that is inert (typically gold (Au) or Pt) in an HF environment functions as the cathode. The Si and metal are electrically connected, and a current density ranging from a few mA/cm^2 to several hundred mA/cm^2 is passed such that oxidation occurs at the Si surface. As the etch proceeds, pores ranging from a few nanometers to hundreds of nanometers are produced. The thickness and pore size of the PS layer is controlled by current density, electrolyte composition, the dopant type, the Si resistivity, and the etch time. Figure 1 shows the setup of a typical etch cell, in which a silicon wafer is sandwiched between a Teflon compartment containing an HF-based

electrolyte and a bottom block of Teflon. The o-ring serves to prevent leakage of the electrolyte. Two typical optical images of PS (1 cm^2 area) formed in an etch cell are shown. The conditions used in this report typically result in a black, reddish brown, or blue (not shown) PS.
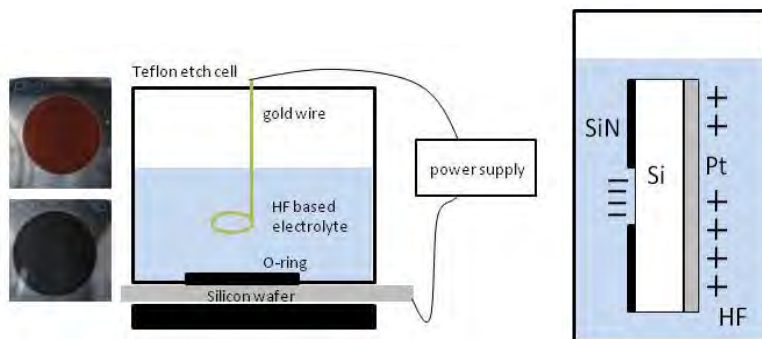
Figure 1. (L) Typical etch cell composed of Teflon electrolyte chamber, a Au wire cathode, silicon anode, o-ring, and powersupply. Two optical images of PS are included. (R) Galvanic cell arrangement showing ionic charges (reduction at the Pt cathode, oxidation at the Si anode). Si$_3$N$_4$ acts as the etch mask in HF.

Alternatively, PS can be generated using a galvanic process that results in autonomous current generation between electrically connected Si and an HF-resistant metal (Au or Pt), as shown in figure 1 (*14, 12*). In this process, no power supply is needed. The open circuit potential (OCP) of Si and Pt differ in an HF-based electrolyte. When electrically connected, Pt raises the OCP of Si, and it has been shown by electrochemical techniques that the dissolution of Si (forming of pores) is realized (*14*). Reduction of the oxidizing agent (either dissolved oxygen in solution or addition of a strong oxidizer, such as hydrogen peroxide) at the metal cathode drives the current. The autonomously generated current is affected by electrolyte composition and surface area ratio (SAR) of metal to exposed Si.

In this work, we use sputtered Pt directly on a 1–10 ohm-cm resistive wafer as the metal contact. Pt has a much larger reduction current than does Au when H$_2$O$_2$ is used as an additive. Additionally, we have found the Pt can withstand over 30 min of immersion in HF/EtOH/H$_2$O$_2$. Ethanol is used as a surfactant to aid in wetting of the Si. Other surfactants, such as the commercially available Triton X-100 that has been used in other works (*15, 14, 16*), were tested with some success. Patterned Si wafers using a Si$_3$N$_4$ mask and a sputtered Pt film on the back of the wafer were used to fabricate 2 mm diameter PS devices. In the case of the 2 mm devices, the SAR is about 2.4, whereas a single crystal wafer with a Pt film on the backside has a 1.0 SAR.

FTIR (Nicolet, Thermo-Fisher Scientific) is used to monitor changes in PS composition as a result of different preparation methods or treatments. We use FTIR in reflection mode with a diamond window, attenuated total reflection (ATR) fixture. Specifically, we study the role of oxidation in an O$_2$ atmosphere at 250 ºC for 60 s in a rapid thermal anneal (RTA) tool.

Calorimeter data (Parr Instruments, 1109 semi-micro bomb), in conjunction with pressure measurements of the evolved gas from the energetic PS reaction, is presented, revealing how energy output and gas generation change with Si oxidation prior to ignition.

3. Results and Discussion

3.1 FTIR Characterization of PS

The actual cause of the rapid exothermic reaction of PS with a solid oxidizer is thought to result from a region of bare Si nanocrystal becoming exposed to the oxidizer. The high concentration of a strong oxidizer in the presence of exposed Si, which has a higher exothermic energy release after oxidation than carbon, leads to a rapid chain reaction with a large energy release occurring in milliseconds. "Fresh" PS—PS only several hours old or less—exhibits a hydrogen-terminated Si surface that prevents the slow oxidation of the Si nanocrystals in the ambient environment. It is also thought that the hydrogen is what leads to the gas evolution during ignition of the nanoenergetic PS. From rudimentary tests in which a mass is propelled from the surface of a PS ignition, it is evident that gas is being generated from the reaction. Equation 1 is proposed as the reaction equation for nanoenergetic PS without consideration of any other species, such as hydrogen or crystalline water, in the oxidizer. Since the reaction products of the fuel, Si, and the oxidizer, $NaClO_4$, are all solid, the gas evolution must be coming from another source.

$$2Si + NaClO_4 \rightarrow 2SiO_2 + NaCl \tag{1}$$

Generation of hydrogen gas and water vapor as a result of the hydrogen surface termination being driven is likely (*8*). One source suggests that a mild oxidation of PS does not diminish the exothermic energy release after ignition; it may improve stability of the removing relatively weak Si-H bonds by either forming O-Si-H or removing all of the Si-H to form a thin SiO2 layer (US patent: 6984274). Figure 2 shows FTIR data of "fresh" and oxidized (details described in the experimental section) Si. Two variants of PS Si are shown: (1) PS from an electrochemical etch at 20 mA/cm2 for 30 min in 1:1 (49% HF:EtOH by volume), and (2) PS from a galvanic process etched for 20 min in 1:11:22 (70% H2O2:EtOH:49% HF by volume), with a 1.0 SAR of Pt to Si.

The relative peak intensities in figure 2 reveal that the oxidation performed in relatively mild conditions and short time does not completely remove the hydrogen termination, but there is a clear increase in Si-O bonds, indicative of a partial oxidation of the surface. It is also noted that the susceptibility of the PS to accidental ignition by mechanical stimulation did decrease as suggested in (US patent: 6984274). The two methods of PS preparation yield similar FTIR data, with the galvanic process showing a slight resistance to oxidation, as the height of the peaks at 2100 cm^{-1} did not diminish as much as the electrochemical etch.
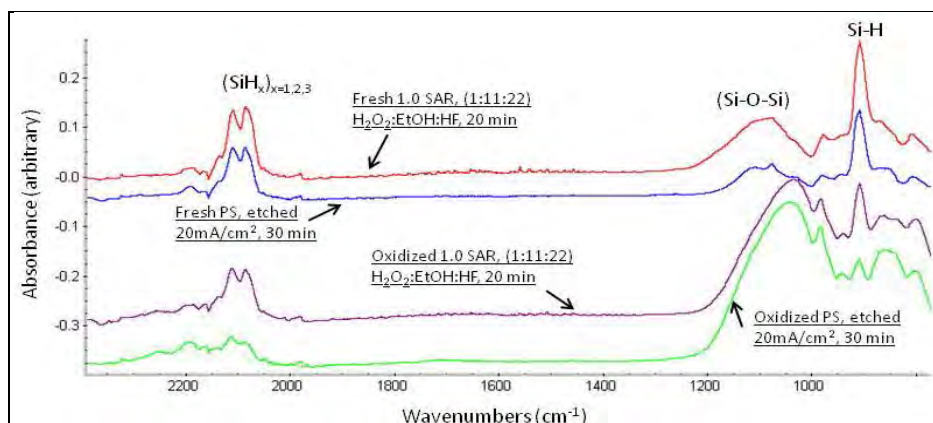
Figure 2. FTIR of "fresh" and oxidized PS from a standard electrochemical etch and a galvanic etch process.

3.2   Calorimetry of PS

To determine the effect of oxidation on energetic PS, calorimetric measurements of "fresh" and oxidized PS with $NaClO_4$ oxidizer were made. In each case, the pressure evolved from each reaction was measured in a separate experiment using a standard pressure gauge connected to the Parr calorimetry bomb. Figure 3 shows the temperature rise as a function of time; both variants of PS show similar behavior. The exothermic energy from each reaction is very similar at 5.4 kJ/g for oxidized PS and 5.7 kJ/g for "fresh" PS.
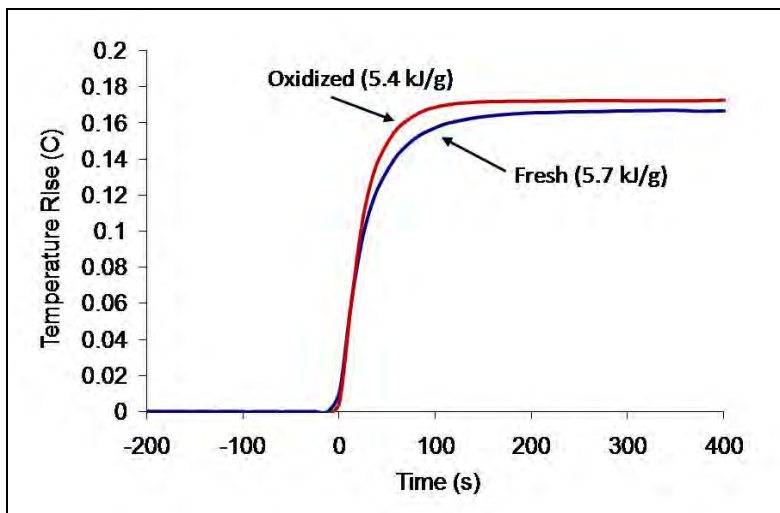
Figure 3. Temperature rise during bomb calorimetery.

The two variants differ dramatically in gas volume generated. "Fresh" PS yields about 0.0129mol/g, whereas the oxidized Si generates about 0.004 mol/g. This suggests that the hydrogen termination plays a significant role in gas generation, but minimally affects the exothermic energy of the reaction. This discovery is likely to provide avenues for "tuning" the gas generation of the reaction for different applications. Further analysis and testing of additional

69

PS variants are required to fully understand this result, but initial propagation rate studies, from high speed video analysis, indicate that the oxidized sample reacts slower than the "fresh" sample.

Additionally, higher propagation speeds can be correlated to louder energetic reactions (120 db+), and both the "fresh" and galvanic PS achieve the loudest ignitions. The galvanic PS especially is highly reproducible in ignition sound, with even the 2 mm devices producing a large flash and loud bang.

3.3 On-chip, Nanoenergetic Galvanic PS

Energetic PS devices are currently realized by using a Si_3N_4 etch mask to pattern a Si wafer. Next, an electrochemical etch fabricates PS in the exposed regions of the Si_3N_4 mask. Finally, a metal bridgewire (shown in figure 4a) is patterned on the PS. A current can be passed through the bridgewire to cause localized heating of the PS and subsequent ignition when oxidizer is present. During the processing steps to realize these devices, the PS is degraded and large cracks are formed that can result in bridgewire damage (figure 4b). Additionally, the etch depths are limited by this process.
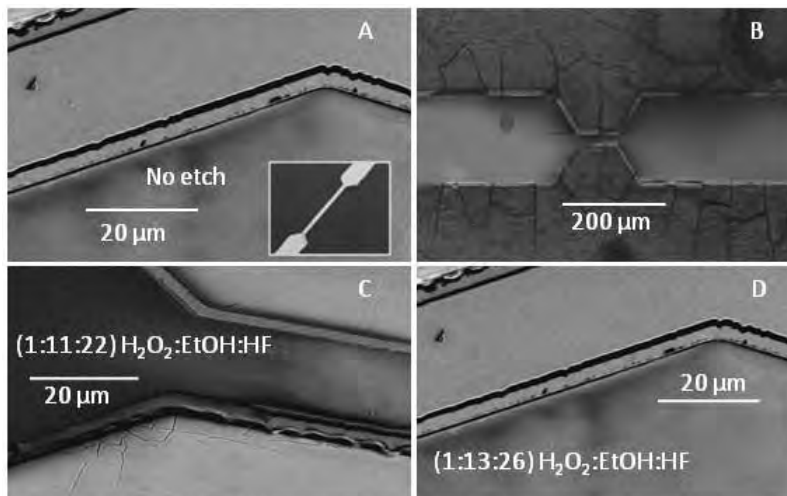
Figure 4. SEM images. (a) Bridgewire deposited on bare Si; inset) expanded view of bridgewire. (b) Bridgewire deposited on electrochemically etched PS. (c,d) Bridgewire after galvanic PS generation. The higher H_2O_2 concentration in (c) results in a more aggressive etch than an (d).

In an effort to realize structurally stable PS and more reliable bridgewire structures, as well as to reduce the number of processing steps and increase device yield per wafer, galvanic PS generation was used to create PS films on the order of 20–50 µm thick with limited bridgewire degradation. In this process, the bridgewire is patterned on bare Si that is then galvanically etched to generate PS. Results indicate that the bridgewire remains intact, and the PS is structurally stable with limited cracking present.

Figure 5 presents SEM cross section images of galvanic PS with different SAR and different electrolyte compositions. The etch depth increases both with increasing H_2O_2 concentration, as well as SAR. Additionally, HF concentration and EtOH concentration affect the structural integrity of the film. The wafer resistivity also drastically affects the PS film quality and etch depth. More results are needed to develop a more exact correlation of SAR and electrolyte composition to film thickness and quality, but these preliminary results indicate that it is possible to generate stable porous Si layers at least 50 μm thick using the galvanic process.
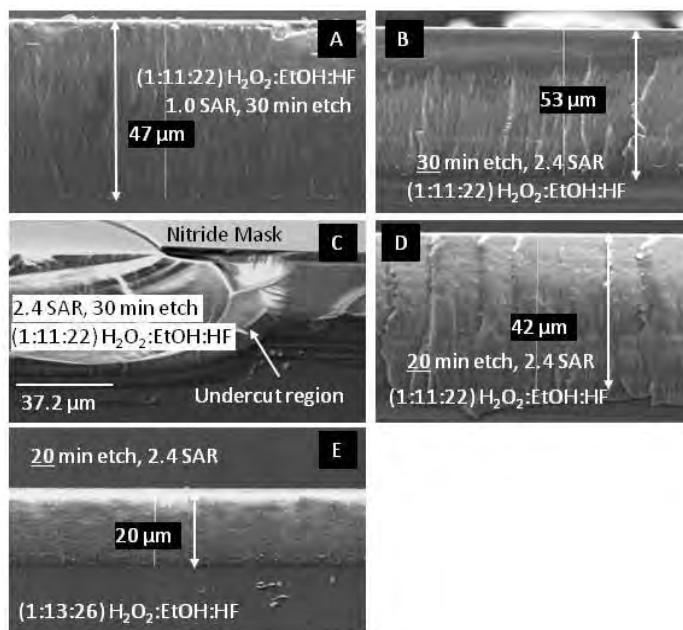
Figure 5. SEM cross section images of galvanic PS with different SAR and different electrolyte compositions.

Currently, appropriate galvanic etch conditions have been used to fabricate stable PS films after bridgewire deposition. These devices have been wirebonded such that ignition can be tested. While no quantitative data has been attained, the reaction propagation velocity in small devices (2 mm diameter) appears to be much greater than the standard electrochemical PS devices. Additionally, the bridgewire is of high quality and less prone to failure due to cracking of the porous film. This process is still very young but could realize very unique device architectures, faster device fabrication, and more reproducible ignitions.

3.4 On-chip Velocity Measurements

The velocity at which the energetic reaction between PS and $NaClO_4$ proceeds is an important parameter. The velocity indicates if the material is truly detonating or is slowly burning. Molecular energetic materials contain the fuel and oxidizer in one molecule and, thus, oxidation occurs extremely quickly. Reaction velocities of these materials approach 10 km/s. The PS-$NaClO_4$ is not expected to reach this velocity since the reaction involves the decomposition of $NaClO_4$ prior to oxidizing PS. However, modifying the PS morphology, either through etching

conditions or with heat and chemical treatments, is expected to change the velocity of the reaction.

High velocity, explosive reactions are often studied with a high speed camera, but this is a time-intensive and costly technique. For an on-chip measurement, resistive wires that are very similar to the initiator wire previously discussed are lithographically patterned on the PS. The reaction is initiated at one of the chip, and as it progresses, it breaks the wires, as shown schematically in figure 6. Initially, 9 V is applied across the wires, and this voltage is monitored with an oscilloscope. The voltage drop at each wire is broken.
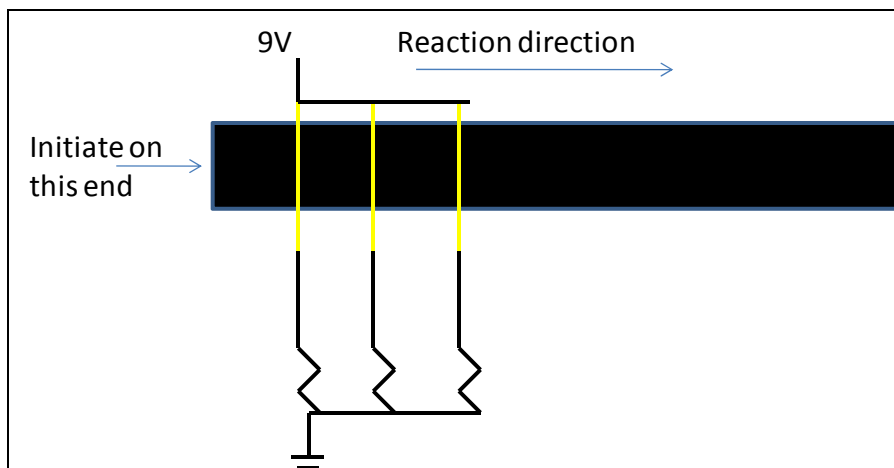
Figure 6. Schematic of on-chip velocity measurement.

A representative plot of the wires failing is shown in figure 7. The reason for the increase in the voltage after the wires fail before once again settling to 0 V could relate to either properties of the oscilloscope or effects from the energetic reaction reconnecting the wires via conductive plasma. For a SAR of 5.2–6.4, the velocity is, on average, 2130 m/s. This velocity can fluctuate hundreds of m/s along the chip, however. This may relate to areas where $NaClO_4$ dries differently or is not reacting with the PS in the same manner as other regions. Initial work reveals that when low concentration $NaClO_4$ is used (0.8M–1.6M), the reaction velocity slows to hundreds of m/s and, in some cases, tens of m/s. Additionally, high speed video analysis should be conducted alongside these measurements to verify some of the findings, although the average velocity presented here is within an expected range (9). Alongside calorimetric data, this velocity test can be performed to gain insight into how PS morphology, surface termination, or use of an oxidizer other than $NaClO_4$ affects the reaction.
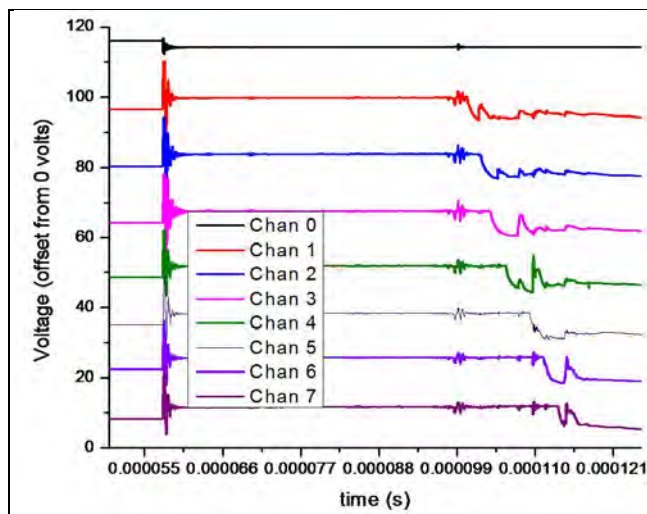
Figure 7. Representative velocity data from the on-chip
measurement with wire spacing of 5 mm.

4. Summary and Conclusions

Nanoenergetics is a very young field of research, and limited quantitative data and material characterization is presented in the literature. The focus of this report is nanoenergetic PS. Calorimetry, FTIR, SEM, and velocity data are presented for several variants of PS. Quantitative data will aid in the ability to fine-tune the PS morphology to yield desired gas volume, propagation speed, and energy density. A new galvanic process to form energetic PS is introduced, and initially suggests an easier, faster, and more reliable route to on-chip integration. Additional benefits seem to include increased propagation rate and more reliable bridgewire structures. Future work will include further study into the structure of PS and how it affects velocity and energy yield.

5. References

1. Rossi, C.; et al. *Journal of Microelectromechanical Systems*. **2007**, *16* (4), 919–931.

2. Ferguson, J. D.; et al. *Powder Technology*. **2005**, *156* (2005), 154–163.

3. Apperson, S.; et al. *Applied Physics Letters*. **2007**, *91*, 243109.

4. Zhang, K.; et al. *Journal of Microelectromechanical Systems*. **2008**, *17* (4), 832–836.

5. Du Plessis, M. *Phys. Stat. Sol. A*. **2007**, *204* (7), 2319–2328.

6. Clement, D.; et al. *Phys. Stat. Sol. A*. **2005**, *202* (8), 1357–1364.

7. Churaman, W.; et al. *Chemical Physics Letters*. **2008**, *464*, 198–201.

8. Currano, L.; Churaman, W.; Becker, C. *Transducers Conference,* Denver, CO, 2009.

9. Churaman, W.; et al. *Journal of Physics and Chemistry of Solids.*, *71*, 69–74.

10. Subramanian, S. *ASC 2008*.

11. Currano, L.; Churaman W. *Journal of Microelectromechanical Systems., 18*. 799–807.

12. Splinter, A.; et al. *Sensors and Actuator*. **2001**, *92*, 394–399.

13. Canham, L.; editor. Properties of Porous Silicon, 1997.

14. Ashruf, C.; et al. *Sensors and Actuators*. **1999**, *74*, 118–122.

15. Becker, C.; et al. *Journal of Micromechanics and Microengineering,* In press.

16. Miller, D.; Becker, C.; Stoldt, C. *Journal of the Electrochemical Society*. **2008**, *155* (12), 253–265.

U.S. Army Research Laboratory
SUMMER RESEARCH TECHNICAL REPORT

Determination of Truncated Peptide MRE Binding to Protective Antigen Protein Using Enzyme-Linked Immunosorbent Assay (ELISA)

IRENE VAL-ADDO
DR. JOSHUA KOGOT
RDRL-SEE-O

Contents

List of Figures

List of Tables

Abstract

The protective antigen (PA) protein secreted by the *Bacillus anthracis* bacterium combines with either edema factor or lethal factor protein to form either edema toxin or lethal toxin. Since PA is necessary to the formation of both toxins, it can be used as a target to detect the presence of *B. anthracis*. Because antibody-antigen detection methods are time consuming and require specific conditions for testing, alternative methods, such as peptide-antigen detection, are being considered. Enzyme-linked immunosorbent assay (ELISA) is commonly used to test for binding affinity of proteins and enzymes, and employs the use of visible detection of substrate-enzyme reactions. Binding affinity is quantified based on the dissociation constant (K_D) of a peptide-antigen or antibody-antigen complex, with low K_D values representing high affinity. A fluorogenic substrate was reacted against a 15-amino acid peptide bound to a PA-enzyme conjugate using the ELISA method. The determined K_D for the peptide was in the range of 680–728 nM, while the binding antibody specific to PA was in the range of ~3–5 nM. Truncated segments of the full-length peptide will be tested to determine a sequence with the highest binding affinity to PA, providing a more efficient alternative for field use.

Acknowledgments

I wish to acknowledge the mentorship of Dr. Joshua Kogot.

INTENTIONALLY LEFT BLANK.

1. Introduction/Background

Following its use in 2001, *Bacillus anthracis* and its associated toxins have received much attention. *B. anthracis* secretes three distinct proteins, identified collectively as anthrax toxin: edema factor (EF, 89 kDa), lethal factor (LF, 90 kDa), and protective antigen (PA, 83 kDa). Cleaving of PA_{83} on the cell surface into PA_{20} and the activated PA_{63} protein by furin proteases exposes binding sites for EF and LF (*1, 2*). PA is easily passed through the cellular membrane, and thus any bound EF or LF protein can be introduced inside the cell and undergo its respective biological toxins—edema toxin (EdTx) and lethal toxin (LeTx) (figure 1) (*2–4*).
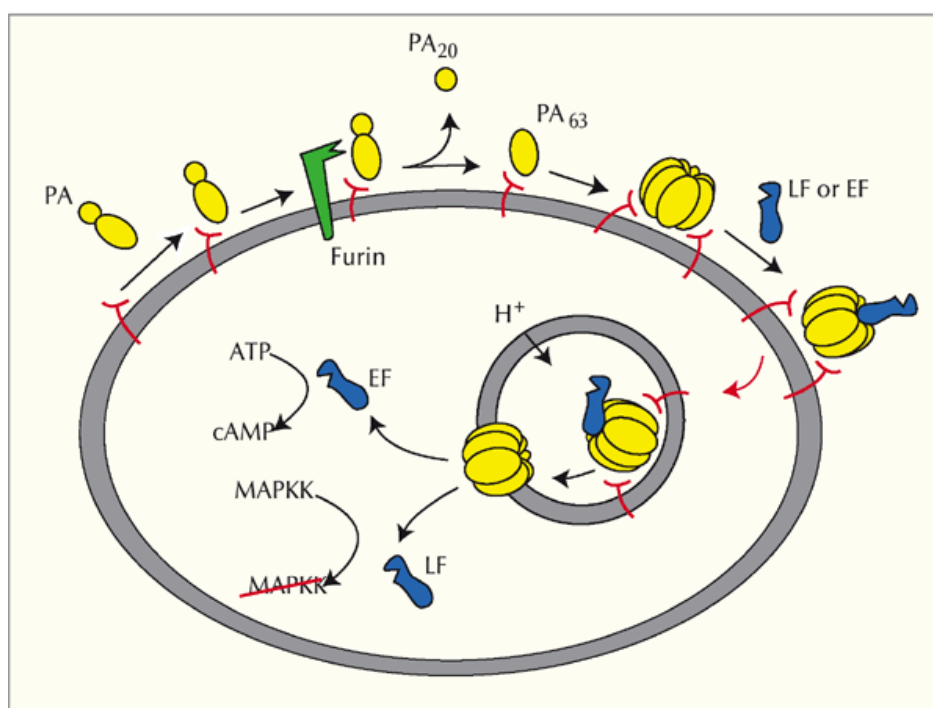
Figure 1. Mechanism of EF and LF introduction inside cell membrane via binding with PA (*3*).

Biochemical and computational research addressing different mechanisms of molecular recognition is currently being conducted to gain a better understanding of binding affinities and target specificity using synthetic alternatives. Peptide recognition elements have emerged as a potential synthetic alternative to antibodies. Antibody production against a specific protein often requires in vivo conditions and several months of isolation, whereas target-specific peptide binders can be sequenced and isolated in vitro within 2–4 days (*5*). The overall focus of our research is to develop a high-affinity peptide with the sequence necessary for PA binding that would provide low-cost, high-stability, rapid, and accurate detection methods for such virulent toxins as EdTx and LeTx.

My current project to this end goal centers around the use of enzyme-linked immunosorbent assay (ELISA) to determine the binding affinity of the 15 amino acid SM545 peptide, expressed in terms of the dissociation constant, K_D (units of nM). For the equilibrium dissociation reaction of a PA-peptide complex,

$$PA^{\bullet}Peptide \leftrightarrow PA + Peptide. \tag{1}$$

The K_D is determined via the following expression:

$$K_D = [PA]\,[Peptide]\,/\,[PA^{\bullet}Peptide\ complex]. \tag{2}$$

This paper focuses on ELISA and its biochemical uses in peptide-protein interaction and detection. Direct heterogeneous ELISA is a simple, rapid, and sensitive method that exploits the target-specific binding behavior of proteins. It employs the use of 96-well polystyrene plates (figure 1) in which reagents are sequentially added and directed at a solid phase, and several washing steps are performed to separate bound (reacted) and unbound (unreacted) reagents (*6*). Detection is based on the chromogenic or chemifluorescent interaction between an enzyme-linked protein and a reacting substrate that produces a readable signal. Because biological macromolecules, such as proteins, have the potential to denature and lose proper binding function, optimization of a consistent method is a key factor in obtaining reproducible results. Most of my current research has dealt with identifying these experimental complications and making the necessary modifications. Following successful K_D determination of the full-length SM545 peptide, we will analyze fragmented truncates of varying lengths to determine the exact sequence of the peptide necessary for PA binding.

2. Methods and Materials

2.1 Procedure for Direct Heterogeneous ELISA

The general procedure of the direct heterogeneous ELISA is outlined in figure 2 (*6*). The steps are as follows:

1. A 100-µL sample of peptide diluted in buffer is added to the solid phase, incubated for 2 h at room temperature (i), and allowed to passively adsorb to the well walls (ii) (*6–8*).

2. After incubation, the wells are emptied of the sample, and 300 µL of a blocking agent (neutral buffer + detergent) is added to the wells and incubated for 3 h. This blocking step is essential to coat all available binding sites on the solid phase to deter further passive adsorption by reaction reagents (*6, 9, 10*).

Figure 2. Procedural outlines for direct heterogeneous ELISA.

3. The wells are emptied again and flooded three times with 300-μL aliquots of the blocking agent. These washing steps remove any unbound (unreacted) peptide.

4. The antigen-labeled enzyme (100 μL) is then added to the reaction wells and incubated at room temperature for 1 h (iii).

5. Two additional washing steps are performed using a neutral buffer to remove residual detergent present in the wells from the blocking agent (6, 11). At this time, peptides are bound to the solid phase as well as to the enzyme-labeled antigen. Chromophoric or fluorophoric substrate (100 μL) (see section 2.2) is added to the wells and incubated for ~10–30 min (iv). A readable signal is observed at this stage. Enzymatic activity is stopped, and the colorimetric or chemifluorescent reaction discontinued via denaturation of enzymes (6). The reaction is quantified using a MicroWell plate reader (vii).

2.2   Reaction Reagents

The purpose of the following experiment was to investigate the binding affinity of the polystyrene-tagged SM545 peptide (molecular weight [MW]: 3515 g/mol) dissolved in a degassed 0.2-M carbonate/bicarbonate buffer with a pH = 9.4. PA mAb (MW: 150,000 g/mol) antibody dissolved in the same buffer was used as a positive control. The carbonate/bicarbonate buffer was chosen as a solvent because it contained no competing proteins and also served as a negative control to ensure that unreacted reagents were not present in the final quantified sample. Phosphate-buffered saline (PBS) +0.1% Tween-20 was used to block and wash the wells. The 0.5 µg/ml PA conjugated with horseradish peroxidase (HRP) was diluted in PBS and used as the enzyme-linked antigen. HRP reacts via oxidation with chromogenic substrates, such as 3, 3', 5, 5'- tetramentylbenzidine (TMB), or chemifluorescent substrates, such as 10-acetyl-3-7-dihydroxyphenoxazine (ADHP). A blue product is observed when the HRP-conjugated antigen reacts with TMB, while a resorufin, a fluorescent product, is observed when reacted with ADHP. The TMB reaction is stopped using a high concentration of a strong acid such as 0.5-M H_2SO_4 or 1-M H_2SO_4 in 8-M acetic acid, yielding a yellow end product with absorbance at 450 nm. The HRP-ADHP complex fluoresces at 570 nm.

2.3   Plate Setup and Sample Prep

The Nunc Immuno 96 Microwell plates were used for the solid phase. The plate was set up as shown in figure 3. The edge plates were left without samples to avoid temperature differences and edge effects (see section 2.4) (*6, 12*). The concentrations of the samples in the wells are given in table 1.
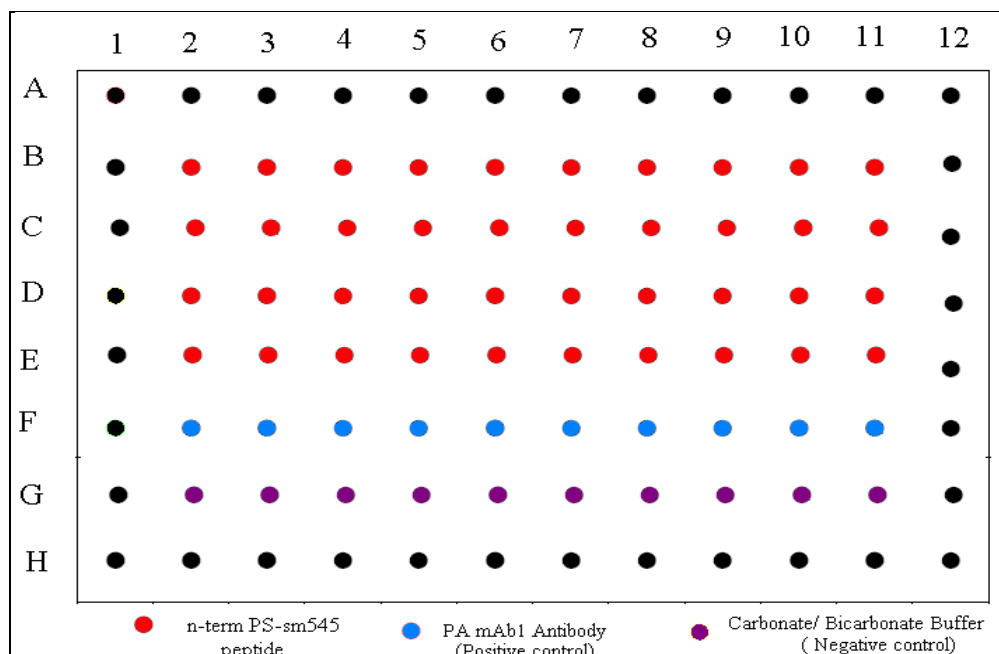
Figure 3. Pictorial representation of a 96-well plate setup.

Table 1. Antibody and peptide sample concentrations (µg/mL).

	1	2	3	4	5	6	7	8	9	10	11	12
A												
B		5.0 µg/ml	3.0	2.5	2.25	2.0	1.75	1.5	1.25	1.0	0.50	
C		5.0 µg/ml	3.0	2.5	2.25	2.0	1.75	1.5	1.25	1.0	0.50	
D		5.0 µg/ml	3.0	2.5	2.25	2.0	1.75	1.5	1.25	1.0	0.50	
E		5.0 µg/ml	3.0	2.5	2.25	2.0	1.75	1.5	1.25	1.0	0.50	
F		2.0 µg/ml	1.75	1.5	1.25	1.0	0.75	0.50	0.25	0.125	0.06	
G		0.2-M Carbonate/Bicarbonate Buffer										
H												

2.4   ELISA Complications and Modifications

In the ELISA method, the use of peptides and protein makes several factors important to successful and repeatable data collection and K_D determination. The first factor is amount. The same aliquot of liquid reagent needs to be delivered to all wells in each step of the procedure. To offset this factor, the same calibrated pipettes were used in all trials to maintain instrumental precision, and the delivery method was standardized across all wells in the plate to minimize human error. During all incubation steps, the reaction plates were placed on a rotator to ensure even distribution of reagents within the wells. With the constant and sequential emptying and flooding of the high-proximity wells with liquids, the possibility of cross contamination arises. Precautions, such as constant changing of pipette tips and removal of liquid via pipette withdraw instead of a simple overturn of reaction plate, were taken to ensure contaminations were minimized. Lastly, optimization of molecules, such as peptides and proteins (antigens and antibodies), is important to maintain working reactants. To counteract the potential of light and temperature-induced denaturation, aluminum foil was placed over the reaction plate during all incubation periods, and all peptide and protein samples were kept cold when not in use. Temperature differences across the well are also inherently present in the plates themselves. Peripheral wells have a higher evaporation rate than the interior well and therefore are cooler (*7*). For this reason the outer wells of the plate were not used, and evaporation rates were slowed down by sealing the plate and lid cover together with Parafilm during incubation steps.

3. Results

Several trials of the full-length SM545 peptide and the PA mAb antibody ELISA procedure were performed, and the degree of dissociation (K_D) was determined by plotting normalized fluorescence vs. molar concentration of peptide and antibody and fitted to a sigmoid function (figure 4). The molecular weight of the full-length polystyrene-tagged peptide is 3515 g/mol and that of the antibody is 150,000 g/mol. From this, the following molar concentrations of peptide and antibody can be calculated (table 2).
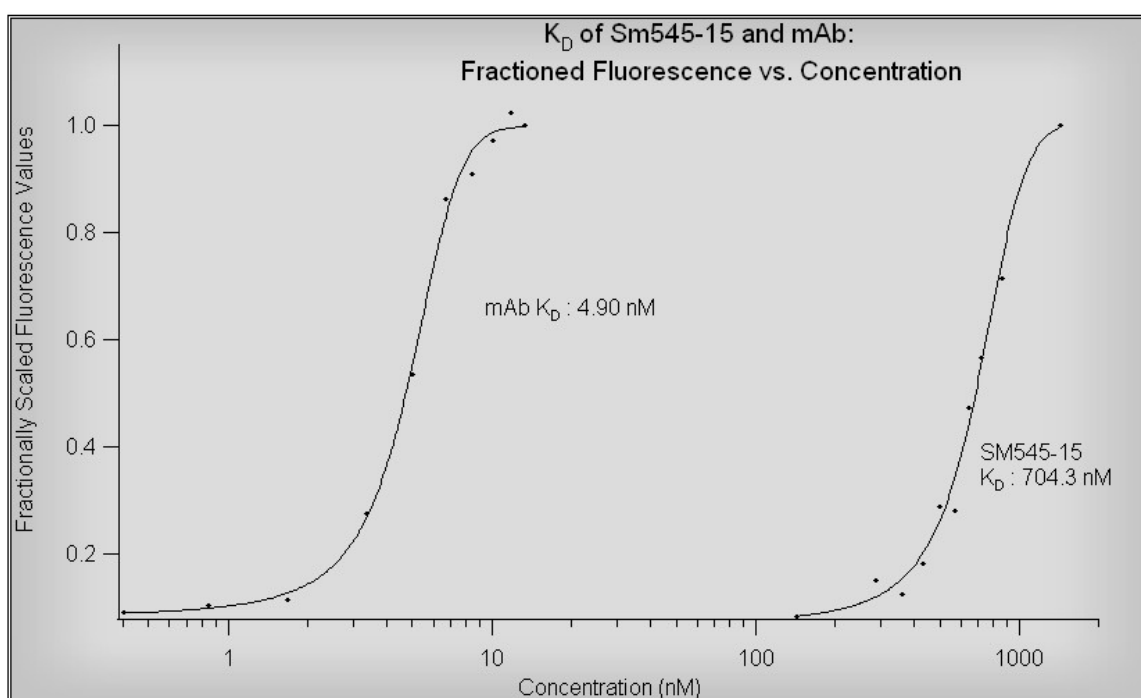
Figure 4. K_D determination curves of SM545-15 peptide and mAb using ADHP.

Peptide (rows B& C): MW= 3515g/mol		
Well number	Volume-based concentration	Molar concentration
2	5.00 µg/ml	1.42×10^{-6} M
3	3.00 µg/ml	8.53×10^{-7} M
4	2.50 µg/ml	7.11×10^{-7} M
5	2.25 µg/ml	6.40×10^{-7} M
6	2.00 µg/ml	5.69×10^{-7} M
7	1.75 µg/ml	4.98×10^{-7} M
8	1.50 µg/ml	4.27×10^{-7} M
9	1.25 µg/ml	3.56×10^{-7} M
10	1.00 µg/ml	2.84×10^{-7} M
11	0.50 µg/ml	1.42×10^{-7} M

Antibody (Row E) MW= 150,000g/mol		
Well number	Volume-based concentration	Molar concentration
2	2.00 µg/ml	1.33×10^{-8} M
3	1.75 µg/ml	1.17×10^{-8} M
4	1.50 µg/ml	1.00×10^{-8} M
5	1.25 µg/ml	8.33×10^{-9} M
6	1.00 µg/ml	6.67×10^{-9} M
7	0.75 µg/ml	5.00×10^{-9} M
8	0.50 µg/ml	3.33×10^{-9} M
9	0.25 µg/ml	1.67×10^{-9} M
10	0.125 µg/ml	8.33×10^{-10} M
11	0.060 µg/ml	4.00×10^{-10} M

Table 2. Converted molar concentrations of antibody and peptide samples.

From this data, we find that the K_D of the full-length SM545 peptide is 704.3 ± 24.7 nM ± while the mAb antibody has an equilibrium dissociation constant of 4.90 ± 0.14 nM. A follow-up to the full-length SM545 peptide was to analyze, using fluorescence, a 5-amino acid truncated segment of the SM545 peptide with molecular weight of 2338 g/mol (figure 5). The same volume-based peptide concentrations as presented in table 2 were used.
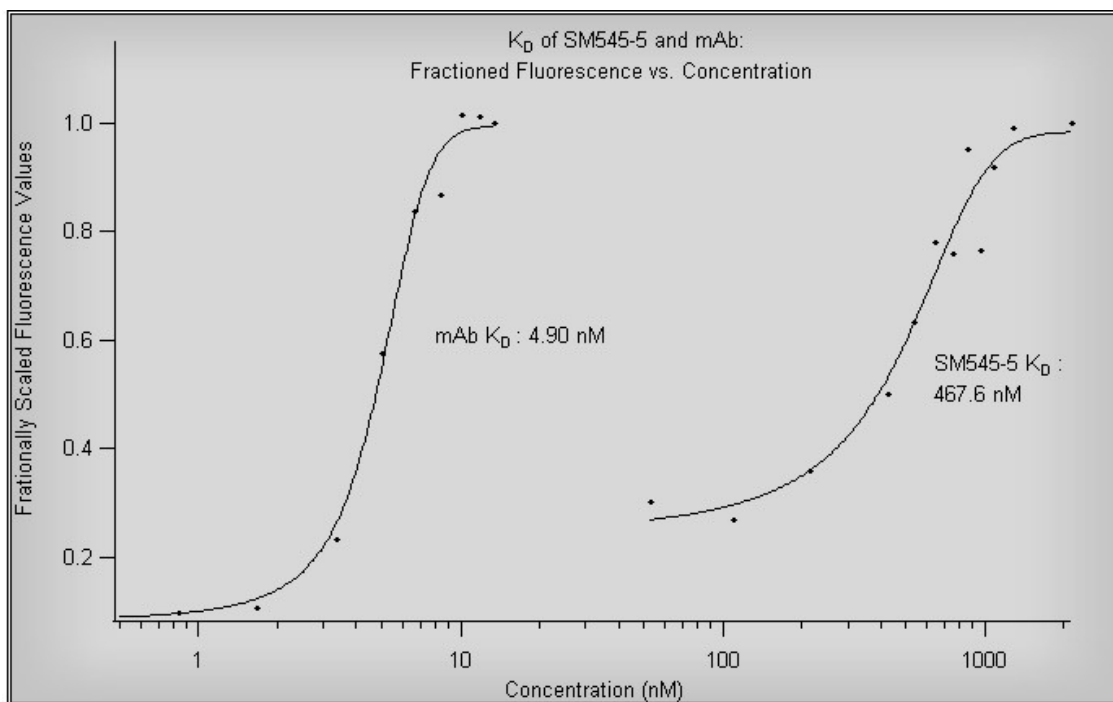
Figure 5. K_D determination curves of SM545-5 truncated peptide and mAb antibody using ADHP.

After eight trials, the K_D of the truncated peptide was determined to be 467.6 ± 178.0 nM. As shown in figure 4, the data does not fully fit a sigmoidal function. The lower limit of the peptide concentration will be extended in order to provide a more accurate determination of the truncated peptide's dissociation constant.

4. Summary and Conclusions

From these results, the full-length SM545 peptide binds with lower affinity to PA than the mAb. Preliminary results also suggest that although the SM545-5 truncate also binds with lower affinity to PA than mAb, it binds at a higher affinity than the full-length peptide. For this reason, experiments will continue using truncated peptide fragments of varying lengths of the peptide to determine the sequence with the highest binding affinity to PA. Although it is feasible to use TMB for signal detection, analysis of fluorescence of the truncated peptides using ADHP will be used exclusively as the detection method for remaining experimentation because it provides easily reproducible results.

5. References

1. Beauregard, K. E.; Collier, R. J.; Swanson, J. A. Proteolytic Activation of Receptor-Bound Anthrax Protective Antigen on Macrophages Promotes its Internalization. *Cellular Microbiology* **2000**, *2* (3), 251–258.

2. Elliott, J. L.; Mogridge, J.; Collier, J. R. Mapping the Lethal Factor and Edema Factor Binding Sites on Oligomeric Anthrax Protective Antigen. *Biochemistry* **2000**, *39* (22), 6706–6713.

3. Starnbach, M. N.; Collier, R. J. Anthrax Delivers a Lethal Blow to Host Immunity. *Nature Medicine* **2003**, *9*, 996.

4. Brossier, F.; Mock, M. Toxins of Bacillus Anthracis. *Toxicon* **2001**, *39* (11), 1747–1755.

5. Daugherty, P. S. Protein Engineering With Bacterial Display. *Current Opinion in Structural Biology* **2007**, *17*, 474–480.

6. Crowther, J. R. *The ELISA Guidebook*; Humana Press: Totowa, NJ, 2000; pp 10–111.

7. Esser, P. *Activity of Adsorbed Antibodies*; Thermo Fisher Scientific Application Note: 11b; http://www.nuncbrand.com/us/frame.aspx?ID=596 (accessed July 2010).

8. Esser, P. *Principles in Adsorption to Polystyrene*; Thermo Fisher Scientific Technical Bulletin: 06a; http://www.nuncbrand.com/us/frame.aspx?ID=579 (accessed July 2010).

9. Esser, P. *Blocking Agent and Detergent in ELISA*; Thermo Fisher Scientific Technical Bulletin: 09; http://www.nuncbrand.com/us/frame.aspx?ID=588 (accessed July 2010).

10. Pearce-Pratt, R.; Roser, B. *Comparison of Blocking Agents for ELISA*; Thermo Fisher Scientific Technical Bulletin: 07a; http://www.nuncbrand.com/frame.aspx?ID=155 (accessed July 2010).

11. Esser, P. *Detergent in Polystyrene ELISA*; Thermo Fisher Scientific Technical Bulletin: 08; http://www.nuncbrand.com/us/frame.aspx?ID=591 (accessed July 2010).

12. Esser, P. M. *Edge Effect in Thermo Scientific Nunc MicroWell ELISA*; Thermo Fisher Scientific Technical Bulletin: 01; http://www.nuncbrand.com/us/frame.aspx?ID=586 (accessed July 2010).

INTENTIONALLY LEFT BLANK.

Survivability/Lethality Analysis Directorate (SLAD)

INTENTIONALLY LEFT BLANK.

U.S. Army Research Laboratory

SUMMARY RESEARCH TECHNICAL REPORT

SUMMER RESEARCH TECHNICAL REPORT

Fragment Processing and Analysis for the Joint Trauma Analysis and Prevention of Injury in Combat (JTAPIC) Program

ANN M. PLOSKONKA AND MICHELLE C. RACINE
KAREN PIZZOLATO
BALLISTICS & NBC DIVISION
WARFIGHTER SURVIVABILITY BRANCH
ABERDEEN PROVING GROUND, MD 21005-5068

Contents

List of Figures

Abstract

The analysis of fragments removed from Soldiers killed in action (KIA) is vital to understanding the vulnerabilities to threats that they face in-theater, as well as for understanding enemy tactics, techniques, and procedures (TTPs). As part of the Joint Trauma Analysis and Prevention of Injury in Combat (JTAPIC) program, fragments of particular interest are removed during autopsy by the Office of the Armed Forces Medical Examiner (OAFME) and sent to the U.S. Army Research Laboratory's (ARL) Warfighter Survivability Branch (WSB) for analysis. The fragments are processed and analyzed, and these results are entered into the JTAPIC Fragment and Material Database. The processing and analysis data includes fragment photographs, dimensions, weight, density, three-dimensional scans, and elemental analysis results. The JTAPIC fragment analyses enable analysts to determine the identification of the fragment and determine the fragment's origin. This information is used in event recreations, modeling, and simulation. This paper focuses on all phases of the fragment analysis, including receipt of fragments and coordination with the Weapons and Materials Research Directorate (WMRD) for scanning and sterilization. Upon completion of WMRD's efforts, the students processed and analyzed all fragments and entered their results into the database.

Acknowledgments

I wish to acknowledge the mentorship of Karen Pizzolato and Barbara Wolfe.

INTENTIONALLY LEFT BLANK.

1. Introduction/Background

The Joint Trauma Analysis and Prevention of Injury in Combat (JTAPIC) program was established at the U.S. Army Medical Research and Material Command (USAMRMC), based on DODD 6025.25E (*1*). JTAPIC is a partnership whose purpose is to collect, integrate, and analyze operational and injury data. Its goal is to understand the vulnerabilities to threats that U.S. Soldiers face in-theater as well as enemy tactics, techniques, and procedures (TTPs). Fragment analysis is one project that was established as a part of the JTAPIC Program. During an event in-theater, fragments are often embedded in Soldiers. Fragments are removed during autopsy by the Office of the Armed Forces Medical Examiner (OAFME). Analysts within the Warfighter Survivability Brach (WSB) of the U.S. Army Research Laboratory (ARL) receive, process, and analyze fragments of interest. Fragments are analyzed to determine their elemental composition and origin. Knowing the composition of the fragments can assist with event recreation, modeling, and simulation, as well as provide insight into fragments still embedded in those wounded in the same event. All fragment information is stored in the JTAPIC Fragment and Material Database.

The JTAPIC Fragment and Material Database was created by WSB to collect and store the fragment information. The database provides an easily accessible storage method and search tool that can be used by all WSB analysts working on fragment-related projects. The database contains information including fragment photographs, dimensions, weight, density, three-dimensional (3-D) scans, and elemental analysis results.

The fragment processing and analysis procedures are described. Examples of the analysis results are included in this report. A total of 47 fragments from 8 cases were analyzed. These results were briefed to the Dismounted Soldier Incident Analysis Working Group and were provided to all JTAPIC partners.

2. Experiment/Calculations

JTAPIC fragment analysis is an ongoing project run by WSB analysts. OAFME transfers cases of interest to WSB for processing. A forensic investigator from OAFME transfers custody of each fragment delivery to a WSB evidence custodian. The fragments are then transported to Aberdeen Proving Ground (APG), MD. The WSB evidence custodian contacts all personnel involved in fragment analysis to develop an analysis schedule for each delivery. The following organizations are involved in the fragment analysis process: the Safety and Health Physics

Branch of the Associate Director for the Laboratory Operations Directorate (ALDO) and the Multi-Functional Materials Branch (MMB) of the ARL Weapons and Materials Research Directorate (WMRD).

Before WSB can handle the fragments received from OAFME, they must first be scanned for radiation, in particular, for the presence of depleted uranium. The fragments also must be sterilized to remove any potential biological hazard. The radiation scanning and sterilization is conducted at WMRD. The radiation scanning is conducting using a hand-held Geiger counter. Once the fragments have been confirmed to be free of radiation, photographs are taken of the fragments from each case. The chain of custody (COC) paperwork, DA Form 4173, is included in the photograph, so that the unique medical examiner (ME) identification number is visible as a reference within the photos. These photographs are vital as a precautionary measure to record the condition in which the fragments arrived at WMRD in case any of the fragments should be harmed during the sterilization process. The Fragment Evidence Logbook is used to record the date and time of evidence transfers. Notes on any distinctive features on the fragments and any ME information written on the fragment containers (such as recovery location) is also recorded in the logbook (*2*).

Once all information has been recorded in the logbook, the fragments can be sterilized. There are two separate sterilization procedures used by WMRD. Metallic fragments are sterilized using a VSR Model AS12 autoclave. The autoclave heats the fragments at 100 ºC for 100 min at 17 psi of pressure. Fragments that appear to be plastic are separated from the rest of the fragments during the photographing stage.   These fragments are soaked in formalin for 24 h, which provides the same level of sterilization as the autoclave method, but ensures that the plastic will not melt (*2*).

After sterilization is completed, the fragments are transported by the WSB evidence custodian for analysis. The fragments in each case are first placed into separate containers and the number of fragments for each case is noted in the database and logbook. Each fragment is examined individually. The weight of each fragment is taken using a Scout™ Pro SP402 scale, which has a maximum weight measurement of 400 g with a readability of ± 0.01 g. The length, width, and depth of each fragment are then measured using a 0–200 mm digital caliper. Observations of any distinguishing coloring, marks, or features of each fragment are made using a light microscope and are recorded in the database along with the weight and dimensions previously noted. The fragments are photographed again from all sides using an L-shaped forensic evidence ruler and grid paper to indicate the size of the fragment in the photograph. The ME number is written underneath the grid setup for reference. These photographs are cropped for uniformity and entered into the database under the ME identification number that corresponds to each specific fragment. These photographs are important because they preserve the image of the fragment, which could be used in a military court of law as evidence of a homicide (*2*).

Three-dimensional scans of the fragments are important for the same reason. Any fragment that has been removed directly from the body of a Soldier killed in action (KIA) is scanned using a NextEngine HD 3-D scanner. Scanning creates a replication of each fragment, which preserves its appearance and 3-D shape. Scanning must be completed prior to any required cutting for elemental analysis. The fragment is placed on the scanner in one orientation, is scanned, and then is rotated into an orthogonal position in relation to the first scan. Then, the fragment is scanned again. These two scans are then merged to create a complete 360° 3-D representation of the fragment using the Geomagic computer program. Any holes within the scans due to defects in the exact placement of the fragment or in the processing of the fragment by the scanner can be filled in using the Geomagic program. Once the model has been created, "snapshots" of the model are taken in Geomagic from various orientations of the model (top, bottom, left, right, front, back, and isometric). The final snapshot of each fragment, the file containing the scan itself, and the density of each fragment are entered into the fragment database (*2*).

The final part of the analysis involves the elemental analysis of each fragment by scanning electron microscopy-energy dispersive x-ray (SEM-EDS), which may be accompanied by inductively coupled plasma-atomic emission spectroscopy (ICP-AES) when necessary. A Hitachi S-4700 field emission SEM with energy dispersive x-ray spectroscopy (EDS) capabilities is used for fragment analysis. A low magnification (35×) micrograph is taken of a representative area on all samples. Qualitative elemental analysis is performed with EDS. With this technique the sample's surface is impacted by an electron beam. The electron beam excites the surface atoms in the sample producing x-rays that are characteristic of the elements found in the sample. A detector is used to convert the x-ray energies into voltage signals, which are sent to a pulse-processor for detection. The results are displayed as a spectrum of elements. When indicated, ICP-AES may be used to determine trace concentrations of metal and is used to provide quantitative elemental analysis of the fragments.

After the completion of all analyses, the cases are transported to Range 10 on Spesutie Island to be stored in a secure evidence cage. In the past two months, 47 fragments from 8 cases were delivered to WSB from OAFME and analyzed by us using the aforementioned procedure.

3. Results and Discussion

An example of the results from one of the 47 fragments processed from the past two deliveries is illustrated in figure 1. The physical characteristics of the fragment, including mass, dimensions, recovery location, and description, were taken and recorded in the database. Use of the light microscope revealed multiple tan fibers and a small blue fiber adhering to the surface of the fragment. The fragment was determined to be 1.33 g with dimensions of 13.93×14.42×3.01 mm. Figure 2 provides an example of the fragment photograph taken with a forensic evidence L-shaped ruler. The 3-D scan, illustrated in figure 3, preserved the image and shape of the

fragment and also provided the fragment density. Scanning indicated the density was 2.20 g/mL. The elemental composition of this fragment was determined to be predominately copper and iron, which can be seen in the SEM-EDS spectrum in figure 4. A magnified (35×) surface view of an area on the fragment is shown in the SEM micrograph (figure 5).

Mass: 1.33 g

Dimension: 13.93 × 14.42 × 3.01 mm

Density: 2.20 g/mL

Shape: Irregular

Recovery Location: Lateral thigh

Description: Silver colored with reddish-brown encrusted matter and ridges. One end is more jagged and irregular whereas other is more square with rounded edges. Many tan and reddish fibers on convex side along with a small blue fiber near a small hole (located near area where fragment folded onto itself). Near jagged end on reverse side are several tan fibers and fabric with spherical adhesions along concave side.

Predominant Materials: Copper and Iron

Figure 1. An example of the basic information entered into the database. The density, dimensions, mass, shape, recovery location, description, and predominant materials are shown for this fragment.

Figure 2. A photographs taken of the fragment once sterilization has been completed.

102
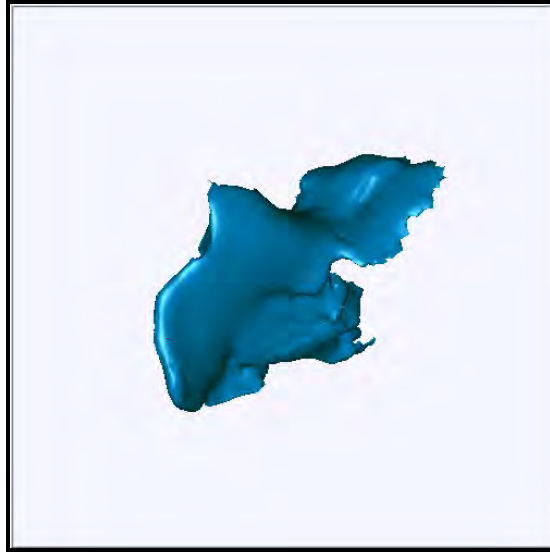
Figure 3. A 3-D model of the fragment obtained from
the scans and merged using Geomagic.
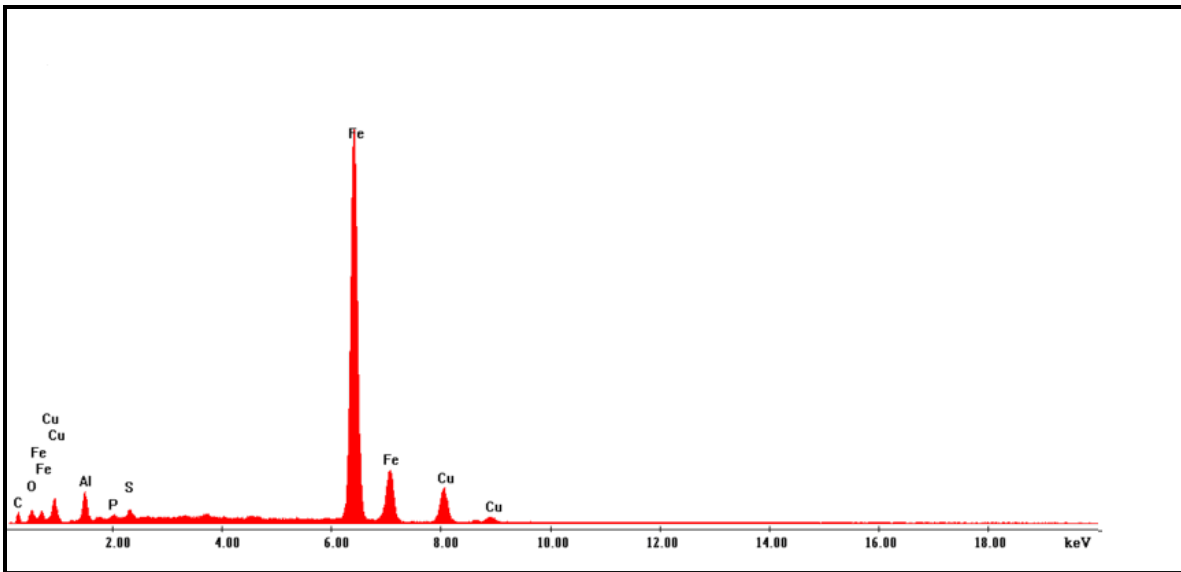
Figure 4. The EDS spectrum from the qualitative analysis of the fragment by SEM-EDS.
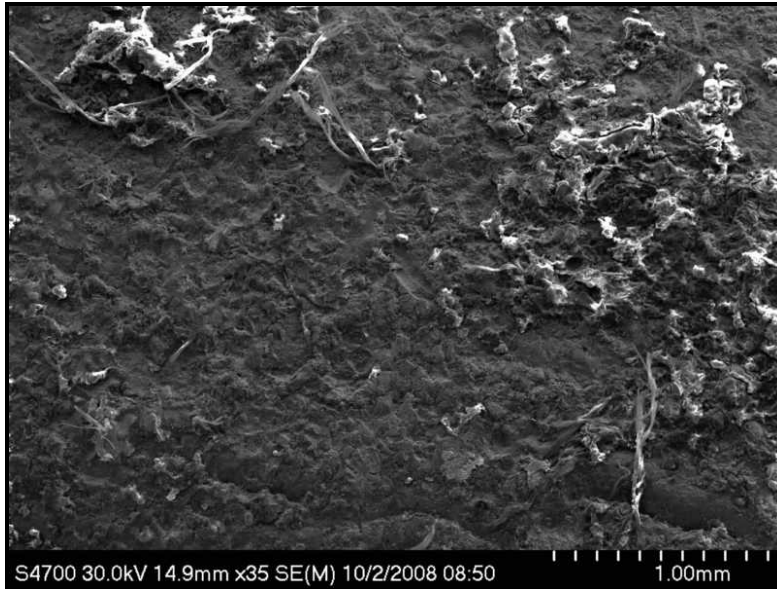
Figure 5. A micrograph of the fragment obtained by SEM.

4.   Summary and Conclusions

The elemental composition of the fragment described in section 3 was determined to be predominately copper and iron. These results were combined with event information to determine fragment origin. Fibers were found on the fragment.

The results of the analysis of these 47 fragments were provided to JTAPIC partners and were briefed to JTAPIC's Dismounted Soldier Incident Analysis Team (DIAT) to aid in their event analysis. The 3-D models and specific details of each fragment contained in the JTAPIC database will also be used in future modeling and simulation efforts and in event recreations. WSB analysts will also use the results to increase their understanding of enemy TTPs.

5. References

1. *Medical Research for Prevention, Mitigation, and Treatment of Blast Injuries*; U.S. Department of Defense Directive 6025.21E; U.S. Department of Defense, 5 July 2006.

2. Wolfe, B. *WSB Internal Operating Procedures for Processing of Fragments under JTAPIC*; August 2008.

INTENTIONALLY LEFT BLANK.

Vehicle Technology Directorate (VTD)

INTENTIONALLY LEFT BLANK.

U.S. Army Research Laboratory

Development of Multi-Body Dynamics Analysis Capability for Flapping Wing Systems

DAVID CROSS
DR. RAJNEESH SINGH
VEHICLES APPLIED RESEARCH DIVISION,
VEHICLES TECHNOLOGY DIRECTORATE,
ABERDEEN PROVING GROUND, MD

Contents

List of Figures

Abstract

MBDyn is an open source software tool capable of multi-body dynamics analysis. The Vehicles Technology Directorate (VTD) of the U.S. Army Research Laboratory (ARL) views MBDyn as a potential computational research and design tool for numerous aerial vehicle platforms. The most common application of MBDyn is for rotor-blade analysis, a subject of great interest to VTD. However, MBDyn provides a very generic environment for creating models and conducting dynamic analysis, making it suitable for numerous applications. One such application, also of interest to VTD, is research concerning flapping wing micro-aerial vehicles (FWMAVs). These systems are driven by the most advanced technologies and have great potential to aid the operational warfighter. The primary objective of this research is to build a preliminary model of a flapping wing system in MBDyn and evaluate it as a potential tool for future use at VTD. The preliminary models of flapping wing systems presented in this report illustrate that MBDyn possesses analysis capabilities well-suited to meet many VTD needs.

Acknowledgments

INTENTIONALLY LEFT BLANK.

1. Introduction/Background

Flapping wing micro-aerial vehicles (FWMAVs) are biologically inspired aircraft micro-systems with enormous potential for Army applications. The Vehicles Technology Directorate (VTD) of the U.S. Army Research Laboratory (ARL) in recent years has made the advancement of micro-systems technology one of their objectives. These systems would be extremely useful, discrete, and efficient surveillance platforms, which would enhance the warfighter's capabilities and safety while in operation. Furthermore, warfighter-focused micro-systems, especially FWMAVs, are driven by the most advanced, cutting-edge technologies, which bring about many design challenges, some of which are discussed in this report. The most obvious and critical design challenge for FWMAVs is also one of its greatest advantages: there are seemingly endless possibilities for FWMAV configurations.

The vast possibilities are easily illustrated by noting the immense variety of flapping wing configurations among insects, birds, and bats. Figures 1 through 4 help to illustrate the variety and complexity of wing topologies. Flapping wing flight is achieved by insects with masses on the order of milligrams and large birds with masses on the order of kilograms. Furthermore, research and observation has shown that all flapping wing species achieve flight through different patterns of wing kinematics and different wing topologies. There are a vast number of variables, all of which play some role in determining their wing shapes and wing kinematics. For example, house flies depend largely on forward flight as opposed to hovering; therefore, the wings of a house fly have a large degree of sweep, providing increased forward thrust. Dragonflies depend on forward flight as well, flying several miles a day, but also need the ability to hover; therefore, they have adapted to using four wings, or coupled wings, which provide thrust vectoring capabilities for forward flight, hovering, and even gliding. Hummingbirds are best known for their figure-of-eight wing kinematics with very high wing beat frequencies. This design provides them with enhanced maneuverability and agility. Most other birds have wing kinematics with a much more limited range of motion, and typically have the lowest wing beat frequencies amongst flapping wing species. Another reason for the immense variety is that the aerodynamic effects change drastically over a broad range of low Reynolds' numbers. Thousands of years of natural selection have fine-tuned these variables, endowing each particular species with the flight capabilities necessary for survival. For successful development of FWMAV technology, the ultimate goal is to understand the sensitivities that various flight objectives have toward all of these variables.

Figure 1. Dragonfly (*1*).
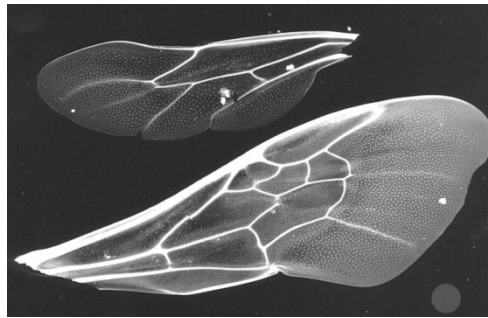
Figure 2. Wing topology (*2*).
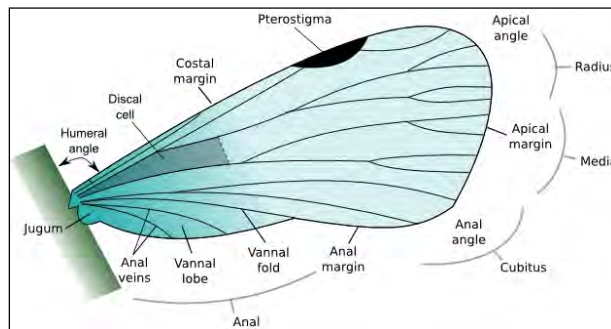
Figure 3. Wing nomenclature (*3*).
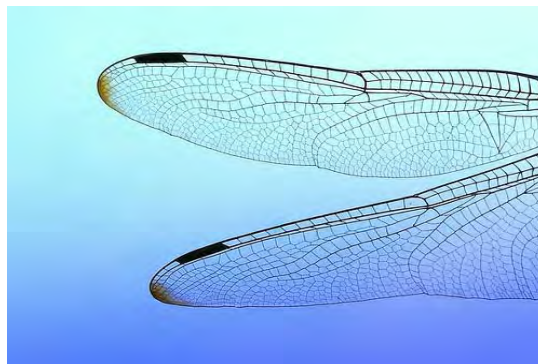
Figure 4. Dragonfly wing venation (*4*).

At the prime of the aviation industry, engineers and inventors approaching the problem of flight were faced with similar challenges. In order to design a successful aircraft system, they needed to understand the numerous physical relationships in play. After a century's worth of knowledge and experience, these relationships for conventional aircraft systems are somewhat trivial and the design process has been drastically simplified to a fundamental science. With interest growing in unconventional aircraft systems, such as FWMAVs, all of the previous knowledge and experience cannot be directly applied. Though it can be very helpful, the result is, once again, we face a very complicated and uncharted design process.

Experimental studies will be very important to designing successful flapping wing (FW) platforms, but computational studies will be crucial for optimization. Computational analysis of FW flight depends heavily on dynamics and aeroelastic effects. For these systems, optimization does not come in the form of mass minimization and stress constraints, like it does for conventional aircraft systems,, rather, optimization of FWMAVs depends on aeroelastic tailoring of the wing topology to optimize certain flight parameters, such as cruise efficiency or hover capability. The optimization can be constrained by controllability metrics, manufacturing constraints, etc. Therefore, it is imperative that an efficient and capable computational design tool be identified. The primary objective of this research is to evaluate a computational design tool called MBDyn. This multi-body dynamics tool has the potential to be used for detailed design of FWMAVs and other aerial vehicle platforms across the board. Currently, there are several documented applications of rotor blade analysis in MBDyn, all of which speak well for MBDyn's capabilities. However, there is no documentation of MBDyn being used to model FW systems. Therefore, this research evaluates the efficiencies and inefficiencies of MBDyn through a few simple FW models.

2.   Model Definition

VTD is developing experimental models of several micro-system platforms it is researching. Dr. Asha Hall of the Multifunctional Structures team in the Mechanics Division has built an experimental FW model that makes use of piezoelectric (lead zirconate titanate [PZT]) actuation. Hall's model is used as the baseline for developing a FW model in MBDyn. The following sections describe both the experimental model and the computational model, while also detailing MBDyn.

2.1   Experimental Flapping Wing Model

PZTs are often used for vibration damping on a variety of rotor-craft platforms and in many other applications as well. In this case, PZT is being used for the exact opposite reason, to excite motion in the system. The PZT in this case, is a thin cantilevered beam and can be seen clamped in the orange vice in figure 5. One end of the beam is clamped and connected to a power source.

The beam has three layers of material, and as voltage is applied, the top and bottom layer act as opposite poles, while the middle layer is a conductive passageway for electron transfer. The polarity between the two beams creates a strain, causing the PZT to deflect. If the poles are reversed, the direction of the strain reverses, thus deflecting the beam in the opposite direction. Therefore, the end of the beam can be forced to oscillate up and down at a desired frequency. The particular model that Hall has built has two wings rooted at the oscillatory end of the PZT. Thus, the up and down oscillation of the PZT excites a flapping motion in the wings. This is becoming a very popular method of actuation for FW systems due to its high frequency response and the ability to map periodic oscillations into desired wing kinematics (*5, 6*).
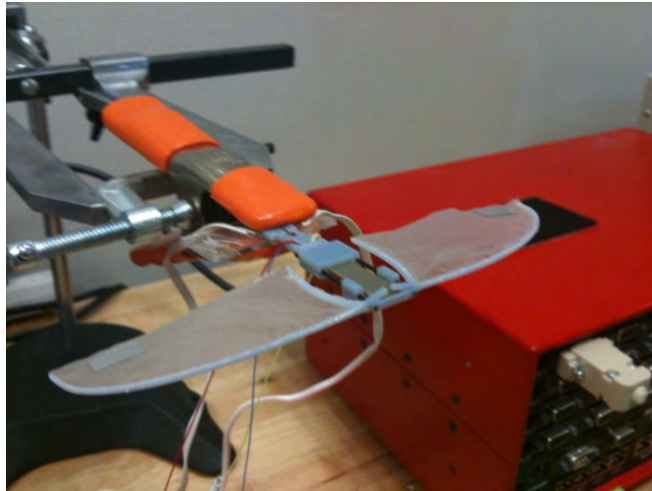
Figure 5. MRI experimental FW model (*5*).

Hall created the wing structure using a three-dimensional (3-D) printing method. The structure was modeled in computer-aided design (CAD) software, in this case, SolidWorks. The CAD model was then provided to the 3-D printer, in which a FullCure cartridge was installed. FullCure was the material used to create the structure and it is commonly used for 3-D printing. A couple hours later, Hall was able to remove her FullCure structure from the printer and begin conducting her experiments. The wing surface is a low density polyethylene (LDPE) film. In figure 5, note the gray patches near the wing tips. These are small pieces of reflective tape, which give Hall the ability to take displacement measurements while the wings are flapping (*5*).

Currently, the wings are connected via the two carbon fiber rods seen in figure 5. These rods are connected in such a way that they oscillate in unison with the PZT. The wing connection behaves like a clamped beam and does not allow rotation. The wings are flexible enough that if excited at the right frequency they will take on a flapping motion. Future models that MRI builds will look towards creating a mechanical connection that allows rotation. This will allow the flapping motion to achieve larger amplitudes than the current model. In addition, the current model only gives Hall active control of wing plunge. Many research studies have shown that the phase difference between wing plunge and wing pitch is key to optimizing thrust production.

Therefore, MRI is in the process of designing a modified PZT bimorph that will give them active control of both wing plunge and wing pitch. This will allow MRI to experimentally explore a broader range of wing kinematics (*5*).

2.2   MBDYN Input

MBDyn runs off of a text input file that requires specific formatting. The input file is divided into five different data sets. This section briefly defines those data sets and the basic layout for MBDyn input. A partial example of an MBDyn input file is provided in appendix A. Section 2.3 provides the detail of how the FW model specific to this research was defined in MBDyn. The five data sets are problem type, problem, control data, nodes, and elements. (*7*)

The first data set simply tells MBDyn what type of problem it will be solving. The analysis used for the FW model was an initial value problem; therefore, the second data set, specific to the problem type, is called initial value. This data set requires the definition of several parameters and allows for the optional definition of several others. The required parameters are initial time, final time, time step, max iterations, and tolerance. The initial and final time simply define the time domain within which the analysis is conducted. The time step is the increment size by which the time domain is discretized. Max iterations limits the convergence of the solution at each time step to a maximum number of iterations. Tolerance is the absolute error that must be achieved at each time step. (*7*)

The third data set is called control data. This set informs MBDyn of what is included in the model definition. That is, what type and how many nodes and elements are used in the model. This prepares MBDyn for what to look for and read and may not be required in future versions of MBDyn, but it certainly helps for readability and debugging purposes. MBDyn's definition of node and element covers many types of nodes and elements. For instance, a node can be structural, abstract, hydraulic, etc., and an element is considered to be a beam, a joint, a rigid body, a force, etc. (*7*)

The fourth data set is called nodes. All MBDyn nodes used in the model are defined in this data set. For the FW model, all nodes are defined as structural nodes; however, there are a few different types of structural nodes, most notably, static and dynamic. Basically, a dynamic node can be issued mass whereas a static node cannot. In the FW model, there is one static node at the wing root, necessary to ground the entire structure, while all other nodes are dynamic. The definition of a node requires the following information: node type, node ID, absolute position, absolute orientation, absolute velocity, and absolute angular velocity. Here the word "absolute" refers to the global reference frame or the absolute reference frame. (*7*)

The fifth data set is called elements. All MBDyn elements used in the model are defined in this data set. For the FW model, there were four different types of elements used: joints, rigid bodies, beams, and forces. MBDyn has a joint library, which allows one to define everything from a clamp joint to a pin joint to a revolute hinge to a gimbal hinge. This library is diverse

enough that almost any imaginable mechanical connection can be modeled. This versatility will be important for future development of FW models with complicated actuation and wing kinematics. This particular FW model makes use of a clamp joint, connecting the wing root to the leading edge spar, and a total joint. The total joint provides the ability to constrain or drive any degrees of freedom of the relative node. A drive can be defined as any time-dependent function and prescribed to a specific degree of freedom of any node. The drive used to prescribe motion in the FW model is described in section 2.3. Rigid body definition gives the structure mass and inertial properties. Any number of rigid bodies can be defined, and their definition consists of a rigid body ID, the node ID relative to which the rigid body is being defined, the total mass of the rigid body, a position vector defining the center of mass of the rigid body, and a mass moment of inertia matrix for the rigid body. This gives users versatility in the type of rigid body they wish to model. Beams are an element type that defines nodal connectivity. Beam2 is a beam connecting two nodes, while beam3 is a beam connecting three nodes. The Beam2 definition requires a beam ID; the two node IDs which the beam is connecting, a relative orientation matrix, which allows the beam to be defined in a local reference frame; and a constitutive law by which the beam behaves. (*7*)

2.3 MBDYN Flapping Wing Model

The first couple of weeks of this research time were spent climbing the initial learning curve of MBDyn. Very simple cantilever models were built and analyzed in MBDyn, and the research slowly progressed to the point of modeling a FW system. In the end, a rather refined process was developed to build a FW model for analysis in MBDyn.

The process begins by creating a two-dimensional unstructured surface mesh of triangular elements using a program called Solid Mesh. For the baseline model (MRI's experimental model), the unstructured mesh was created by mapping it over the SolidWorks file that Hall used for printing the FullCure structure. This ensured that the dimensions of the wing boundaries for the computational model matched those of the experimental model. Figures 6 and 7 show the SolidWorks model of the FullCure structure and the resulting unstructured mesh.

Figure 6. Image of the SolidWorks wing model (*5*).

120
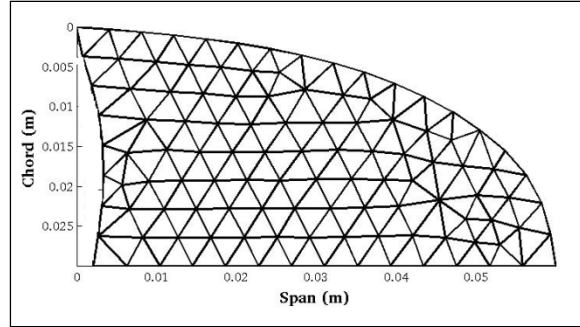
Figure 7. Unstructured mesh for the MBDyn model construction.

From here, the user employs a pool of MATLAB scripts that were developed throughout this research. The first MATLAB script reads the Solid Mesh data file and stores the element data into the workspace. In addition to the element data, some user input is required. The user is prompted to provide the following information:

1. The Node ID number at which the hinge is to be located.

2. The number of material groups the user wishes to define.

3. Material properties for the default material group (prescribed to all structural members):

    a. Material group ID

    b. Elastic modulus

    c. Shear modulus

    d. Mass density

    e. Thicknesses of member cross sections

4. Properties 1–4 for each subsequent material group

5. The number of stiffening members the user wishes to define (spars/ribs).

6. For each stiffening member, the user must enter the following:

    a. Material group ID used for the stiffening member

    b. Vector of nodal connectivity for the stiffening member

    c. Thicknesses of the member cross section at first node

    d. Thicknesses of the member cross section at last node

The material property for this particular FW model is the polyethylene material group. These material properties are prescribed to all structural members. The material properties list in item 4 are used to define the FullCure. There are two stiffening members defined in this FW model:

121

one is the leading edge FullCure spar and the other is the root edge FullCure rib. A linear interpolation is applied to the thicknesses defined in item 6, allowing the leading edge spar and root edge to be properly tapered.

A second MATLAB script takes the user input and element data and writes all of the information to an MBDyn input file with proper formatting. The MATLAB script then calls and executes MBDyn. If MBDyn has an error, it prints the error to the MATLAB command window, and if it is successful, another MATLAB script reads the output files and stores the information into the MATLAB workspace. The MATLAB script has some optional post-processing features for graphs and visualization. In addition to the MATLAB visualization shown in figure 8, there is an application called EasyAnim, which is compatible with MBDyn. A snapshot of the EasyAnim window is provided in figure 9. EasyAnim allows for the user to create video files to visualize the structural dynamics for the entire time domain of the analysis. Before presenting the results of this model, it is important to discuss some modeling considerations.
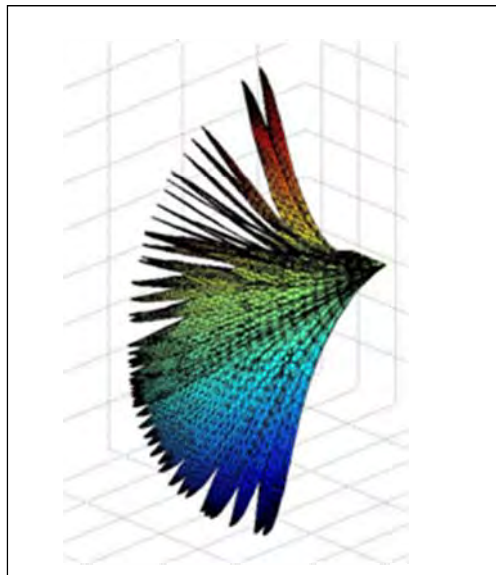
Figure 8. MATLAB visualization example.
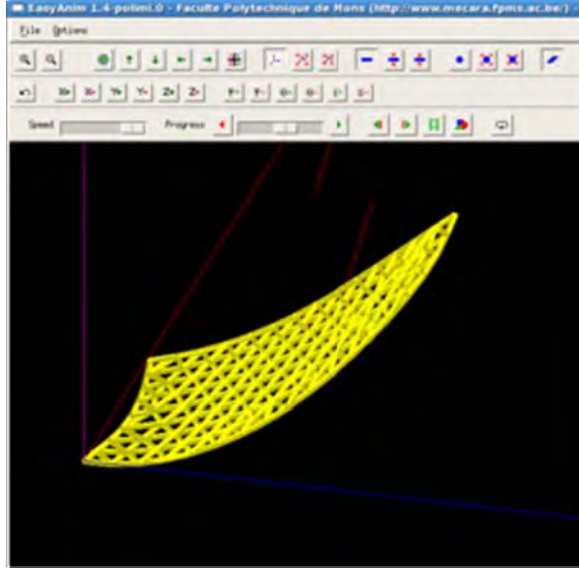
Figure 9. EasyAnim visualization snapshot.

2.4 Important Modeling Considerations

This section discusses important issues regarding beam analysis, equivalent continuum, rigid body definition, and wing excitation. All of these topics have considerable influence on the dynamic response of the system.

As seen in the figure 9, the wing surface is being modeled as a network of one-dimensional (1-D) beams. Before discussing the issue of equivalent continuum, it is important to understand how MBDyn is conducting the deformation analysis of 1-D beams. For the FW application, like many others, being able to accurately model large deformations and rotations is critical. It is here that many beam theories can lose accuracy. The beam theory being used by MBDyn is the geometrically exact beam theory (GEBT). GEBT is essentially the combination of a 1-D nonlinear beam analysis and a 2-D cross-sectional stiffness analysis. It relies on the constitutive law (equation 1); however, the constant matrix does not have to be diagonal and can include the proper coupling terms. In addition, variations of this law can be used that include warping and viscous effects (*8, 9*).

$$
\left\{ \begin{array}{c} F_1 \\ F_2 \\ F_3 \\ M_1 \\ M_2 \\ M_3 \end{array} \right\} = \left[\begin{array}{cccccc} EA & 0 & 0 & 0 & 0 & 0 \\ 0 & GA_{xx} & 0 & 0 & 0 & 0 \\ 0 & 0 & GA_{zz} & 0 & 0 & 0 \\ 0 & 0 & 0 & GJ & 0 & 0 \\ 0 & 0 & 0 & 0 & EI_{xx} & 0 \\ 0 & 0 & 0 & 0 & 0 & EI_{zz} \end{array} \right] \left\{ \begin{array}{c} \gamma_{11} \\ 2\gamma_{12} \\ 2\gamma_{13} \\ \kappa_1 \\ \kappa_2 \\ \kappa_3 \end{array} \right\}
$$

(1)

This law allows for direct computation of the strains. The strains are then simply integrated in order to calculate the displacements and rotations. For that reason, this type of beam analysis can capture large deformations while only relying on the assumption of small strains. The FW system is perfect for this, because flexible wings will respond with large rotations in the local reference frame but very small strains. Furthermore, the constitutive law contains the entire geometric definition of the beam, making no approximations, hence the name "geometrically exact (*8, 9*)."

For the purposes of this research, it would be ideal to represent the wing membrane with either 2-D shell elements or membrane elements. Unfortunately, as previously stated, MBDyn is limited to 1-D beams. So, it is important to consider how a beam/truss lattice continuum can be equated to a thin film/membrane continuum. Odegard and Gates (*10*) present an equivalent continuum method for representing a complicated volume with a finite element truss lattice. In their paper, Odegard and Gates define certain criteria, which if met, means the representative truss lattice can be assumed equivalent to the desired continuum. When the two models are prescribed, a discrete load under static analysis must satisfy the following:

- The boundary displacement of the representative element must match that of the other model.

- The thermo-elastic strain energies of the two models must be equivalent.

Odegard and Gates provide the following expression for calculating the strain energy of a discrete beam/truss lattice.

$$\Lambda^{t} = \sum_{j} \sum_{i} \frac{A_i^j Y_i^j}{2 R_i^j} \left(r_i^j - R_i^j \right)^2$$

(2)

Here, A is the cross-sectional area of the member, Y is Young's modulus of the member material, r is the deformed length of the member, and R is the un-deformed length of the member. The summation about j is from 1 to the number of types of members, if there are multiple types; and the summation about i is from 1 to the number of members (*10*).

The primary issue with applying this method to the model defined in this research is that the method depends upon periodicity of the representative lattice. Unfortunately, the unstructured mesh used to create this model does not have periodicity. Nevertheless, a lot can be said for the importance of equating the strain energies of two different models in order to consider them equivalent continua. The results presented in the research do not attempt to apply an equivalent continuum method to the model. Rather, this preliminary computational model uses the material properties of polyethylene while keeping the representative beam members thin in cross section. Equating the strain energy of the representative model to the polyethylene membrane should be applied in the future, and is further discussed in section 4 of this report (*10–12*).

Rigid body definition could be done in a number of different ways and still properly represent the network of 1-D beams; however, the simplest way is to define a rigid body for each beam. Thus, when each beam is identified with two nodes, the rigid body for that beam is defined relative to the first of the two nodes. The mass is defined by multiplying the mass density of the material for each beam by its respective length and cross-sectional area. The relative center of mass is defined as the distance vector from the relative node to the midpoint of the beam. Lastly, the mass moment of inertia matrix is defined as that of a simple rod or beam in the absolute reference frame (9).

The last key component of the model definition is prescribing the dynamic motion of the system. All nodes are initialized at rest, and the wing surface is defined in the x-y plane with zero pitch. As previously described, the current wing root connections force the wings to have the behavior of clamped boundary conditions. This dynamic motion is easily modeled in MBDyn through what is called a drive. A drive is a time-dependent function, usually periodic, which defines the motion of a given node. Consequently, in this FW model, the drive was defined as a sine function, which acted for the entire time domain. As previously mentioned, the current experimental model has wings that behave as clamped beams constraining rotation at the roots. Therefore, two of the models presented in section 3 excited a vertical oscillation of the wing root. In addition, section 3 also presents a model that was excited by prescribing a rotation at the root rather than a vertical oscillation.

3.   Results

This section details three very simple FW models. These models illustrate that MBDyn is capable of successfully modeling a simple FW system. Section 4 of this report sheds light on MBDyn's potential role for conducting computational studies to benefit and advance the efforts of detailed design of FWMAV platforms. No comparison of the computational results to the experimental results is made here. Some refinement needs to be done before the computational model can be directly compared to the experimental model. Right now, the wing root excitation of the computational model is of arbitrary amplitude. This is because displacement measurements of the PZT have not been directly taken. Thus, the dynamic motion prescribed in the computational model cannot yet be equated to that of the experimental model. Nonetheless, the results presented illustrate MBDyn's capability to model FW systems.

3.1   Model 1

The first model is built upon the coarse, unstructured mesh shown in figure 10. This mesh was mapped directly from the SolidWorks model used to print the FullCure structure of the experimental model.
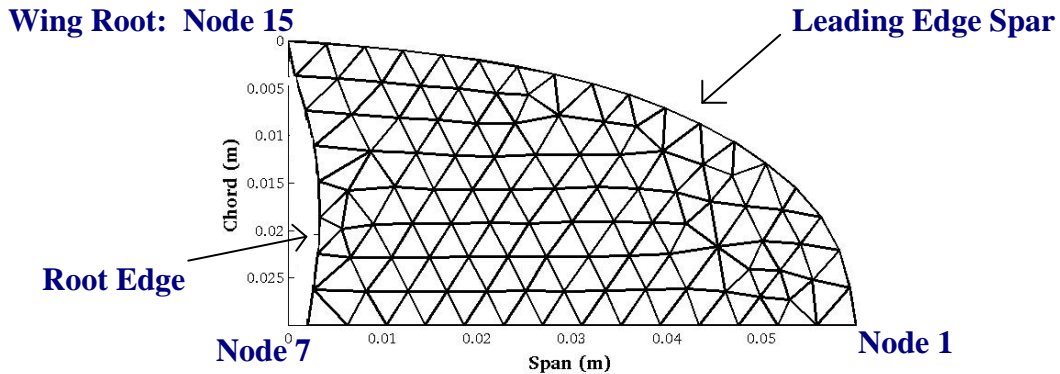
Figure 10. Coarse, unstructured mesh.

The following are the specifications for the model:
- Membrane material:

  Elastic modulus: 150 MPa

  Shear modulus: 150 MPa

  Mass density: 1030 kg/m^3

  Cross section: 1 mm x 1 mm

- FullCure material:

  Elastic modulus: 700 MPa

  Shear modulus: 700 MPa

  Mass density: 1092 kg/m^3

- Leading edge spar:

  Material: FullCure

  Cross section at node 15:   1.29 mm x 1.26 mm

  Cross section at node 1:   1 mm x 0.52 mm

- Root Edge:

  Material: FullCure

  Cross section at node 7:   1 mm x 0.66 mm

  Cross section at node 15:   1.29 mm x 1.26 mm

Before exciting the structure and conducting a dynamic analysis, it is important to conduct an eigenvalue analysis of the structure. Every structure has various natural frequencies. When a

structure is excited at one of its natural frequencies it will respond according to the corresponding mode shape. In this particular case, a flapping motion is desired, and twist about the span-wise axis is not desired. After conducting an eigenvalue analysis of this structure, another capability of MBDyn, the mode shapes shown in figure 11 resulted.

| 19.8 Hz | 71.3 Hz | 72.2 Hz | 111.7 Hz | 185.7 Hz |
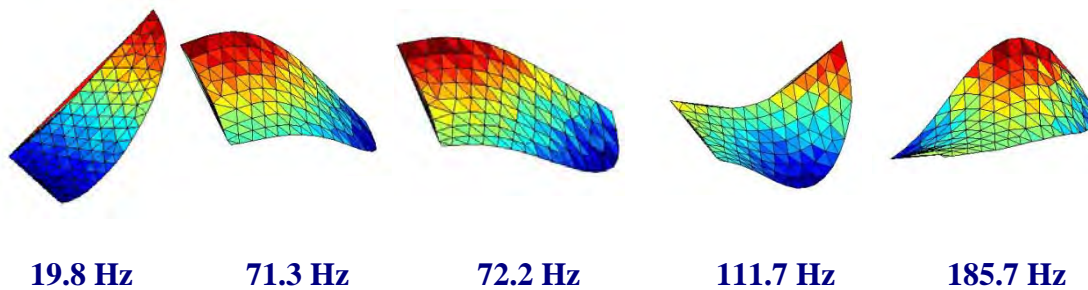
Figure 11. Model 1 mode shapes.

The lowest frequency results in the lowest degree of curvature with little twist. The higher frequencies exhibit motion that has either too much twist or too much curvature, neither of which is desired. Therefore, when conducting this dynamic analysis, the excitation should be at the first frequency.

Figures 12 through 15 illustrate the structural response of the wing due to an excitation at a frequency of 19.8 Hz. The excitation was prescribed at the wing root in the vertical z-direction with an amplitude of 1 mm. Notice that the wing tip displacement peaks at 10 mm. Because the excitation was at a natural frequency, the response is amplified as the excitation continues, inducing a flapping motion in the wing. It should also be noted that this model has zero damping, which will be necessary for future models. In addition, a beat frequency is apparent, which is the result of the interaction between multiple frequencies. This is less than desirable, and will have to be explored in future models.
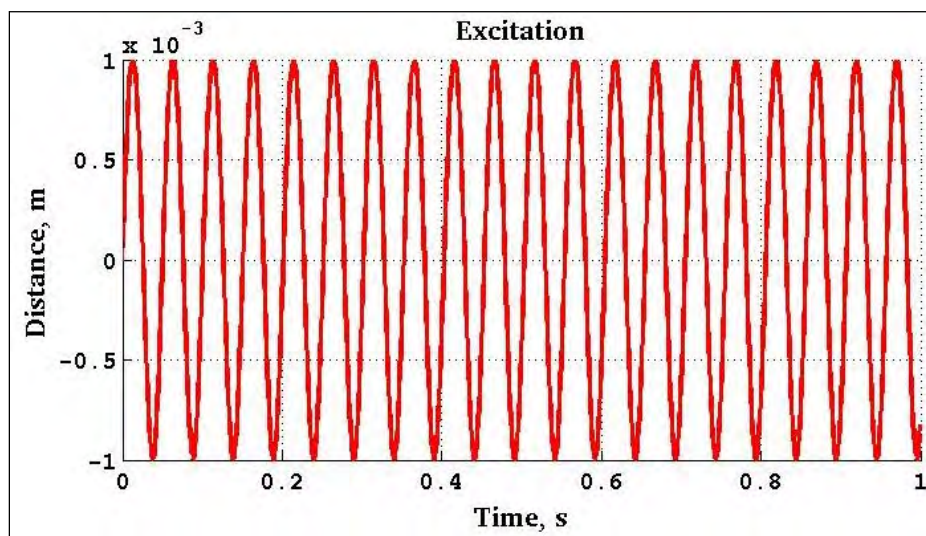
Figure 12. Model 1 excitation, amplitude = 1 mm, frequency = 19.8 Hz.

127
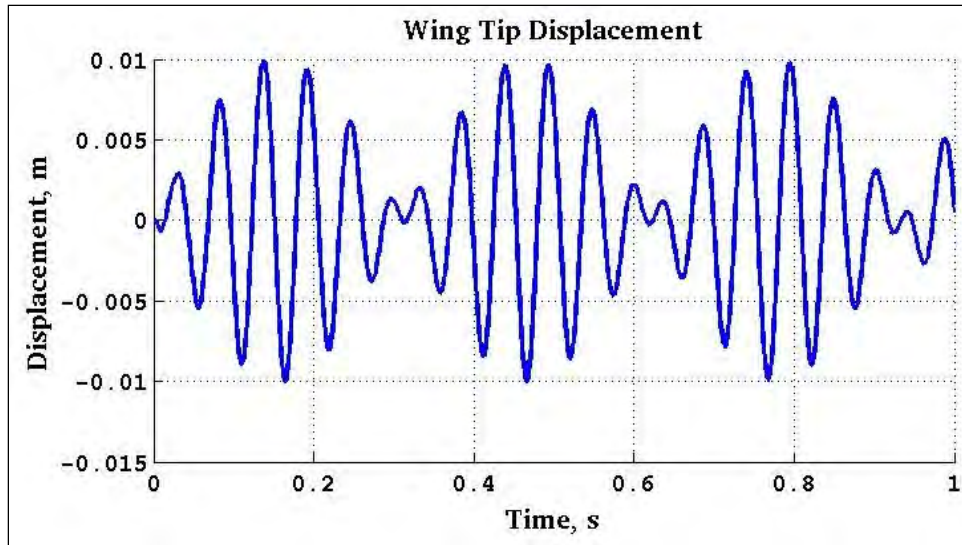
Figure 13. Model 1 wing tip displacement.
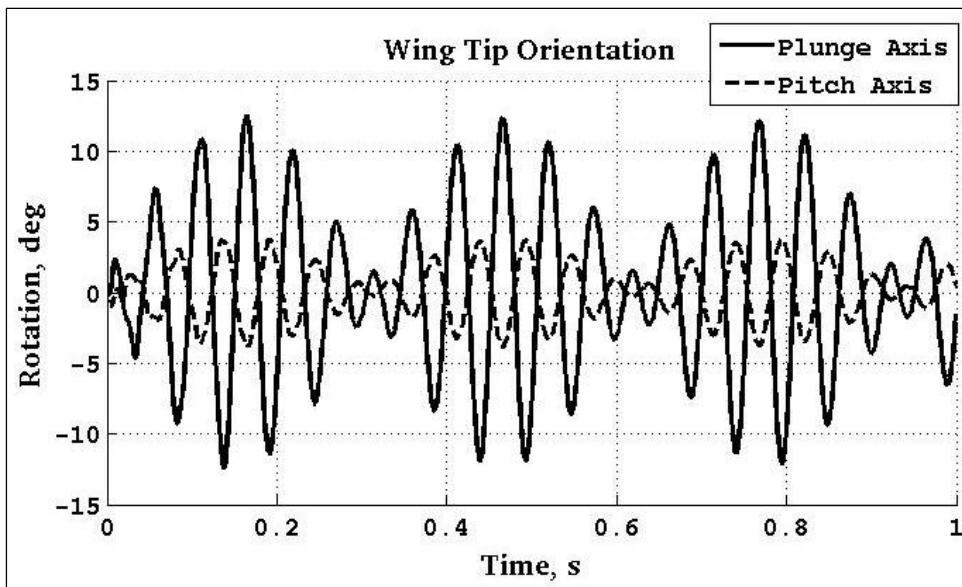
Figure 14. Model 1 wing tip rotations.
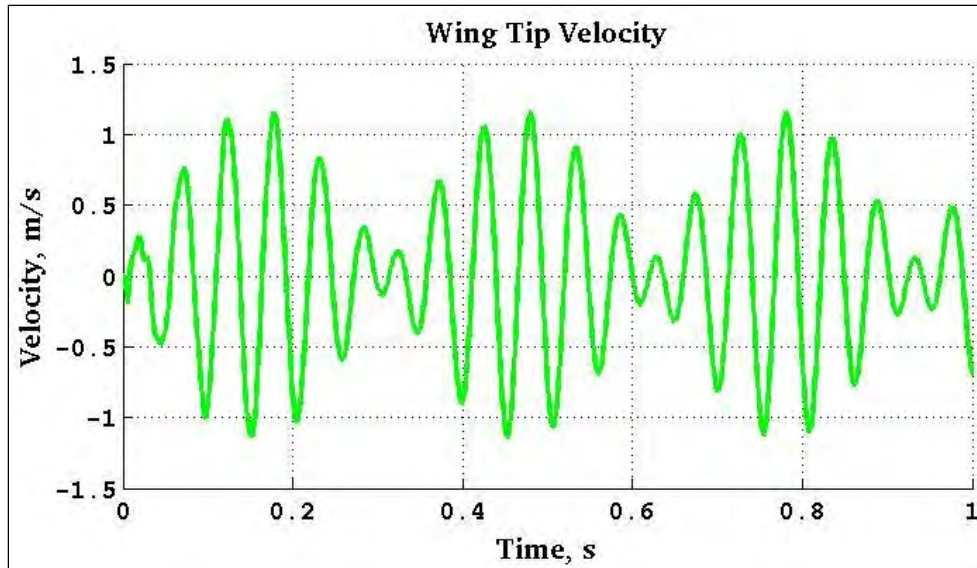
Figure 15. Model 1 wing tip velocity.

3.2   Model 2

The second model is built upon the fine, unstructured mesh shown in figure 16. This mesh was also mapped directly from the SolidWorks model, but given a smaller element spacing.

Wing Root: Node 15
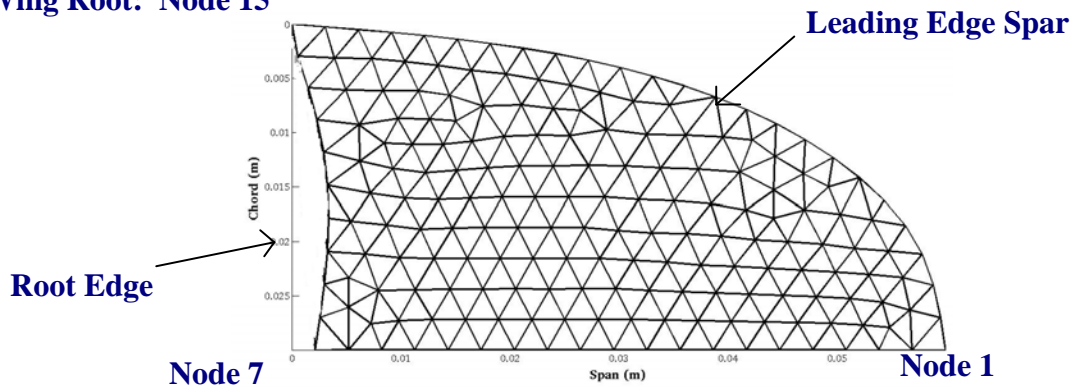
Figure 16. Fine, unstructured mesh.

The following are the specifications for the model:

- Membrane material:

  Elastic modulus: 150 MPa

  Shear modulus: 150 MPa

  Mass density: 1030 kg/m^3

  Cross section: 1 mm x 1 mm

129

- FullCure material:

  Elastic modulus: 700 MPa

  Shear modulus: 700 MPa

  Mass density: 1092 kg/m^3

- Leading edge spar:

  Material: FullCure

  Node connectivity: [15,31:53,1]

  Cross section at node 15:   1.29 mm x 1.26 mm

  Cross section at node 1:   1 mm x 0.52 mm

- Root Edge:

  Material: FullCure

  Node connectivity: [7,22:30,15]

  Cross section at node 7:   1 mm x 0.66 mm

  Cross section at node 15:   1.29 mm x 1.26 mm

The eigenvalue analysis was conducted the same as in Model 1; however, the results this time were less than desirable. As can be seen from the mode shape in figure 17, no natural frequency exists that produces the flapping motion desired. This model was tested at the lowest natural frequency but resulted in a motion involving little wing plunge and a lot of wing twist/pitch.

54.4 Hz

Figure 17. Model 2 mode shape.

This is a perfect illustration of how important equivalent continuum is for continuing research. Ultimately, an equivalent continuum method would allow for a particular system to be accurately modeled by different meshes. The finer mesh used in this model makes the wing much stiffer due to the larger number of beams. A stiffer structure results in higher natural frequencies, and in this case, the mode shapes result in motions that are not desired. Since an accurate equivalent

continuum method has yet to be developed, all that can be done is adjust the beam properties by way of trial and error until a similar frequency and mode shape is obtained. Upon doing so the membrane properties were adjusted to E = G = 132 Mpa, and new eigenvalues and mode shapes were found (figure 18).

| 18.5 Hz | 56.0 Hz | 65.4 Hz | 102.3 Hz | 172.8 Hz |
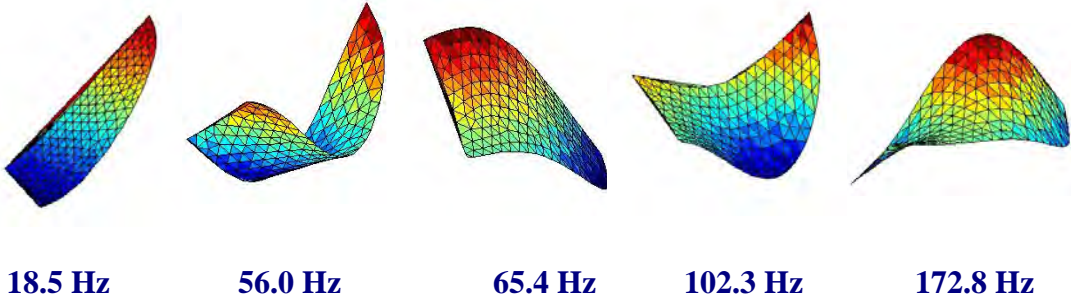
Figure 18. Model 2 mode shapes with adjusted membrane properties, E = G = 132 Mpa.

Now the structure has a natural frequency that corresponds to a mode shape very similar to that of Model 1. The structure was excited at 18.5 Hz with the same amplitude used in Model 1. The results are shown in figures 19 through 22. The motion exhibits the same behavior as Model 1, but notice that the maximum displacement of the wing tip has decreased to about 8.5 mm. For future models, it will be very critical to represent the membrane appropriately. Changing the mesh forced a change in the material properties to obtain similar results. These sensitivities will need to be explored in addition to formulating an adequate equivalent continuum method.
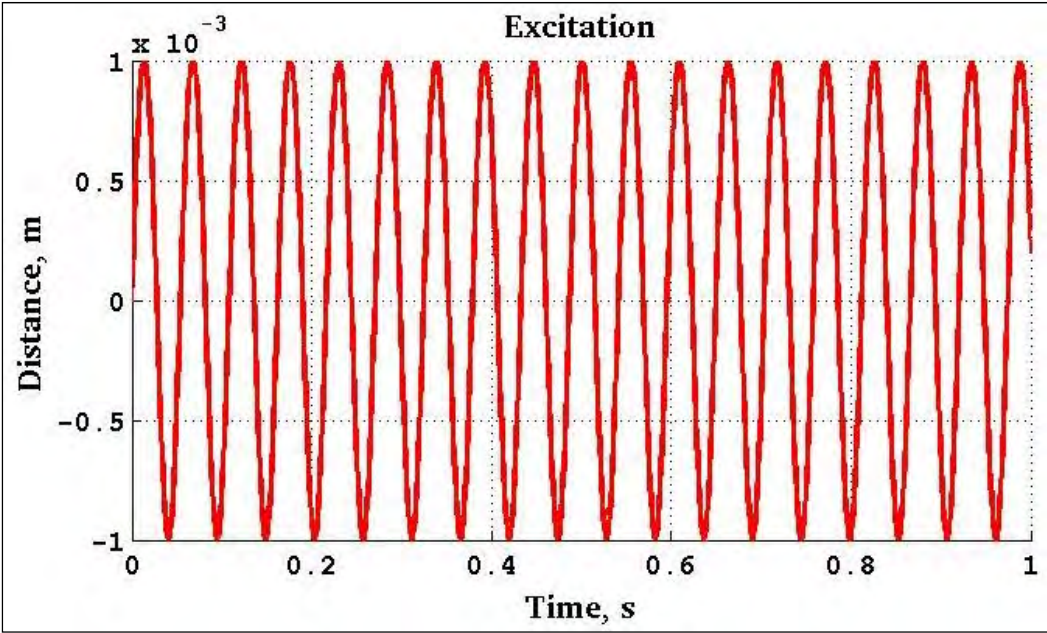
Figure 19. Model 2 excitation, amplitude = 1 mm, frequency = 18.5 Hz.
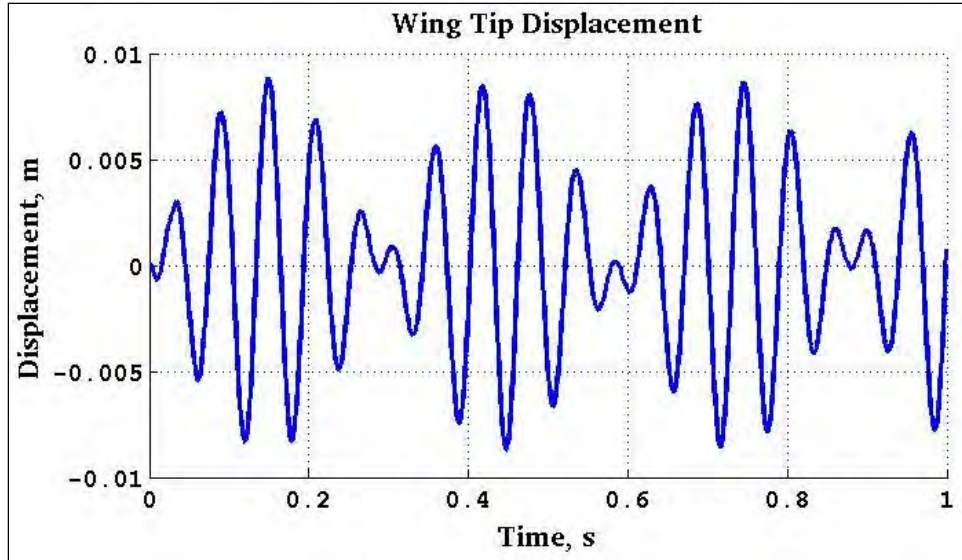
Figure 20. Model 2 wing tip displacement.
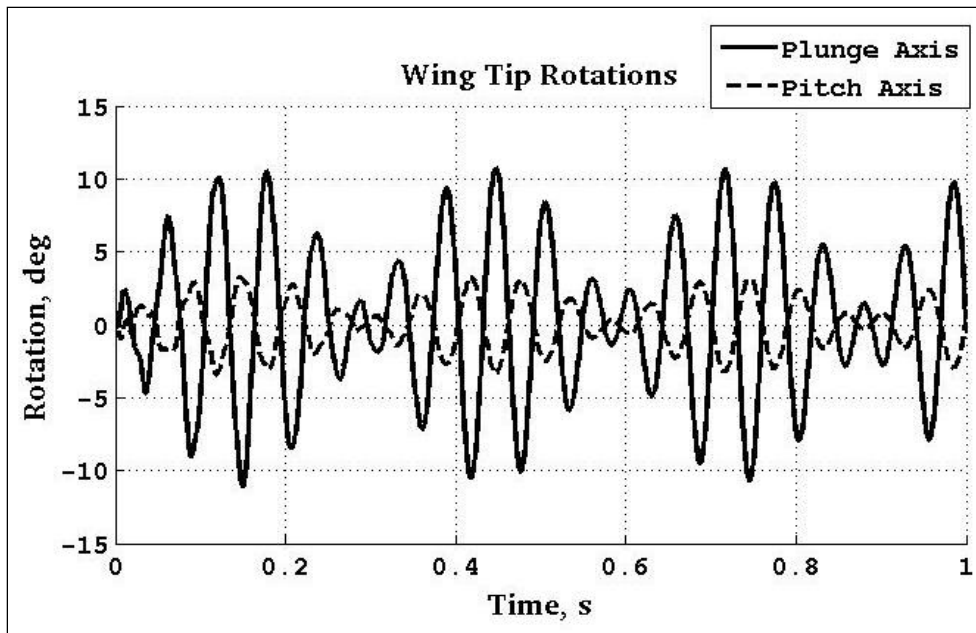
Figure 21. Model 2 wing tip rotations.

132
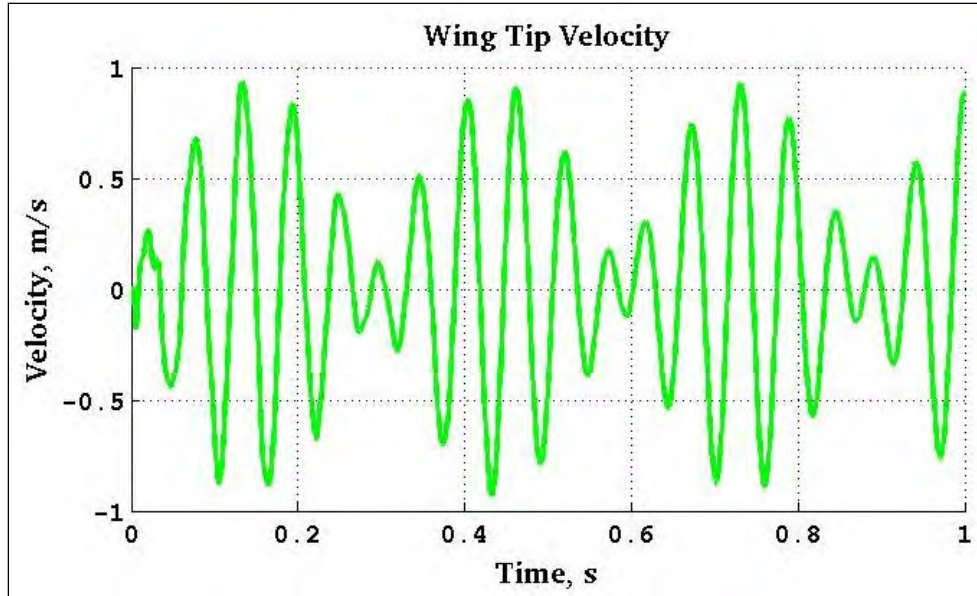
Figure 22. Model 2 wing tip velocity.

3.3   Model 3

The third model varies from the first two in that the motion prescribed at the wing root is a rotational motion as opposed to a vertical displacement. This excitation forces the orientation of the wing to change more drastically than that of the first two models. This model was built upon the coarse mesh used in Model 1 and has all of the same material properties. Because it was the same structure as Model 1, it has the same natural frequencies, and so, was excited at the same frequency of 19.8 Hz. The results are shown in figures 23 through 26. Because rotation was allowed, the wing tip displacement achieved a larger amplitude, exhibiting a more enhanced flapping motion.
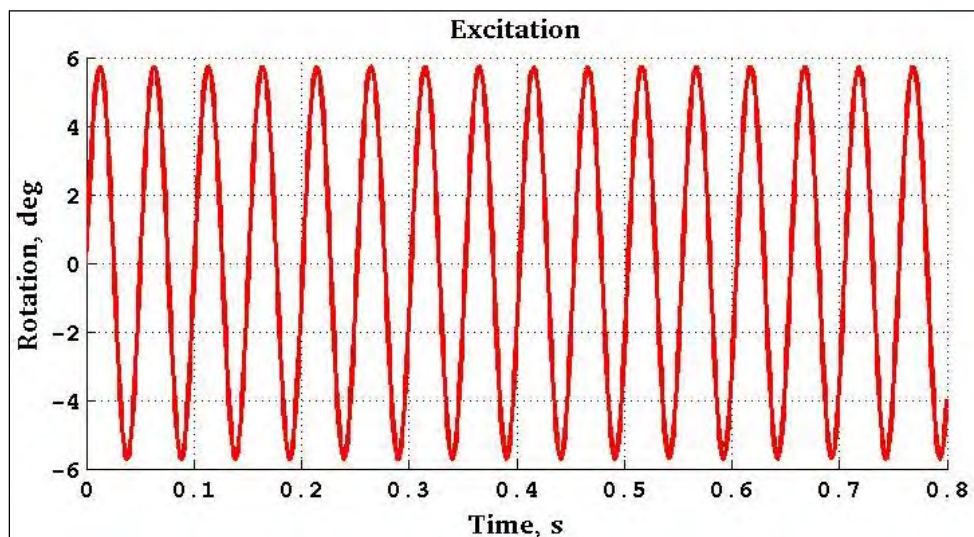
Figure 23. Model 3 excitation, amplitude = 0.1 radians, frequency = 19.8 Hz.

133
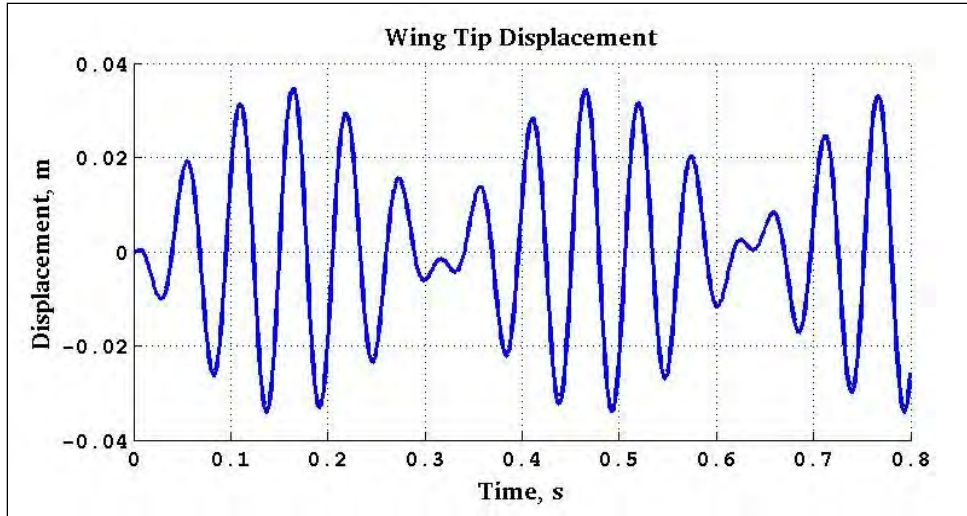
Figure 24. Model 3 wing tip displacement.
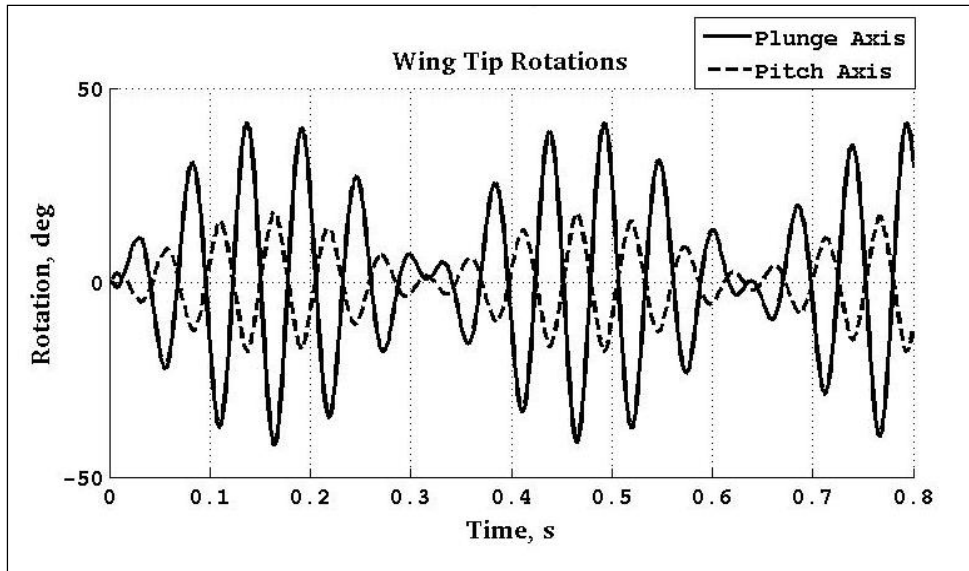
Figure 25. Model 3 wing tip rotations.

134
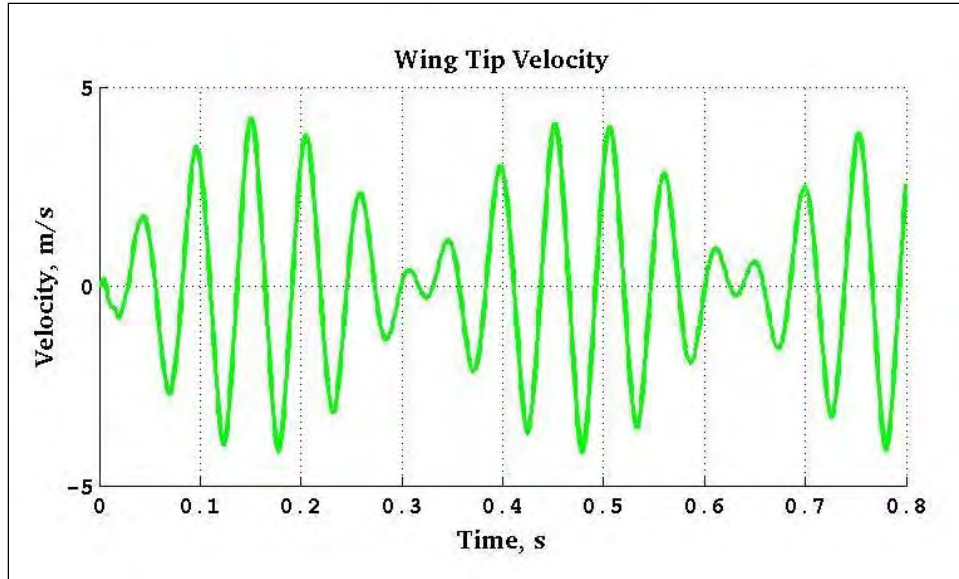
Figure 26. Model 3 wing tip velocity.

4. Discussion and Future Work

4.1   Short-term Objectives

The primary short-term objective is to obtain the displacement data for the PZT in the
experimental model. This exact same motion could then be applied to the computational model.
Making sure that all other material parameters were consistent, the experimental and
computational models could then be compared. This would serve as a validation for the MBDyn
model as well as lead into other interesting studies involving the comparison of MBDyn results
and experimental results. Models to be explored consist of varying the type of excitation
function. Due to the beating seen in these models, it is apparent that the excitation amplifies the
motion to a certain limit and then it interferes. In addition, adding pitch to the mix should create
for some interesting results.

As pointed out several times, modeling the membrane accurately with 1-D beams is going to be a
challenge. Trade studies will be done to determine how sensitive the response is to mesh
refinement, changing the value of EA that is prescribed to the representative beam elements, etc.
This could consist of scaling Young's modulus as well as the cross-sectional area of the
representative beams.

Another very important short-term objective is to begin the process of pairing MBDyn with an
external computational fluid dynamics (CFD) tool. An MBDyn model can be set up to
communicate with external software via an edge communicator. Essentially, MBDyn is told to
print specified data at every time step iteration to a data file. The external CFD tool does the

same, and the two software share this file, which is called an edge communicator. The communicator tells both MBDyn and the CFD tool when to read data and when to stop reading data. The long-term objectives discussed in section 4.2 all depend on this capability. Detailed design of FW models requires accurate aeroelastic analysis of the system dynamics. In addition, the aerodynamics involved with FW flight include 3-D unsteady effects dominated by vortex flows and wing-wake interaction, thus requiring an analysis capable of fluid-structure interaction. This means conducting both structural and fluid analysis simultaneously because the output of one analysis is the input to the other and vice-versa. In addition, including the aerodynamic forces will act as a system damper. This will play a key role in having the system approach a limit cycle.

4.2 Long-term Objectives

The ultimate objective is to a have methodical approach to the detailed design of FWMAVs. As previously mentioned, the aeroelastic effects involved with flexible wing configurations require an analysis capable of fluid-structure interaction. Once MBDyn is coupled with an external CFD solver, the computational design tool will be completely in place. Optimization is the next big design step, but in order to do this effectively, classifying and parameterizing various FW platforms is crucial. Optimization depends on objective functions, design variables, and constraints, and identifying and defining such variables and constraints is a challenge.

As discussed in section 1, different FW species depend on different flight characteristics. A fly depends on quick forward-flight, a hummingbird depends on hovering and agility, while a bumblebee depends on efficient cruising and hovering. Therefore, different FW platforms will depend on different flight functions as well. One platform may need to be optimized for hovering and agility, while another needs to optimized for cruising efficiency. This is where classification of platforms comes into play. Secondly, the wing topology and wing kinematics must be parameterized. As seen in flapping wing species, wing topologies vary drastically. Determining the geometric parameters that define these various shapes is imperative for successful optimization. Not to mention, there is the need to parameterize wing venation and wing stiffness. In addition, wing kinematics are more easily parameterized as having a range of plunge, pitch, and lead-lag, as well as frequencies and phase differences. Lastly, all of these parameters must be constrained by a variety of metrics, whether it be lift/thrust requirements, controllability, or manufacturing capabilities. Once all of these are defined, trade studies between these parameters can be conducted, and eventually various designs can be optimized based on a variety of objective functions (*13–15*).

5. Conclusions

After using MBDyn to analyze a few flapping wing systems, it is clear that MBDyn has many features that make it a very appealing analysis tool. MBDyn's geometry and element definition are extremely versatile and straightforward, as is its prescribed dynamic motion to the system. MBDyn is capable of leveraging math libraries for eigenvalue analysis and can even be coupled with an external CFD solver. All of these features are important for computational design, making MBDyn a nearly perfect candidate.

The research did reveal some modeling issues, in particular the problem of equivalent continuum. Representing the wing surface as a network of 1-D beams is difficult, especially when using an unstructured mesh. Using polyethylene material properties is not necessarily the proper approach. As the mesh becomes finer, more beams are added making the structure stiffer. In addition, to maintain the total mass of the system as the mesh becomes finer, the beams need to become thinner, which again affects the stiffness. Developing an accurate equivalent continuum method is crucial for future modeling of FW systems. This problem does not arise for rotor blade analysis, because airfoil data are used to represent the blade surface.

In conclusion, MBDyn is a wonderful candidate for dynamic analysis of aerial vehicle platforms across the board. Documented applications of using MBDyn for rotor blade analysis prove its capability in that field. This research demonstrated MBDyn's ability to model FW systems. Assuming the issue of equivalent continuum is addressed, MBDyn is a strong candidate to be used for FW analysis.

6. References

1. Flickr Web site. http://farm3.static.flickr.com/2010/1938408406_66eea488cb.jpg (accessed June 21, 2010).

2. Chris Thomas, Jr., Web page. http://homepages.tesco.net/~chris.jrthomas/imp_bumblebee_wing.jpg (accessed June 21, 2010).

3. Amateur Entomologists' Society Web site. http://www.amentsoc.org/images/insect-wing-structure.jpg (accessed June 21, 2010).

4. Flickr Web site. http://farm2.static.flickr.com/1348/761546412_0cdd393580.jpg (accessed June 21, 2010).

5. Hall, A. Personal communication, Motile Robotics, Inc., Aberdeen, MD, June 2010.

6. Riddick, J. Personal communication, ARL-VTD, Aberdeen, MD, June 2010.

7. *MBDyn Input Manual*. Dipartimento i Ingegneria Aerospaziale of the University Politecnico di Milano. Maintained by mbdyn@aero.polimi.it. July 15, 2009. (accessed June 14, 2010).

8. *MBDyn Tutorials*. Dipartimento i Ingegneria Aerospaziale of the University Politecnico di Milano. Maintained by mbdyn@aero.polimi.it. July 15, 2009. (accessed June 14, 2010).

9. Shen, J. Introduction to MBDyn Analysis. MBDyn Training Presentation. National Institute of Aerospace. Hampton, VA.

10. Odegard, G.; Gates, T. *Equivalent Continuum Modeling of Nano-Structured Materials*; NASA/TM-2001-210863; Langley Research Center: Hampton, VA, May 2001.

11. Song, J. et al. An Analytical Study of Two-Dimensional Buckling of Thin Films on Compliant Substrates. Department of Mechanical Science and Engineering, University of Illinois. *J. of Applied Physics* **2008**, *103*, 014303.

12. Tada, S.; Dong, C.; Tarbell, J. Effect of the Stress Phase Angle on the Strain Energy Density of the Endothelial Plasma Membrane. *Biophysical Journal* **November 2007**, *93*, 3026–3033.

13. Isogai, K.; Harino, Y. Optimum Aeroelastic Design of a Flapping Wing. Nippon Bunri University. *Journal of Aircraft* **Nov–Dec 2007**, *44* (6).

14. Wu, P.; Stanford, B.; Ifju, P. *Structural Deformation Measurements of Anisotropic Flexible Flapping Wings for Micro Air Vehicles*; AIAA 2008-1813, University of Florida. .

15. Canfield, R. Personal communication, Virginia Polytechnic Institute, Blacksburg, VA, June 2010.

16. *MBDyn Applications*. Dipartimento i Ingegneria Aerospaziale of the University Politecnico di Milano. Maintained by mbdyn@aero.polimi.it. February 28, 2010. (accessed June 14, 2010).

17. Rajneesh, S. Personal communication, ARL-VTD, Aberdeen, MD, June 2010.

Appendix A. Sample Mbdyn Input

```
begin: data;
    problem: initial value;
end: data;

begin: initial value;
    initial time:   0.0000e+00;
    final time:    1.0000e+00;
    time step:    1.0000e-03;
    max iterations: 100;
    tolerance:    1.0000e-05;
end: initial value;

begin: control data;
    structural nodes:
        +1      # clamped node
        +113     # other nodes
    ;
    rigid bodies:
        +296     # mass of nodes
    ;
    joints:
        +1      # ground clamp
        +1      # total joint
    ;
    beams:
        +296     # nodal connectivity
    ;
end: control data;

set: real j =   0.0000e+00;

begin: nodes;
    structural: 1, static,
        -.1, 0., 0.,
        eye,
        null,
        null;
    structural: 2, dynamic,
         5.9909e-02,   2.9994e-02,   0.0000e+00,
        eye,
        null,
        null;
    structural...
    ...
    structural: 114, dynamic,
```

```
         5.5342e-02,    2.5161e-02,    0.0000e+00,
       eye,
       null,
       null;
end: nodes;

set: real initial_time =    0.0000e+00;
set: real frequency =    1.2470e+02; # radians
set: real amplitude =    1.0000e+00;
set: real initial_value =    0.0000e+00;

drive caller: 100, sine, initial_time, frequency, amplitude, forever, initial_value;

reference: 1000,
     null,
     eye,
     null,
     null;

begin: elements;
     joint: 10, clamp, 1, node, node;
     joint: 20, total joint,
         1,
             position, reference, 1000, null,
             position orientation, reference, 1000, eye,
             rotation orientation, reference, 1000, eye,
         16,
             position, reference, 1000, null,
             position orientation, reference, 1000, eye,
             rotation orientation, reference, 1000, eye,
         position constraint,
             active, active, active,
                 0.,0.,.001,
                 reference, 100,
         orientation constraint,
             active, active, active,
                 0.0, 0.0, 0.,
                 reference, 100;

     body: 1, 2,
         5.3988e-06,
         -3.2671e-04,   -2.0016e-03,    0.0000e+00,
         diag,   0.0000e+00,    7.4019e-12,    7.4019e-12;
     beam2: 1,
         2, null,
         41, null,
         eye,
         linear elastic generic,
             diag,    8.5322e+02,    8.5322e+02,    8.5322e+02,    1.7674e-04,    7.1102e-05,
```

```
1.0564e-04;

    body: 2, 2,
          4.2517e-06,
         -2.0639e-03,    1.0000e-08,    0.0000e+00,
         diag,    0.0000e+00,    6.0372e-12,    6.0372e-12;
    beam2: 2,
         2, null,
         3, null,
         eye,
         linear elastic generic,
             diag,    1.5000e+02,    1.5000e+02,    1.5000e+02,    2.5000e-05,    1.2500e-05,
1.2500e-05;

    body...
    ...

    body: 296, 113,
          3.3209e-06,
          1.2218e-03,   -1.0517e-03,    0.0000e+00,
         diag,    0.0000e+00,    2.8769e-12,    2.8769e-12;
    beam2: 296,
         113, null,
         114, null,
         eye,
         linear elastic generic,
             diag,    1.5000e+02,    1.5000e+02,    1.5000e+02,    2.5000e-05,    1.2500e-05,
1.2500e-05;

end: elements;
```

.

U.S. Army Research Laboratory
SUMMER RESEARCH TECHNICAL REPORT

Evaluating Strategies to Open Doors via Compliant Methods

DANIEL CARLTON SMITH
CHAD KESSENS
UNMANNED SYSTEMS, VEHICLE TECHNOLOGIES DIRECTORATE,
ABERDEEN PROVING GROUND

Contents

List of Figures

Abstract

Despite numerous advances in the field of robotics, robots remain astonishingly poor at some simple tasks, such as opening doors. In urban combat environments, doors are a common hindrance to autonomous exploration. As robots continue to enhance Soldier safety by increasing their role in combat environments, autonomous navigation of doors will become ever more important. Therefore, the objective of this project was to implement and evaluate various strategies for opening doors with a robotic manipulator through computer simulation. A high-fidelity physics engine, Open Dynamics Engine, was used to model the Mitsubishi PA10 7-degree-of-freedom manipulator in C++.   To examine the robustness of each strategy to real-world challenges, door characteristics and environments were varied in simulation. Environments analyzed included hallways, rooms, and staircase landings. Characteristics analyzed encompassed the direction of the door's motion, swing radius, and presence or absence of auto-closure devices. Various strategies for opening and closing doors were then implemented in the simulation. These included whole-body motion using full and selected joint compliance, real-time path planning, and equilibrium point control. The robustness and speed of these strategies were then evaluated across the various scenarios.

Acknowledgments

INTENTIONALLY LEFT BLANK.

1. Introduction and Background

1.1 Door Opening Problem

In modern combat settings, thorough exploration of an environment is necessary to ensure safety and mission success. Enormous risks are involved with the exploration of hostile areas, and robots are frequently used to overcome these risks. Unfortunately, robots still perform poorly when presented with tasks such as successfully navigating and manipulating foreign environments.

The inability to open doors speedily remains one of the most common and largest barriers to a robot's usefulness in these situations. The primary reason for this is the door's constrained nature. Small errors in the manipulator's path can create large internal forces, potentially causing damage to the robot and/or doorway and resulting in a failure to successfully manipulate the door. In addition, doors can be found with widely varying features and in widely varying environments. They have different masses, swing radii, closing apparatuses, and directions of motion. The location of a door may be in an open area or in a confined space. Due to these variations, a single strategy may not be optimized for or capable of handling the generic problem. Because of this, different strategies may be better suited to handle the problem given different scenarios. Therefore, this paper compares the effectiveness of several door opening strategies in terms of their speed and robustness to the problem in various scenarios.

1.2 Door Opening Strategies

Compliance has been shown to greatly improve both the speed and probability of success of door opening manipulators (*1*). Allowing compliance in the system enables internal forces to resolve themselves. This, in turn, prevents binding and increases the odds of success as well as the safety of the action. Compliance can be achieved in a number of ways including through backdrivability, the implementation of clutch mechanisms, or inverse dynamics. However, the method of achieving compliance is outside the scope of this paper.

To effectively make use of compliance, several strategies have been suggested. First, the door might be controlled completely by the mobility platform, using fully compliant manipulator joints. This could be implemented with a straight-line mobility path or with real-time course correction. Another strategy might involve controlling the door with a single manipulator joint, where the remaining joints are freely compliant. This would reduce the travel distance necessary for the mobility platform. These strategies might also be combined to handle scenarios where space is limited.

Finally, equilibrium point control represents the current state-of-the-art in door manipulation (*2*). In this strategy, each joint is modeled as a virtual spring, enabling motion with low impedance

control. This control method will be implemented in simulation and will be used for comparison against the other strategies.

1.3 Door Opening Scenarios

The optimal strategy for opening a door likely depends on the scenario in which the door is placed. Several scenarios were used for testing. These included settings where the door was located in a corner of a room, at the end of a hallway, and at the top of a landing for a flight of stairs. Additionally, we considered that the most appropriate strategy could depend on the swing radius of the door, the mass of the door, and the direction in which the door opens. The presence of auto-closure devices was also considered. This included auto-closure both as a constant and as a linearly increasing force.

1.4 Hardware

The Mitsubishi PA10 robot arm is a commonly used 7-degree-of-freedom (7-DOF) robotic arm. It contains seven rotational joints, arranged as alternating pivots and hinges. The PA10 attempts to create a crude model of the human arm and is separated into shoulder, elbow, and wrist components (*3*). The PA10 was selected for use in this project because of its availability, range of motion, and ubiquitous use in robotics research.

1.5 Simulation and Physics Engines

Computer simulation is an important part of analyzing potential solutions to robotic design problems. Simulations are a simple, cost-effective, and safe alternative to field testing in assessing the quality of prospective designs. To successfully model compliance, physical dependability is necessary.

Physics engines are programming frameworks that use iterative methods to approximate rigid body dynamics, making high-fidelity simulation possible without extensive mathematical modeling. Simulations that rely on physics engines provide a high-fidelity physical model while using minimal computing power. In addition, performing experiments in simulation allows results to be obtained much more quickly and safely than conducting physical experiments. For these reasons, evaluating various strategies and scenarios relevant to the door opening problem through the use of computer simulation is incredibly practical.

1.6 Basis for Selecting Open Dynamics Engine

Open Dynamics Engine (ODE) was selected for use based on previous research comparing various criteria important for use in robotic simulation through assessing both physical fidelity and ease of development (*4*). In the cited comparison, a weighted selection matrix was built that contained a list of important features when using a physics engine. ODE was among the physics engines ultimately selected for its ease of use and accurate physics models. Based on these results, ODE was selected for use in the door opening simulation.

1.7 Language Selection

ODE is implemented in the C programming language, a highly popular, procedural programming language. Wrappers for other languages exist, but most of these are poorly documented, out of date, or incompatible with the current version of ODE. The C implementation of ODE was compiled to a dynamically linked library for use with the project.

Because of the robust nature of the door opening problem and the breadth of scenarios constructed, an object-oriented implementation in C++ was used in favor of a simple procedural approach. This object-oriented approach allows for the implementation of separate, independent modules, making it easier to implement different scenarios without rewriting a significant amount of code.

2. Experiment and Calculations

2.1 Implementation of Manipulator

A generic 3-degree-of-freedom (3-DOF) manipulator was built in ODE as a proof of concept. The manipulator, shown in the figure 1, contains three rotational degrees of freedom, arranged as a pivot joint and two hinge joints.
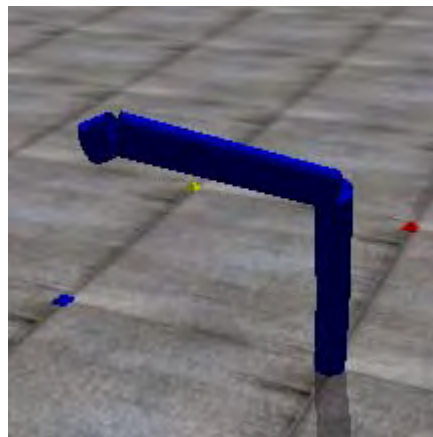
Figure 1. Generic 3-DOF manipulator.

Upon completion of a generic manipulator, the PA10 was coded. The PA10 contains seven rotational joints, each an alternating pivot or hinge. The model, depicted in figure 2, shows the constructed PA10 robotic arm approaching a generic door in the corner of a room. When the PA10 arm is implemented in ODE, it becomes possible to simulate and evaluate the different scenarios for opening the door.
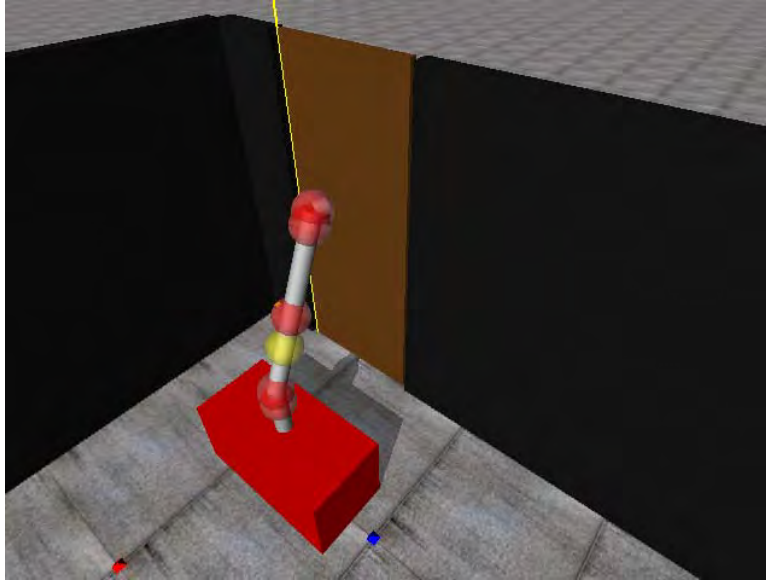
Figure 2. Robot equipped with PA10 arm approaching a door.

2.2   Forward and Inverse Kinematics

All the strategies used in the door opening problem require the simulation to attach the robotic arm to a door either before or during the simulation. Inverse kinematics was necessary to determine the appropriate joint angles needed to attach the end effector to the door (figure 3).
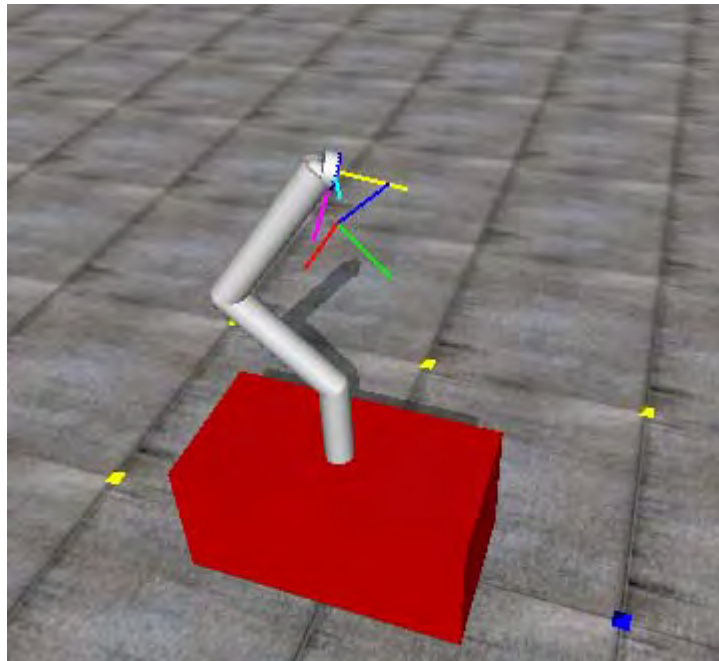
Figure 3. PA10 arm using inverse kinematics to reach a destination.

While forward kinematics seeks to determine the location of an end effector based on joint angle, inverse kinematics attempts to determine a set of joint angles that a robotic arm needs to satisfy a given end-effector position and orientation.

Inverse kinematic equations for the PA10 were evaluated using transformation matrices of Denavit-Hartenberg parameters. Generic inverse kinematic equations from *Robot Modeling and Control* were applied to the PA10 (*5*). A separate matrix class was constructed to supplement the existing code in ODE and ensure that the inverse kinematic equations presented could be successfully compared with the appropriate forward kinematic solutions.

In addition to inverse kinematics, a brute force method called Cyclic Coordinate Descent was used to navigate the end effector to a desired position. This method simply iterates through the joints and attempts to move the end effector closer to its desired position by finding the optimal angle for each joint. By cycling through all the joints several times, the arm typically becomes as close as possible to the target position. However, because of its brute force nature, this method requires significantly more computing power than solving the inverse kinematic equations and is less than ideal for situations in which speed matters, such as the door opening problem.

2.3 Strategy Implementation

At the time of this paper's completion, the only strategy that had been simulated was a free arm controlled entirely by a mobility platform (figure 4). Given the progress and modularity of the code written, it should not be difficult to continue to implement various door opening strategies into the simulation.
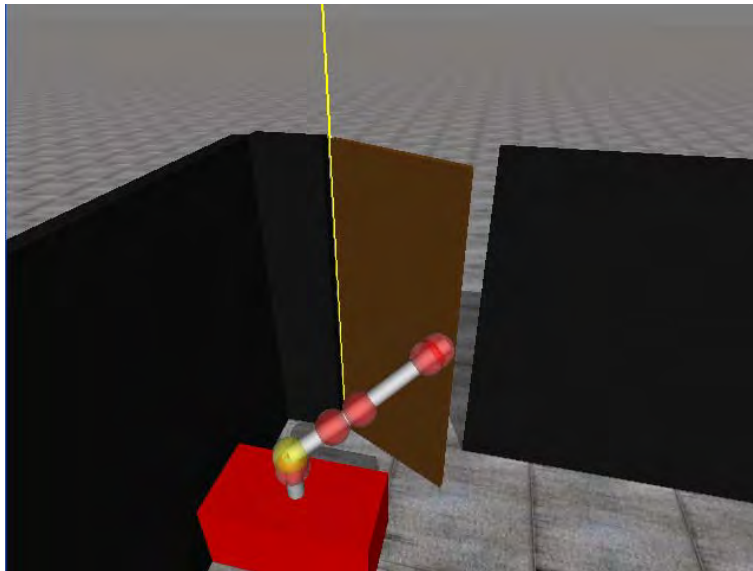
Figure 4. Using mobility platform to open a door.

153

After the complete construction and evaluation of the free joints controlled by the mobility platform, a model will be built that includes individually controlled joints. Data from the simulated joint encoders will be used to implement single-joint active control and attempt to determine the dynamics of the door.

A third scenario will use initial impulses rather than data from joint encoders to attempt to model the physics of the door. The door weight and friction will be estimated based on these initial impulses.

Finally, equilibrium point control, as described by Jain and Kemp (*2*), will be simulated. Equilibrium control has been shown to be an effective method of opening doors and drawers in the past. This differs from the previous scenarios in that the dynamics of the door are not considered. Rather, "springs" are applied to arms to simulate the muscle found in living beings, and the links in the arm are allowed to travel to their equilibrium points. These equilibrium points are then modified to control the arm.

After each scenario is implemented, the scenarios will be compared based on several criteria. These criteria include the predicted speed at which the scenario can be completed on a physical PA10 manipulator and the force and torque at the end effector. The control schemes with online dynamics models will be compared to equilibrium point control in an attempt to determine the benefits of using these physical models.

3. Results and Discussion

3.1 Physical Fidelity of ODE

The physical fidelity of ODE appears to be great enough to successfully implement a robot, manipulator, and door in a simulation environment. Occasional joint instability was present when the robot was attached to the ground with a fixed joint and when the arm initially attached its gripper to the door. In both cases, the links in the arm appeared to bounce beyond the constraints of the joints connecting them. In addition, the door occasionally glided slightly away from its axis when its initial position and orientation were reset.

3.2 Results of Individual Strategies

We are continuing to work on the results of applying the various strategies discussed in section 2.3. At the time of this publication, no results are available. These results will be published in a future document once the project has been completed.

4. Summary and Conclusion

This paper discussed the difficulties associated with the door opening problem, several strategies for opening a door using a Mitsubishi PA10 robot arm, and the benefit of simulation and its applicability to the door opening problem. A PA10 robotic arm was constructed in ODE, and inverse kinematics for the arm and robot were implemented. Several strategies for opening the door were tested and evaluated, and an online model of the door's dynamics was estimated.

5. References

1. Kessens, C. C.; Rice, J. B.; Smith, D. C.; Biggs, S. J.; Garcia, R. Utilizing Compliance to Manipulate Doors With Unmodeled Constraints. *IEEE/RSJ International Conference on Intelligent Robots and Systems.* Taipei, submitted 2010.

2. Jain, A; Kemp, C. C. Pulling Open Novel Doors and Drawers with Equilibrium Point Control, *IEEE-RAS International Conference on Humanoid Robotics (Humanoids)*, 2009.

3. Mpompos, N.A.; Artemiadis, P. K.; Oikonomopoulos, A. S.; Kyriakopoulos, K. J. Modeling, full identification and control of the mitsubishi pa-10 robot arm, *IEEE/ASME International Conference on Advanced Intelligent Mechatronics*, Switzerland, 2007.

4. Rice, J. B.; Smith, D. C. *Fidelity Evaluation of Physics Engines for Manipulation;* U.S. Army Research Laboratory, 2009.

5. Spong, M. W.; Hutchinson, S.; Vidyasagar, M. *Robot Modeling and Control;* John Wiley & Sons, Inc.: New York, 2006.

Weapons & Materials Research Directorate (WMRD)

INTENTIONALLY LEFT BLANK.

U.S. Army Research Laboratory
SUMMER RESEARCH TECHNICAL REPORT

Roll-Stable Projectile Flight Dynamics Analysis for Precision Applications

JOHN W. DYKES, STUDENT
DR. FRANK FRESCONI, MENTOR
FLIGHT SCIENCES BRANCH, LETHALITY DIVISION,
ABERDEEN PROVING GROUND

Contents

List of Figures

List of Tables

Abstract

There is growing interest to move away from unguided munitions towards higher-precision, guided munitions. While these smart projectiles allow for increased probability of hitting a target and lower collateral damage, controller systems for these munitions are required to be small, rugged, yet affordable. Factors contributing to higher costs include complex guidance, navigation, and control (GNC) algorithms, onboard energetics (thrusters), and large battery power demands. One idea to potentially reduce these issues is the concept of naturally roll-stable V-tailed projectiles. Similar to paper airplanes, a roll-stable projectile would be capable of uprighting itself during flight, due to aerodynamic loading in a gravity environment. Implementation of this concept would provide numerous advantages to flight control systems, including reduced actuator burden, higher maneuverability, reduced sensor burden, and simplified GNC algorithms. The scope of this study is to gain insight into the flight mechanics of roll-stable projectiles. A flight dynamic model for asymmetric V-tailed projectiles was developed to replicate flight characteristics observed from initial testing. Next, parametric variation of V-tail geometric parameters was performed. Results from these studies indicate that naturally roll-stable projectiles can exist. Conclusions of this study are based on aerodynamic predictions and rigid 6-degree-of-freedom trajectory simulation.

Acknowledgments

INTENTIONALLY LEFT BLANK.

1. Introduction

Projectiles such as mortars and artillery are used to hit targets; however, a number of conditions can cause rounds to miss an intended target. These conditions include variable atmospheric conditions, firing platform motion, aiming errors, and manufacturing inaccuracies of the gun tube, propellant, and projectile. With the advent of low-cost, small, rugged micro-electro-mechanical systems, dramatic reduction in dispersion for projectiles equipped with a flight control system is possible. While these smart projectiles allow for increased probability of hitting a target, as well as lower collateral damage, control systems for these munitions are required to be small and rugged, yet affordable.

Factors contributing to higher costs include complex guidance, navigation, and control (GNC) components; onboard energetics (thrusters); and large battery power demands. Simplifying GNC systems effectively reduces cost, but there are many hurdles that result from adherence to conventional projectile designs. For example, projectiles are fired out of rifled or smooth-bore guns, which dictate the static stability. For statically unstable rounds, extremely high roll rates are imparted on the projectile in a rifled gun barrel. To control these spin-stabilized rounds, the GNC algorithm is required to process data from high quality positional and rate sensors, and coordinate in control mechanism actuators with extremely fast response times. These factors stress the available technology and drive up the cost. Statically stable projectiles can mitigate these issues because they ideally do not require spin to fly efficiently; however, sophisticated sabot/fin-deployment designs are often used, which again increase system complexity. Also, fin configurations are often canted to induce a smaller, but still considerable, amount of spin so as to "roll out" aerodynamic and mass asymmetries, thus reducing ballistic dispersion and increasing precision.

One idea to potentially reduce these issues is to employ aerodynamic and mass asymmetries to the benefit of the control system. Specifically, asymmetric projectile airframes exist that do not require spin. Similar in characteristic to the flight mechanics of a paper airplane, these asymmetric airframes might also have the ability to naturally upright while in flight. If these naturally uprighting, roll-stable projectiles exist, and at the same time possess favorable flight characteristics, then this concept would provide numerous advantages in smart projectile applications, including reduced actuator burden, higher maneuverability, reduced sensor burden, and simplified GNC algorithms.

Figure 1 shows the concept of a V-tailed projectile airframe, which is investigated in this study. Similar to paper airplanes, a roll-stable projectile would be capable of uprighting itself naturally during flight due to aerodynamic loading in a gravity environment. The scope of this study is to gain insight into the flight mechanics of V-tailed projectiles. A flight dynamic model for asymmetric V-tailed projectiles was developed to replicate flight characteristics observed from

initial testing. Next, parametric variation of V-tailed geometric parameters was performed, and finally, naturally uprighting roll-stable airframes were identified.
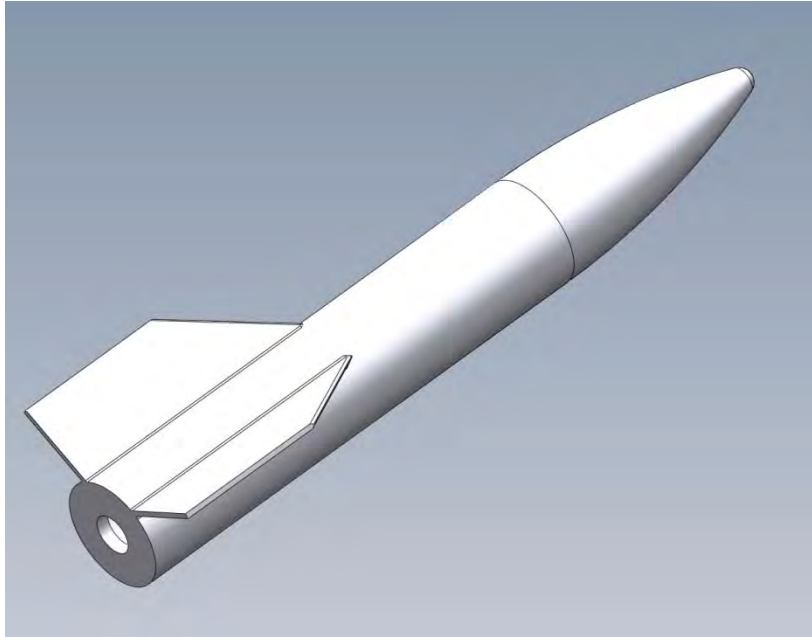
Figure 1. A 3-D rendering of a V-tailed airframe for proposed naturally upright, roll-stable flight characteristics.
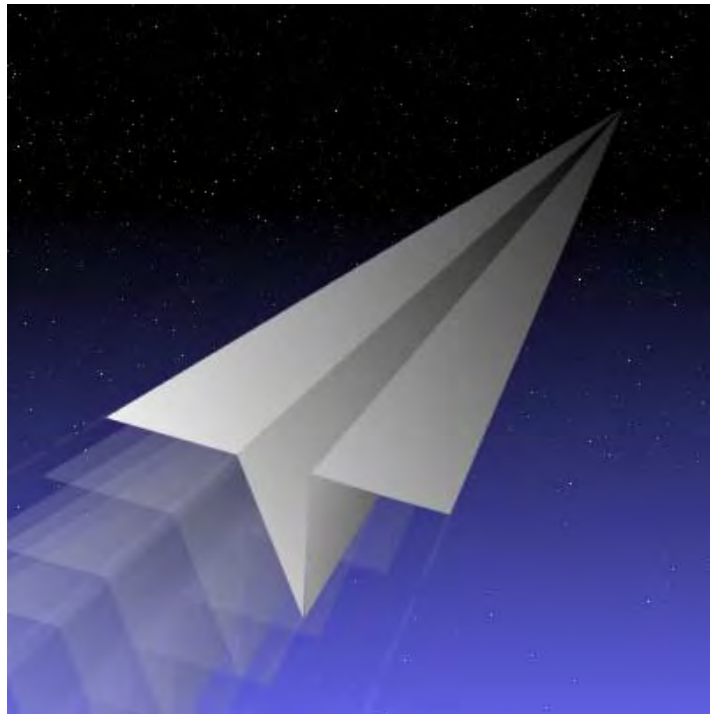
Figure 2. Similar to paper airplanes, V-tailed projectile airframes utilize to flat aerodynamic surfaces located above the center of mass for naturally upright roll-stable flight.

2. Projectile Flight Dynamic Model

2.1 Equations of Motion

The non-linear trajectory simulation used in this study is a standard 6-degree-of-freedom (6DOF) model typically used in flight dynamic modeling of projectiles. The 6DOF includes three components of the center of gravity (CG) position vector (x,y,z) and three Euler projectile orientation angles (ϕ,θ,ψ), referenced to an inertial frame. Refer to figure 3 for an illustration of a projectile possessing 6 degrees of freedom.
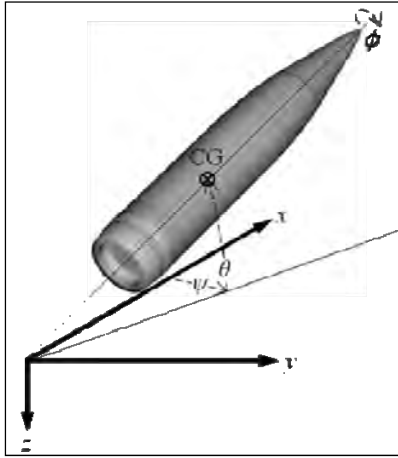
Figure 3. Projectile axes (x,y,z) and Euler angles (ϕ,θ,ψ).

The kinematic and dynamic equations for the 6DOF system are provided in equations 1–4, as derived by McCoy [1] and Carlucci [2].

$$\begin{Bmatrix} \dot{x} \\ \dot{y} \\ \dot{z} \end{Bmatrix} = \begin{bmatrix} c_\theta c_\psi & s_\phi s_\theta c_\psi - c_\phi s_\psi & c_\phi s_\theta c_\psi + s_\phi s_\psi \\ c_\theta s_\psi & s_\phi s_\theta s_\psi + c_\phi c_\psi & c_\phi s_\theta s_\psi - s_\phi c_\psi \\ -s_\theta & s_\phi c_\theta & c_\phi c_\theta \end{bmatrix} \begin{Bmatrix} u \\ v \\ w \end{Bmatrix}$$

(1)

$$\begin{Bmatrix} \dot{\phi} \\ \dot{\theta} \\ \dot{\psi} \end{Bmatrix} = \begin{bmatrix} 1 & s_\phi t_\theta & c_\phi t_\theta \\ 0 & c_\phi & -s_\phi \\ 0 & s_\phi / c_\theta & c_\phi / c_\theta \end{bmatrix} \begin{Bmatrix} p \\ q \\ r \end{Bmatrix}$$

(2)

$$\begin{Bmatrix} \dot{u} \\ \dot{v} \\ \dot{w} \end{Bmatrix} = \begin{Bmatrix} X/m \\ Y/m \\ Z/m \end{Bmatrix} - \begin{bmatrix} 0 & -r & q \\ r & 0 & -p \\ -q & p & 0 \end{bmatrix} \begin{Bmatrix} u \\ v \\ w \end{Bmatrix}$$

(3)

$$\begin{Bmatrix} \dot{p} \\ \dot{q} \\ \dot{r} \end{Bmatrix} = [I]^{-1} \left[\begin{Bmatrix} L \\ M \\ N \end{Bmatrix} - \begin{bmatrix} 0 & -r & q \\ r & 0 & -p \\ -q & p & 0 \end{bmatrix} [I] \begin{Bmatrix} p \\ q \\ r \end{Bmatrix} \right]$$

(4)

In equations 1 and 2, standard shorthand notation for trigonometric functions is used: $s_\alpha = \sin(\alpha)$, $c_\alpha = \cos(\alpha)$, and $t_\alpha = \tan(\alpha)$. *X,Y,Z* and *L,M,N* are the force and moment components appearing in equations 3 and 4. Three translational velocity components (*u,v,w*) and three angular velocity components (*p,q,r*) are related to the time rate of change of the position vector (*x,y,z*) and orientation angles (ϕ,θ,ψ), respectively. Also, *m* and *I* represent the projectile total mass and inertia tensor.

2.2 Gravity and Aerodynamic Modeling

Projectile body forces were modeled using superposition with contributions from gravity (G), body aerodynamics (A), and fins (F). Using superposition, the force components are decomposed, as shown in equation 5.

$$\begin{Bmatrix} X \\ Y \\ Z \end{Bmatrix} = \begin{Bmatrix} X_G \\ Y_G \\ Z_G \end{Bmatrix} + \begin{Bmatrix} X_A \\ Y_A \\ Z_A \end{Bmatrix} + \begin{Bmatrix} X_F \\ Y_F \\ Z_F \end{Bmatrix}$$

(5)

The dynamic equations are expressed in a body fixed reference frame, thus all forces acting on the body are expressed in the projectile reference frame. The force-acting due to gravity is shown in equation 6.

$$\begin{Bmatrix} X_G \\ Y_G \\ Z_G \end{Bmatrix} = mg \begin{Bmatrix} -s_\theta \\ s_\phi c_\theta \\ c_\phi c_\theta \end{Bmatrix}$$

(6)

The body aerodynamic force-acting at the center of pressure (COP) of the projectile is given by equation 7.

$$\begin{Bmatrix} X_A \\ Y_A \\ Z_A \end{Bmatrix} = -\frac{\pi}{8} \rho V^2 D^2 \begin{Bmatrix} C_{X0} + C_{X2}(v^2 + w^2)/V^2 \\ C_{NA} v /V \\ C_{NA} w /V \end{Bmatrix}$$

(7)

The aerodynamic force coefficients are zero-yaw drag (C_{XO}), yaw drag (C_{X2}), and normal force slope due to angle of attack (C_{NA}). Atmospheric density is expressed as ρ, and the projectile diameter and total velocity are *D* and *V*, respectively. The fin forces will be discussed in the next section.

The applied moments about the projectile mass center contains contributions from steady aerodynamics (SA), unsteady aerodynamics (UA), and fins (F).

$$
\begin{Bmatrix} L \\ M \\ N \end{Bmatrix} = \begin{Bmatrix} L_{SA} \\ M_{SA} \\ N_{SA} \end{Bmatrix} + \begin{Bmatrix} L_{UA} \\ M_{UA} \\ N_{UA} \end{Bmatrix} + \begin{Bmatrix} L_F \\ M_F \\ N_F \end{Bmatrix}
$$

(8)

The moment components due to steady aerodynamic forces and control forces are computed by the cross product between the distance vector from the mass center to the location of the specific force and the force, itself. The unsteady body aerodynamic moment provides a damping source for projectile angular motion and is given by equation 9.

$$
\begin{Bmatrix} L_{SA} \\ M_{SA} \\ N_{SA} \end{Bmatrix} = \frac{\pi}{8} \rho V^2 D^3 \begin{Bmatrix} C_{LDD} + \dfrac{pDC_{LP}}{2V} \\ \dfrac{qDC_{MQ}}{2V} \\ \dfrac{qDC_{MQ}}{2V} \end{Bmatrix}
$$

(9)

The aerodynamic moment coefficients are the roll moment due to fin cant (C_{LDD}), roll-damping moment (C_{LP}), and pitch damping moment (C_{MQ}).

2.3   V-tailed Fin Model

The fin forces are modeled as aerodynamic lifting surfaces, where the force due to a single fin is modeled as a point force-acting at the lifting surface aerodynamic center of pressure. The moment generated due to lift about the fin quarter-chord is neglected in this study. Fin orientation on the projectile is defined as a set of three body-fixed rotations about the projectile reference frame. Starting with the canard axis aligned with the projectile body axis, the ith fin is rotated about the $\hat{\imath}_B$ axis by the azimuthal angle (ϕ_i), then about the resulting intermediate k-axis by the sweep angle (γ_i). A third angle, the fin cant angle (δ_i), will be addressed when defining local fin angle of attack. If all three fin angles are zero, the lifting surface is in the $\hat{\imath}_B$ - $\hat{\jmath}_B$ plane. The transformation from the ith fin reference frame to the parent projectile body axis is given by equation 10.

$$
T_i = \begin{bmatrix} c_{\gamma_i} & -s_{\gamma_i} & 0 \\ c_{\phi_i} s_{\gamma_i} & c_{\phi_i} c_{\gamma_i} & -s_{\phi_i} \\ s_{\phi_i} s_{\gamma_i} & s_{\phi_i} c_{\gamma_i} & c_{\phi_i} \end{bmatrix}
$$

(10)

Using equation 10, the body referenced air velocities u, v, and w of equation 3 can be transformed into the ith fin reference frame as u_i, v_i, and w_i, to obtain local angle-of-attack for aero calculations. The vector components r_{xi}, r_{yi}, and r_{zi} represent the distances between the projectile CG and the ith fin.

$$\begin{Bmatrix} u_i \\ v_i \\ w_i \end{Bmatrix} = [T_i]^T \left[\begin{Bmatrix} u \\ v \\ w \end{Bmatrix} + \begin{bmatrix} 0 & -r & q \\ r & 0 & -p \\ -q & p & 0 \end{bmatrix} \begin{Bmatrix} r_{xi} \\ r_{yi} \\ r_{zi} \end{Bmatrix} \right] \tag{11}$$

From this, the fin forces can be modeled as a function of the local angle-of-attack, which for the ith lifting surface is given by equation 12.

$$\alpha_i = \delta_i + \tan^{-1}\left(\frac{w_i}{u_i}\right) \tag{12}$$

The total aerodynamic force components generated by the two V-tailed fins and expressed in the projectile body frame is given by equation 13.

$$\begin{Bmatrix} X_F \\ Y_F \\ Z_F \end{Bmatrix} = \frac{1}{2}\rho \sum_{i=1}^{2} V_i^2 [T_i] \begin{Bmatrix} C_{Li}\sin(\alpha_i - \delta_i) - C_{Di}\cos(\alpha_i - \delta_i) \\ 0 \\ -C_{Li}\cos(\alpha_i - \delta_i) + C_{Di}\sin(\alpha_i - \delta_i) \end{Bmatrix} \tag{13}$$

The moment components generated by the fins on the projectile body are computed by the cross product between the distance vector from the CG to the location of the ith fin force, previously described. Then components for both fins are summed to obtain the total moment.

The aerodynamic coefficients C_{Li} and C_{Di} are modeled according to the following expressions.

$$C_{L_i} = C_{L1_i}\alpha_i + C_{L3_i}\alpha_i^3 + C_{L5_i}\alpha_i^5 \tag{14}$$

$$C_{D_i} = C_{D0_i} + C_{D2_i}\alpha_i^2 + C_{I_i}C_{L_i}^2 \tag{15}$$

The ith fin COP location and the aerodynamic coefficients, C_{Li} and C_{Di}, are again predicted as functions of Mach number and surface angle-of-attack. The fin transverse COP location was assumed to act in the transverse CG location of the fin.

Along with Mach number and angle-of-attack, the aerodynamic fin coefficients of equations 14 and 15 are also dependent upon fin geometry. Six parameters were identified to be important in evaluating V-tailed airframes for performance: fin width (W_{fin}), fin length (L_{fin}), sweep angle (SA), V-tailed angle (θ_v), a fin offset parameter (h), and fin cant angle. An illustration of these parameters is shown in figure 4.
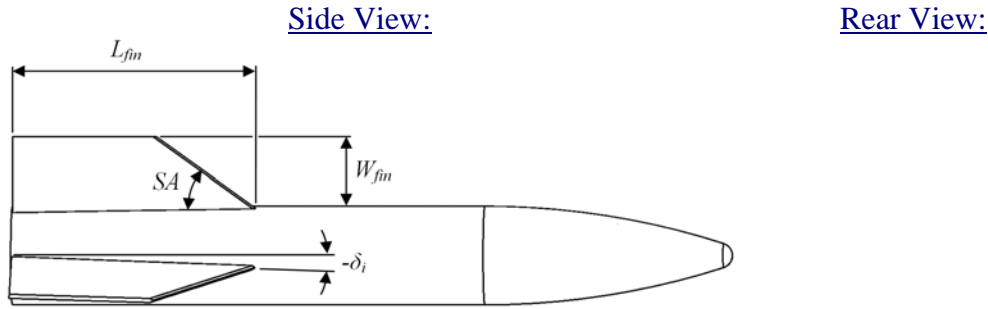
Figure 4. Illustration of V-tailed fin geometry parameter space.

2.4   Simulation Implementation

The dynamic equations given by equations 1–4 are numerically integrated forward in time using a 4th-order, fixed-step Runge-Kutta algorithm. The mass, CG location, and inertia tensor are all assumed to be constant throughout the duration of the flight. The COP location and all aerodynamic coefficients in equations 7, 9, 14, and 15 are estimated using aero-prediction techniques as functions of Mach number and angle-of-attack. During simulation, these coefficients are linearly interpolated.

3.   Results and Discussion

3.1   Projectile Solid Modeling

Customized projectiles were modeled in SolidWorks to obtain exterior geometries and physical properties. These data were used to estimate aerodynamic coefficients. Note that for all 6DOF simulations, the mass, inertia, and CG location were held constant for varied fin configurations. This is because even though modifying fin parameters will consequentially change physical parameters, the changes are expected to be reasonably small, since the fin mass and volume are much smaller than the projectile body.

3.2   Initial Flight Experiments

Initial flight experiments were conducted on asymmetric V-tailed projectiles with different fin configurations. A low-speed airgun was used as a test rig, where roll performance was evaluated by line-of-site observation. Projectile airframes were considered naturally roll-stable if the roll oscillation damped throughout flight when perturbed by an external influence (tip-off conditions, wind gusts, etc.). From these experiments, no airframes were seen to be roll-stable, but otherwise had good flight characteristics—meaning small angles-of-attack were experienced through flight.

Additional tests were performed with video cameras placed in airframes and pusher test articles to observe the roll motion of the projectile. The results of these experiments show that the projectile rolls through multiple cycles with a roll-dependent angular velocity that gradually

increases in frequency through flight. Based on video footage, projectiles were observed to slowly roll counter-clockwise and then, when viewed from behind, change direction as the projectiles became roll-unstable. Also, projectile states at muzzle exit were estimated to be used in 6DOF simulations, as shown in table 1.

Table 1. Projectile initial conditions to be used in a nominal 6DOF simulation.

[x]	**(m):**	0.0000
[y]	**(m):**	0.0000
[z]	**(m):**	0.0000
[ϕ]	**(deg):**	0.0000
[θ]	**(deg):**	30.0000
[ψ]	**(deg):**	0.0000
[u]	**(m/sec):**	202.5000
[v]	**(m/sec):**	0.0000
[w]	**(m/sec):**	0.0000
[p]	**(Hz):**	0.0000
[q]	**(Hz):**	0.0000
[r]	**(Hz):**	0.0000

3.3   6DOF Model Validation

One of the projectile test articles was chosen to be a baseline fin geometry for purposes of 6DOF simulation: L_{fin}=2.42847 (cal), W_{fin}=0.709695 (cal), SA=54.0 (deg), h=0.00 (cal), θ_v=100 (deg), and δ=–1.0 (deg), where 1.0 (cal) is equivalent to the characteristic projectile diameter. Airgun tip-off was estimated (i.e., initial p_o, q_o, and r_o states) until the roll characteristics were observed. The plots shown in figure 5 compare single trajectory results for a projectile with a tip-off of p_o= 0.03 (rad/s), q_o= –0.22 (rad/s), and r_o= 0.052 (rad/s), and without tip-off.
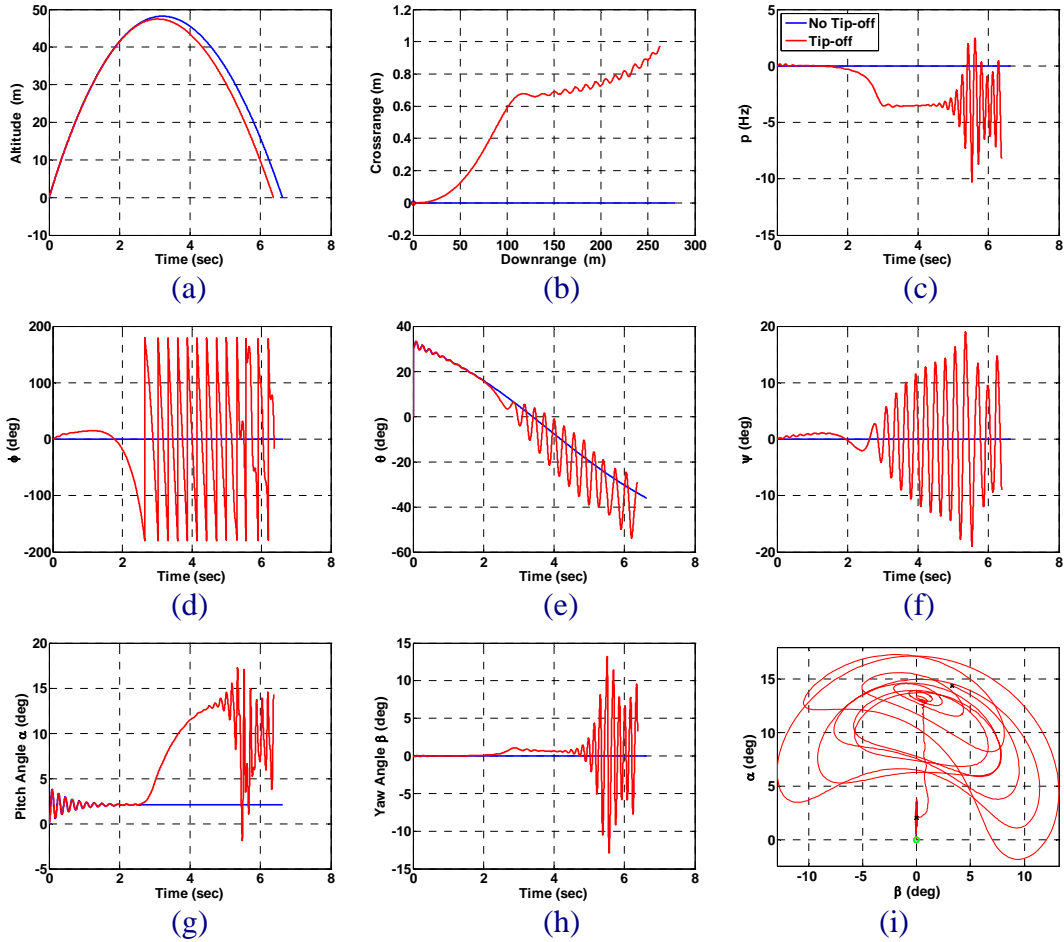
Figure 5. Selected 6DOF simulation plots of the baseline V-tailed projectile with and without estimated tip-off effects including (a) altitude vs. time, (b) deflection vs. time, (c) roll rate vs. time, (d) roll angle vs. time, (e) pitch angle vs. time, (f) yaw angle vs. time, (g) pitch aerodynamic angle-of-attack vs. time, (h) aerodynamic angle of sideslip vs. time, and (i) pitch angle vs. angle of sideslip.

In figures 5(a) and 5(b), trajectory results show that the projectile with tip-off has yaw characteristics. Figures 5(d) –5(e) show Euler angles, where figure 5(c) is the roll rate time history of the projectile throughout flight. As can be seen from both the roll angle and roll rate, the projectile initially begins to slowly roll in the positive direction but then changes direction and starts to roll in a cyclic fashion. The roll rate increases to a nearly constant frequency until late in the flight when oscillations are observed. Note that after approximately 2.5 s of flight, the oscillatory behavior is observed in all three Euler angles. Figures 5(g) and 5(h) show projectile aerodynamic angles' time history. Initial oscillations are observed in the pitch angle but not in the sideslip angle. As time progresses, these angles start to develop growing oscillatory characteristics, which represents decreased flight performance.

3.4   Mechanics Driving Fundamental Projectile Behavior

Several simulations were computed to study the effects of gravity and fin aerodynamics. The contributing forces due to fin geometry are desired to keep the projectile roll-stable in flight, where gravity uprights the projectile during flight. Throughout the trajectory, gravity causes the projectile to follow a near parabolic path in the downrange altitude plane. From this, a small lag exists between the spin-axis and the CG motion, inducing projectile angle-of-attack. The roll-instability is produced from the coupling of this gravity-induced small angle-of-attack and the fins. Inspection of equations 11–13 shows that gravity-induced q and r terms produce asymmetric fin forces on opposite sides of the V-tail, which can drive the roll-instability.

Figure 6 shows selected results from a study investigating the effects of gravity and fin aero on a projectile body. Because this study is purely academic, no tip-off effects were modeled. Also in the absence of fins, the CG was artificially moved forward to eliminate static instabilities commonly observed in finless projectiles. This does not affect motion in the roll direction. Shown in Figures 6(a) and 6(b), the V-tailed projectile in the presence of a gravity environment becomes roll-unstable, even in the absence of tip-off; however, the finless projectile cases do not exhibit any motion in the roll direction. Figure 6(c) shows that the introduction of gravity to the finless projectile introduces oscillations in the vertical plane, and when fins are present, a small offset pitch angle is induced. Once the finned projectile reaches the trajectory apogee, the instability is observed (after approximately 4.3 s of flight). Figure 6(d) shows that the instability in the V-tailed projectile is not isolated to the vertical pitch plane, but is coupled in the lateral yaw plane. This confirms the predictions of equations 11–13.
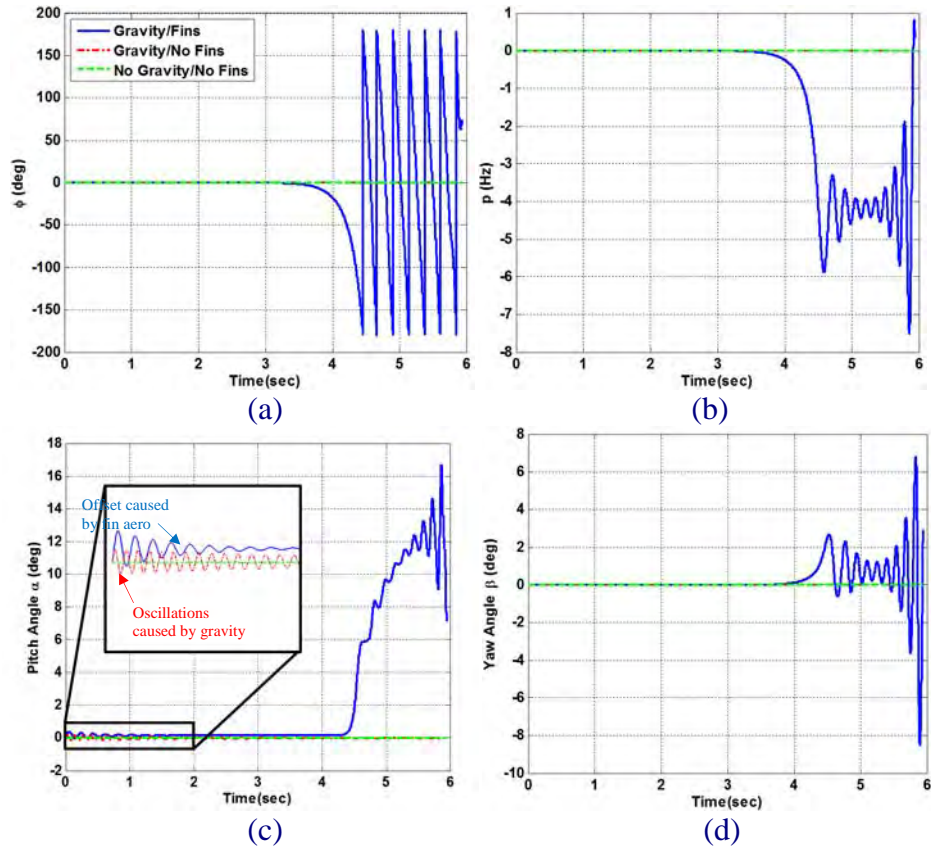
Figure 6. Selected 6DOF simulation plots showing how of gravity and fin aero effects on projectile roll stability: (a) roll angle vs. time, (b) roll rate vs. time, (c) pitch angle vs. time, and (d) yaw angle vs. time.

3.5 V-tailed Fin Parametric Study

To identify possible roll-stable airframes, fin parameters were parametrically varied from the baseline fin geometry to map out roll-stability performance. These parameters include W_{fin}, L_{fin}, h, θ_v, and δ. For simplicity, the fin sweep angle was allowed to vary freely with changes in L_{fin} and W_{fin}, which is a valid assumption for the low flight speeds observed in simulation. New estimated aero predictions were computed based off of new fin geometry prior to each parametric study. The total projectile mass and inertial properties were not recalculated, however. Observations of these parametric studies are summarized below in table 2.

Table 2. Results and summary of fin parametric studies.

Fin Parameter	Trends and Observations
h	▪ Without tip-off effects, increasing the fin offset parameter from 0.0 (cal) to 0.5 (cal) (the top of the projectile) can delay roll-instabilities in flight but not eliminate them. ▪ If tip-off effects are considered, this parameter does not dampen roll-instability or promote projectile uprighting.
W_{fin}	▪ Increasing fin width from the baseline was not observed to positively affect projectile performance.
L_{fin}	▪ Increasing fin length from the baseline was not observed to positively projectile performance. Degradation due to variation of L_{fin} is not nearly as sensitive as W_{fin}.
θ_v	▪ Decreasing θ_v increases stability. For 60.0 (deg) > θ_v > 55.0 (deg), roll-stable, naturally uprighting airframes were observed. ▪ Increasing h and decreasing δ both increased the θ_v roll-stable window form 55.0 (deg) up to approximately 75.0 (deg).
δ	▪ There exists a range (from -1.0 (deg) to -3.5 (deg)) for which the fin cant angle can be adjusted to make the V-tail appear to be roll-stable throughout flight but no naturally uprighting airframes were observed, especially in the presence of tip-off effects. ▪ As the fin can angle increases, the steady state aerodynamic angle-of-attack increases twice as much.

3.6   Roll-Stable Projectile Flight Characteristics

Given the knowledge obtained from the parametric studies, several different fin geometries were simulated to determine roll-stable airframes. As previously discussed, airframes were determined to be naturally uprighting and roll-stable if, for any set of tip-off conditions, the Euler roll angle was observed not to fall into the common cyclic rolling motion but, instead, oscillate in a dampening fashion about the upright orientation of $\phi = 0.0$ (deg). Additionally, the robustness of a roll-stable airframe is assessed by simulating projectile fly-outs for varying tip-off intensities and directions.

Figure 7 shows results of a tip-off analysis for a roll-stable configuration. The trajectory results in figures 7(a)–7(b) show that tip-off effects influence lateral displacement of the projectile, but that altitude trajectory is virtually unchanged. Figures 7(d) –7(e) show Euler angles, where figure 7(b) is the projectile roll rate. The roll rate is observed to mitigate tip-off effects very early into flight and remains very low through the remainder of flight. As a result, the roll angle oscillations are reasonably small and centered about $\phi = 0.0$ (deg) – the upright position. Tip-off

variation does appear to affect the yaw angle in figure 7(e) but not the pitch angle in figure 7(f). Figures 7(g)–7(h) show that all projectile aerodynamic angles dampen throughout flight, which is favorable. Since gravity is a known source of potential energy, the roll rate and angle plots indicate that the fin aero has a damping effect in the roll plane for certain fin configurations. Thus, naturally uprighting, roll-stable projectile airframes can exist.
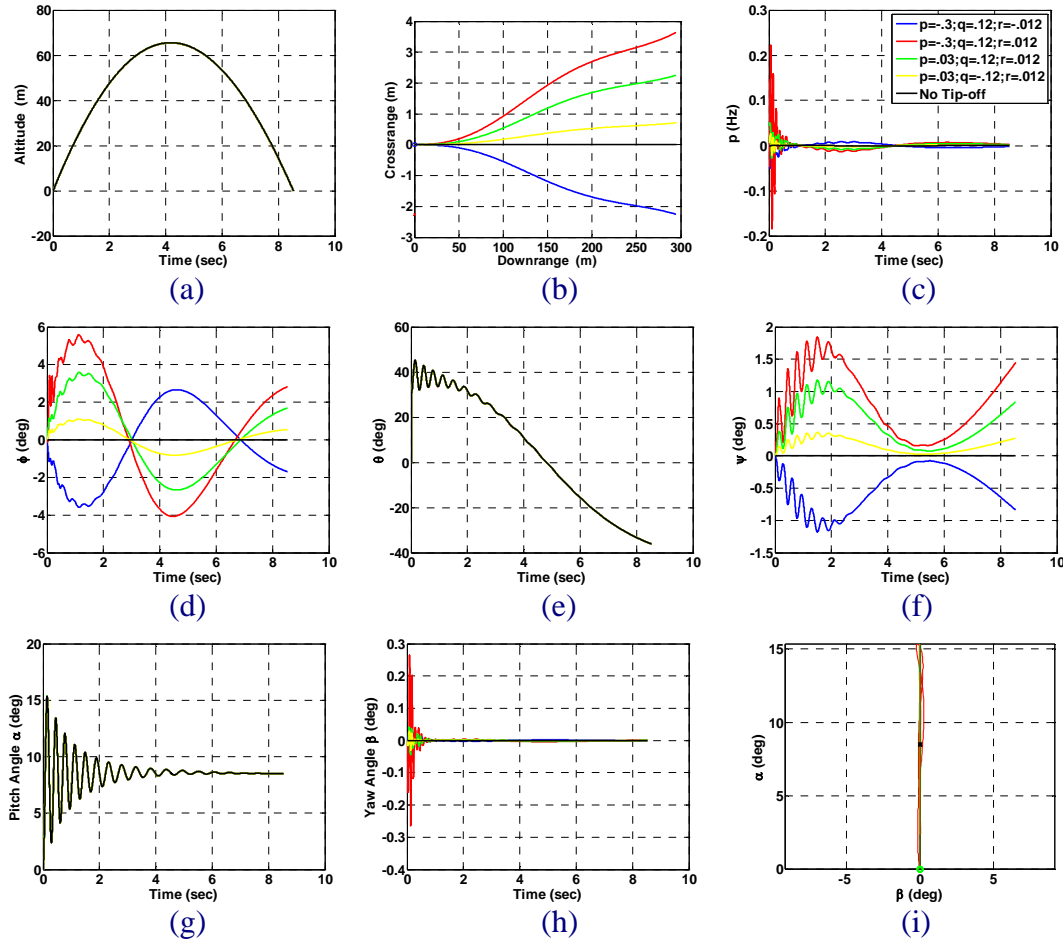
Figure 7. Selected 6DOF simulation plots of a roll-stable V-tailed projectile for varied tip-off conditions including including (a) altitude vs. time, (b) deflection vs. time, (c) roll rate vs. time, (d) roll angle vs. time, (e) pitch angle vs. time, (f) yaw angle vs. time, (g) pitch aerodynamic angle-of-attack vs. time, (h) aerodynamic angle of sideslip vs. time, and (i) pitch angle vs. angle of sideslip.

4.   Conclusion

This research indicates that naturally uprighting, roll-stable airframes can exist with favorable flight characteristics and should be considered further for possible implementation in precision-guided applications. Roll-instabilities observed in flight experiments for a chosen baseline

airframe were able to be computationally reproduced, where fins were modeled as flat surfaces. Next, fin parameters were varied from the baseline airframe to determine how each affects projectile performance. Increasing the h positively affected the roll-stability positively, but with limited influence when tip-off was introduced. Increasing both W_{fin} and L_{fin} were not observed to encourage roll stability; however, θ_v and δ were both observed to significantly promote roll-stability within certain limited regions. Using these trends, several roll-stable airframes were able to be simulated. Further, some roll-stable airframes were observed to be fairly robust to variation in tip-off effects. Conclusions of this study are based on aero-prediction techniques and rigid 6DOF trajectory simulation.

5. Future Work

A second round of flight experiments is currently being performed to demonstrate and confirm simulations that naturally upright roll-stable airframes exist. Upon successful flight testing, there are several directions that could be explored. For example, a more sophisticated test rig could be developed for more useful results (i.e., better 6DOF validation, etc.). Also, 6DOF simulations using control mechanisms could be developed to determine projectile controllability and corresponding flight characteristics while under control. Further attention should also be invested into obtaining better aero-predictions using coupled CFD-6DOF methods proposed by Sahu (*6*), so that complicated flow effects such as fin shadowing and flow separation can be accounted.

6. References

1. McCoy, R. L. *Modern Exterior Ballistics*; Schiffer Publishing Ltd., Atglen, PA, 1999.

2. Carlucci, D.; Jacobson, S. *Ballistics: Theory and Design of Guns and Ammunition*; CRC Press, Boca Raton, Florida, 2008

3. Costello M.; Anderson D. Effect of Internal Mass Unbalance on the Terminal Accuracy and Stability of a Projectile. AIAA Paper 1996, *AIAA Flight Mechanics Conference*, San Diego, California, 1996.

4. Costello, Mark. personal communication, Georgia Institute of Technology, Aberdeen, MD, June 2009.

5. Costello, Mark. *BOOM*, 6DOF Fortran Code.

6. Sahu, Jabaraj. Numerical Computations of Dynamic Derivatives of a Finned Projectile Using a Time-Accurate CFD Method. AIAA Paper 2007-6581.

INTENTIONALLY LEFT BLANK.

U.S. Army Research Laboratory
SUMMER RESEARCH TECHNICAL REPORT

Design of Biological/Synthetic Hybrid Material Approaches for Army Applications

JAMIE HUANG
JOSEPH L. LENHART AND RANDY A. MROZEK
MACROMOLECULAR SCIENCE AND TECHNOLOGY BRANCH, RDRL-WMM-G,
WEAPONS AND MATERIALS RESEARCH DIRECTORATE, BLDG 4600

Contents

List of Figures

Abstract

Integration of synthetic and biomaterials into novel hybrid systems has potential utility in a variety of Army applications. Chitosan is a biocompatible and biodegradable material that can be produced in large quantities. This project focuses on exploring alternative coupling methods and chemistries for chitosan functionalization. As a proof-of-principle, chitosan is being grafted with polyethylene glycol (PEG), polypropylene oxide (PPO), or dodecane to alter the pure chitosan wettability. Preliminary Fourier transform infrared spectroscopy (FTIR) results and contact angle measurements provide contradictory data regarding the degree of functionalization. This contradiction is currently being explored through repeated experimentation and may be due to the preferential segregation of low surface tension groups to the air interface during film casting. Angle-resolved x-ray photoelectron spectroscopy (XPS) and synchrotron near edge x-ray absorption fine structure (NEXAFS) will be explored to examine the surface chemistries.

Acknowledgments

I wish to acknowledge the mentorship of Dr. Joseph L. Lenhart and Dr. Randy A. Mrozek.

INTENTIONALLY LEFT BLANK.

1. Introduction/Background

The incorporation of controlled functionality of synthetic chemistries into biological systems has the potential to impact a variety of Army-relevant applications including tissue scaffolding, chemical or biological decontamination, battlefield wound treatment, and environmental remediation. A key aspect of many of these applications is the ability to tailor the interaction of the hybrid material to its intended environment. For example, the synthetic material could illicit a response to a specific analyte, such as for controlled release of a therapeutic agent or chemical countermeasure. Conversely, the tailored interaction could selectively sequester a specific species to aid decontamination. In most of these applications, a biologically compatible material is desirable so that there is minimal impact on the biological system.

A promising biocompatible scaffold material is chitosan. Chitosan is a deacetylated form of chitin, which is a material found in the shell of many crustaceans. Chitosan is one of the most abundant biodegradable materials, making it an excellent candidate for use in sensitive biological environments. Additionally, its abundance potentially allows any developed technology to scale-up to useful quantities while maintaining a low cost. Chitosan is a linear polysaccharide composed of D-glucosamine and N-acetyl-D-glucosamine (figure 1). Due to its polyglucosamine structure, which is a common dietary fiber similar to cellulose, chitosan is generally considered safe for human consumption (*1*).
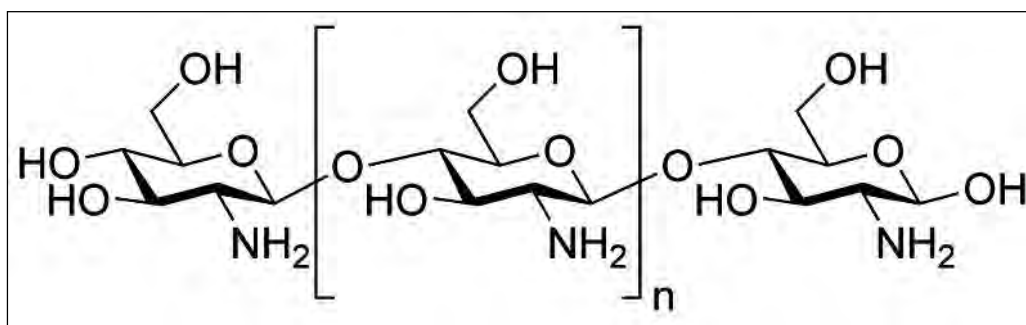
Figure 1. Chemical structure of chitosan.

Chitosan's chemical structure contains both hydroxyl and amine functionalities that can be used for modification with synthetic molecules. The focus of this project is to change the hydrophobicity/hydrophilicity of chitosan, primarily monitored by contact angle. When a water droplet is placed onto a substrate, it forms a bead; the bead's shape is dependent on the interaction between the water and the surface. By modifying the surface with a hydrophilic material, the surface becomes attracted to water and decreases the contact angle. In contrast, a hydrophobic modification would make the newly functionalized surface repel water and the contact angle would increase. This effect is most commonly observed during the process of

waxing a vehicle; the addition of the hydrophobic wax causes the water to bead up and roll off the car. This project explores a range of possible combinations of hydrophobic and hydrophilic polymer attachments to chitosan as a means of controlling the wettability, adhesion, and solubility in various media.

Three polymer materials were evaluated for their impact on wettability when coupled with chitosan. Polyethylene glycol (PEG) is a hydrophilic polymer that is commonly used in biological environments including therapeutics, personal hygiene products, and biological implant coatings. It is soluble in water partially due to its ability to form hydrogen bonds (figure 2a). Polypropylene oxide (PPO) is very similar to PEG except it has an additional methyl group attached to the molecule (figure 2b). This subtle change to the polymer backbone is enough to disrupt the hydrogen bonding character of the polymer and dramatically change its water solubility. Dodecane consists of a long carbon chain that exhibits a high degree of hydrophobicity due to the large number of methylene groups present (figure 2c).

(a) (b) (c)
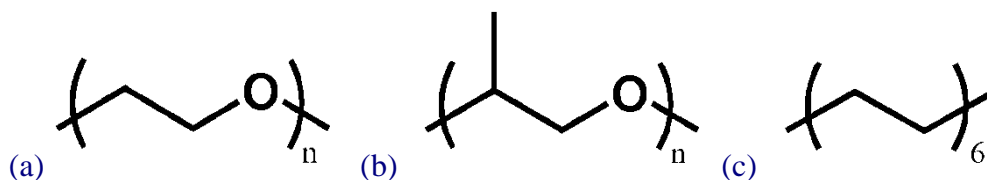
Figure 2. Chemical structures of (a) polyethylene glycol, (b) polypropylene oxide and (c) dodecane.

To alter the wettability and adhesion of chitosan, the hydrophobic and hydrophilic materials must be functionalized onto chitosan so that the chemistry of hybrid material changes. A major drawback of chitosan is its lack of solubility in most solvents, including water, making it extremely difficult to modify chitosan's chemistry. To obtain an aqueous solution of chitosan, the water must be acidic, limiting the available chemistries for coupling (*2*). As a result, the chitosan has been functionalized to enhance its solubility in various solvents. Chitosan functionalization has been attempted through a variety of synthetic approaches (*2*). These approaches typically require complex synthetic methodologies to obtain a large fraction of coupling on the chitosan backbone. For this project, it may not be necessary to obtain a high degree of coupling if a critical degree of functionalization can be identified that produces the required property changes.

The main focus of this project is to determine the viability of alternative reaction conditions for the functionalization of chitosan to ultimately alter its wettability. The amine group on the chitosan is a candidate for a simple Michael addition by reacting with a carbon-carbon double bond. The Michael addition is facilitated by a methyl methacrylate terminated-PEG (figure 3). The amine group can also react with an epoxy functionalized polymer. The epoxy-amine is a robust reaction found in many commercially available adhesives. This reaction is initially investigated using a mono-functional epoxy dodecane, but can be extended to epoxy-functionalized PEG if the results are promising (figure 3).

188
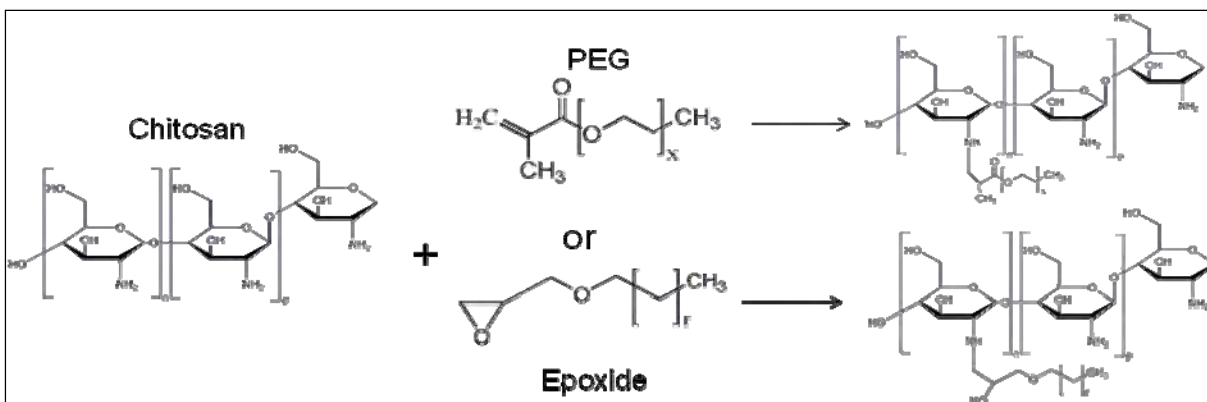
Figure 3. PEG or epoxy dodecane functionalize chitosan by reacting with chitosan's amine group.

For many of the potential applications, a solution of dispersed chitosan will hinder the ability to effectively deploy or contain its intended target. As a result, the project also investigates the ability to use the previously described chemistries to attach the modified chitosan to scaffolding materials with useful geometries. For example, the epoxy chemistry has been implemented into the production of foam materials that have a large surface area. In addition, the modified chitosan can be placed onto a monolithic material to enhance the barrier properties. It is anticipated that these approaches can be readily scaled-up to accommodate current U.S. Army needs.

2. Experimental Setup

2.1   Chitosan Functionalized with PEG

Using similar protocols found in the literature, 2% chitosan solutions were dissolved in acidified water using 0.2% acetic acid. PEG was then added into the solution; the amount of PEG was one of the following: 25%, 50%, or 75% by weight of chitosan in the solution. Blends of the two components were created by mixing the solutions for an hour and then directly casting the solutions into silicon molds. Reacted solutions were also made by constantly stirring the mixture at 60 °C and 500 rpm for 4 h under nitrogen atmosphere (*3*). Alternatively, 1% chitosan/2.0% acetic acid solutions with the same amounts of PEG were produced. The solutions were constantly stirred at 60 °C and 500 rpm for 4 h under nitrogen atmosphere.

All PEG samples were washed with the following method, except the 2% chitosan PEG blends. First, 10% w/w sodium hydroxide (NaOH) was used to precipitate the polymer out of the solutions. The obtained polymer was submerged in methanol and centrifuged to remove any unreacted molecules (*3*). This washing protocol was repeated three times, producing a

189

condensed pellet. The pellet was then redissolved into acidified water and cast into silicone molds to form thin films used for contact angle measurements and Fourier transform infrared spectroscopy (FTIR).

2.2 Chitosan Functionalized with PPO

Various amounts of PPO (25%, 50%, and 75% by weight of chitosan) were stirred into 2% chitosan/0.2% acetic acid solutions for 1 h to create 2% chitosan/PPO blends. Additionally, 1% chitosan/2.0% acetic acid solutions were also mixed with 25%, 50%, and 75% PPO at 1000 rpm and room temperature for approximately 24 h.

2.3 Chitosan Functionalized with Epoxy Dodecane

At this point, 1% chitosan solutions were dissolved in 30% acidified water, using 0.2% acetic acid, and 70% ethanol. Then, 50% epoxy dodecane (half of the weight of chitosan) was added into the chitosan solution. The solutions were constantly stirred at 90 °C and 500 rpm for 4 h under nitrogen atmosphere. The same NaOH washing protocol was used to extract the polymer and cast it into films.

3. Results/Discussion

3.1 Pure Chitosan

Contact angle measurements were used to quantify the wettability of the chitosan-functionalized films. The instrument places a precise droplet of water onto the substrate, i.e., chitosan, and is equipped with a camera to capture the droplet and measure the contact angle. Pure chitosan exhibits a contact angle of 110° as seen in figure 4.
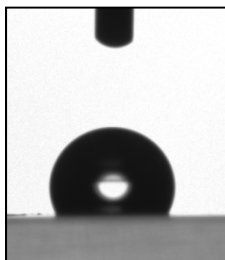
Figure 4. Contact angle of pure chitosan (110°).

FTIR was used to monitor the extent of chitosan with the desired coupling agent. FTIR measures the absorbance of the material at a range of wavelengths that can be assigned to specific functional groups. Figure 5 contains a typical FTIR scan of a pure chitosan film. The key peaks include the amine functionality at 1600 cm^{-1} and the carbon-hydrogen (carbogen) bond stretching around 2900 cm^{-1}.
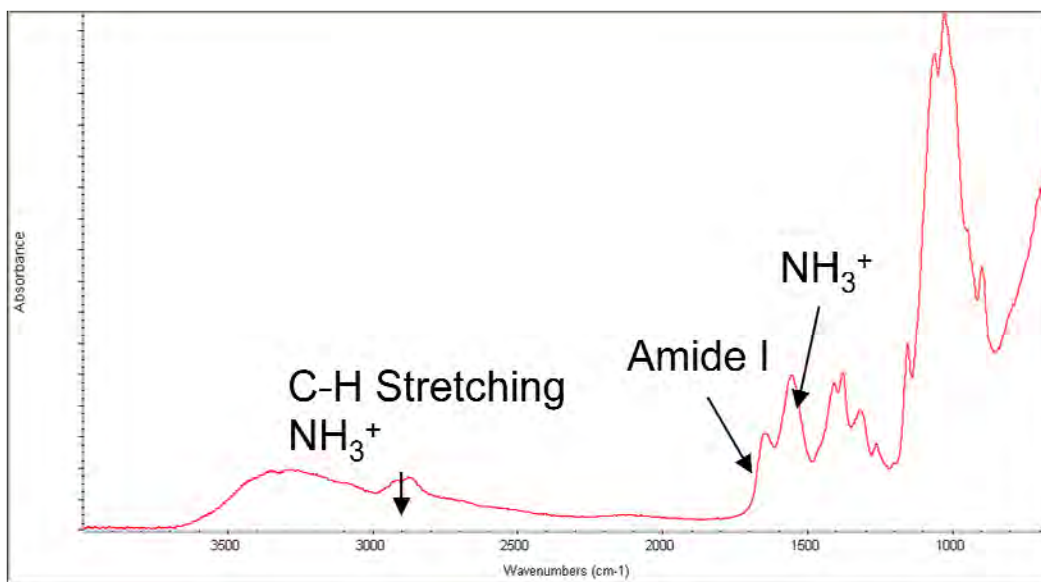
Figure 5. FTIR scan for pure chitosan with carbon-hydrogen bond stretching occurring around 2900 cm^{-1} and amine groups around 1600 cm^{-1}.

3.2   PEG Samples

3.2.1 2% Chitosan/0.2% Acetic Acid Samples

To determine the approximate amount of PEG required to alter the hydrophilicity of chitosan, films consisting of chitosan-PEG blends were produced where the two components were mixed but not reacted. The 2% chitosan blends revealed a significant change in contact angle with the addition of PEG. Samples containing 25% PEG and 50% PEG samples exhibited significant increases in hydrophilicity with contact angles of 39.33° ± 3.93° (Figure 6a) and 31.96° ± 9.34° (figure 6b), respectively. In contrast, the 75% PEG blend became more hydrophobic, with a contact angle of 87.79° ± 15.74° (figure 6c).

(a)   (b)   (c)
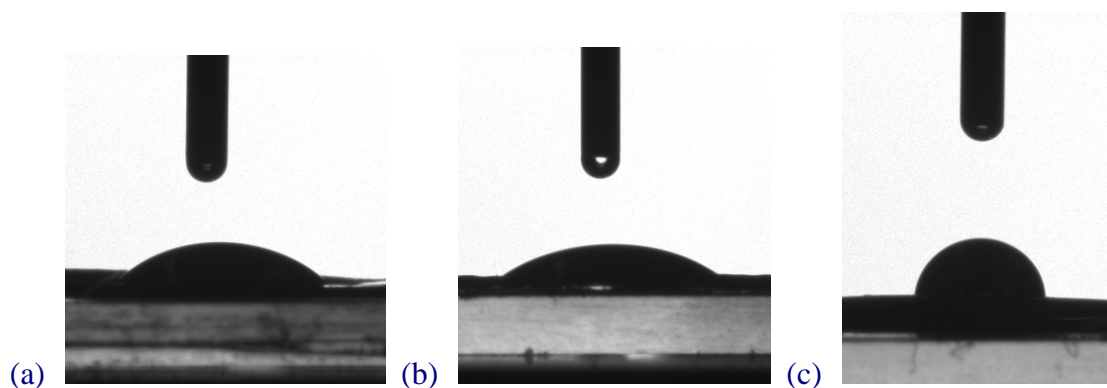
Figure 6. Contact angle of 2% chitosan/0.2% acetic acid and a (a) 25% PEG blend (39°), (b) 50% PEG blend (32°), and (c) 75% PEG blend (88°).

191

The FTIR scans of the three blends support the presence of PEG in the samples (figure 7). The PEG carbon-oxygen double bond (carbonyl) peak is present at around 1710 cm^{-1}. In addition, the peak around 2900 cm^{-1} increases due to the additional hydrocarbons in the PEG backbone. The peak areas are also consistent with the PEG concentration in the blends where an increasing PEG concentration leads to an increased peak area. The increased PEG concentration in the films produces a contact angle decrease when the concentration of PEG in the blend increases from 25% PEG (39°) to 50% PEG (32°). However, the FTIR does not indicate why the blend containing 75% PEG would exhibit a decreased hydrophilicity. It is possible that the high PEG concentration leads to phase separation and inconsistencies in the film with regions of high and low PEG content, which may explain the large standard deviation. It is also possible that the higher concentration leads to a preferential segregation of low surface tension groups to the air interface during film casting. To fully explore these possibilities, angle-resolved x-ray photoelectron spectroscopy (XPS) or synchrotron near edge x-ray absorption fine structure (NEXAFS) could be used to examine the surface chemistries.
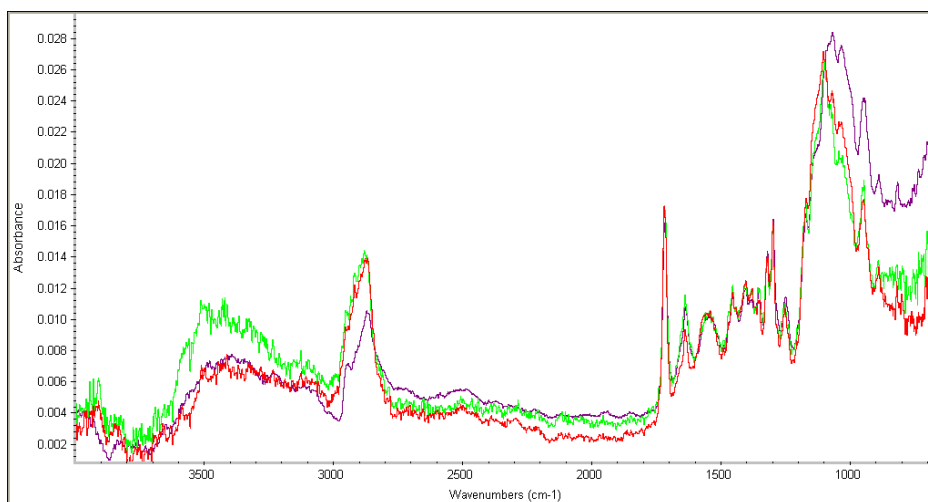
Figure 7. FTIR scans of the 2% chitosan/0.2% acetic acid and 25% PEG (purple), 50% PEG (green), and 75% PEG (red).

To covalently attach the PEG, the sample mixtures were heated to 60 °C to react for 4 h. The samples were thoroughly washed to remove any unbound PEG prior to FTIR analysis. As a result, the presence of carbonyl and increase of the carbon-hydrogen peaks indicates that the PEG is covalently bonded or strongly attached to the chitosan.

In the 2% chitosan/0.2% acetic acid mixtures containing 25% and 75% PEG, no carbonyl peak around 1710 cm^{-1} was present (figure 8a and 8b, respectively). This indicates that the Michael's addition reaction did not occur, and that after the washing, all that remained was pure chitosan. Additionally, both samples had approximately the same contact angle results as pure chitosan with angles of 109° (figures 9) and 104°, respectively, indicating that the reaction did not occur.
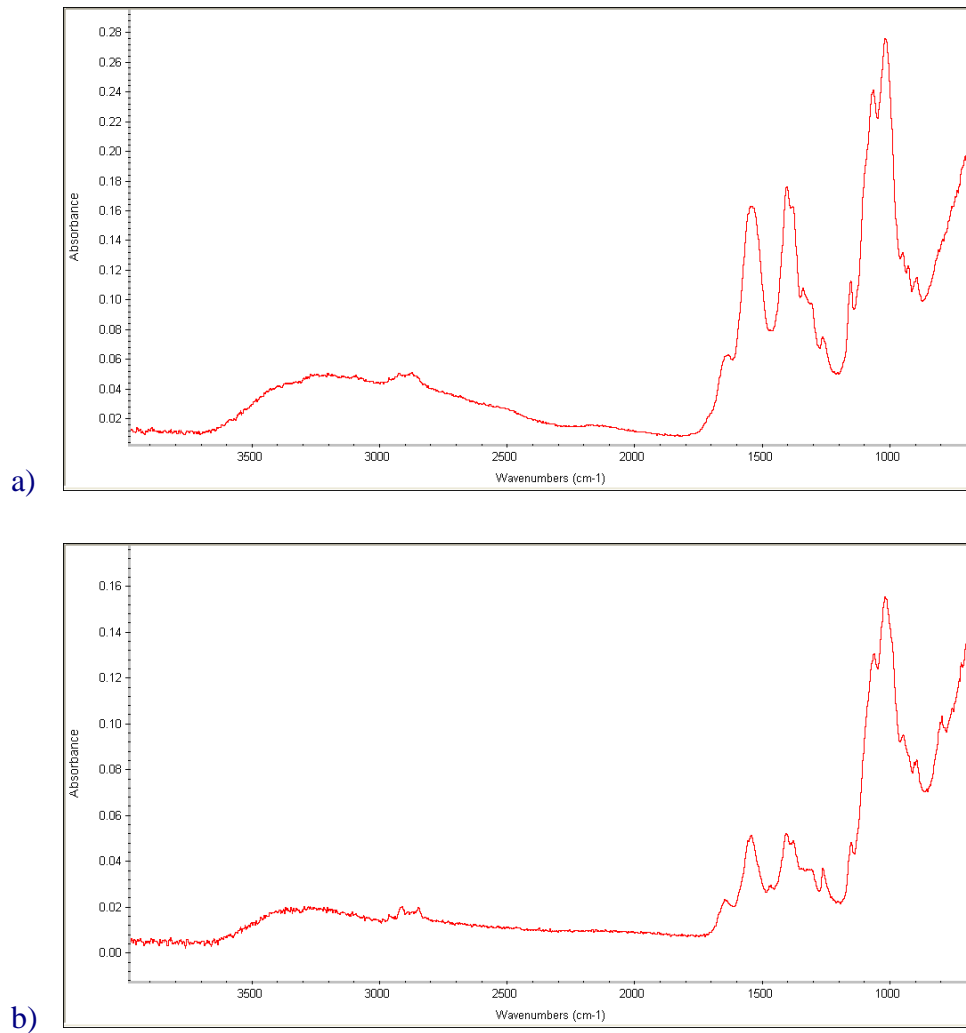
Figure 8. FTIR scans of 2% chitosan/0.2% acetic acid and (a) 25% PEG and (b) 50% PEG illustrating the similarity between the 25% and 50% samples and pure chitosan.
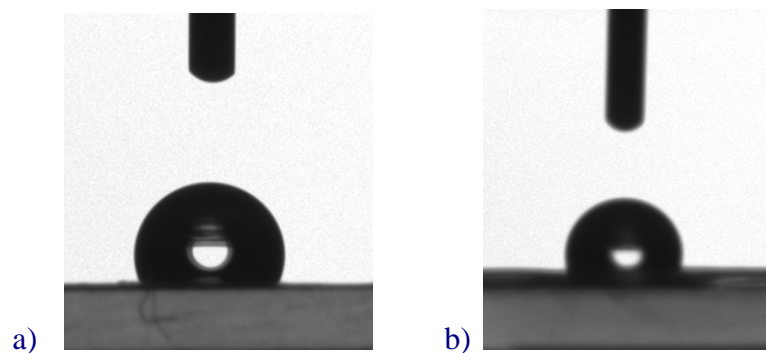
Figure 9. Contact angles of 2% chitosan/0.2% acetic acid and (a) 25% PEG (109°) and (b) 50% PEG (104°).

3.2.2 1% Chitosan/2.0% Acetic Acid Samples

As received, some of the amines on the chitosan are acetylated, resulting in decreased solubility and reactivity. The addition of the acid deacetylates the chitosan, enhancing the water solubility. As with the functionalization, there is likely a critical concentration of acid required for solubility that does not require a large degree of deacetylation. It is possible that at this critical acid concentration the chitosan is soluble but largely nonreactive.

To determine the impact of acid concentration, the chitosan solution concentration was decreased to 1% and the acetic acid concentration was increased to 2.0%. The solutions were reacted with 25%, 50%, and 75% PEG, respectively. All three samples exhibited a decrease in the contact angle, indicating PEG was present in the samples. The 25% PEG sample had a contact angle of 51.32° ± 9.05°, the 50% PEG sample had 18.55° ± 9.24°, and the 75% PEG sample had less than 10.93° (figures 10a, 10b, and 10c, respectively). The 75% PEG sample had droplets of water that absorbed too quickly onto the surface of the film and could not be measured precisely. An increase in the hydrophilicity trend of all three samples suggests that there is a linear relationship between the concentration of PEG and the degree of PEG coupling to chitosan.

a)   b)   c)
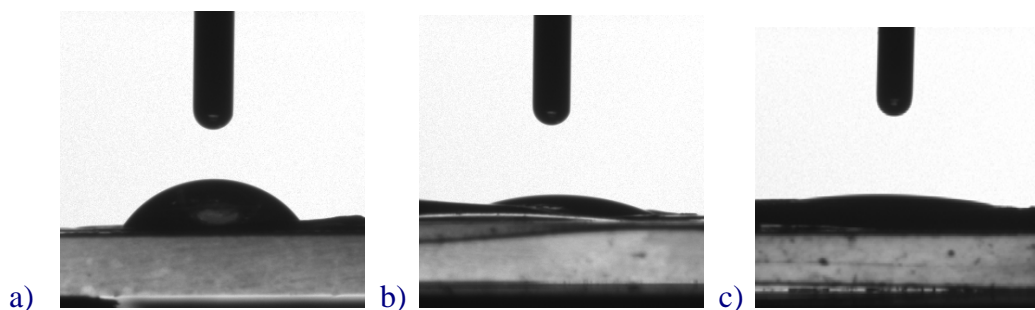
Figure 10. Contact angles of 1% chitosan/2.0% acetic acid and (a) 25% PEG (51°), (b) 50% PEG (19°), and (c) 75% PEG (11°).

The decrease in contact angle, relative to the previous samples, may be attributed to the dilution of the chitosan, the increased acid concentration, or a cooperative impact. The chitosan dilution may lead to a reduction in the steric hindrance of neighboring chitosan molecules, allowing the PEG to react more quickly. However, it is anticipated that even the more concentrated solution would have exhibited some change in contact angle at the highest PEG concentration. The potential cooperative impact of chitosan dilution and increased acid concentration will be explored by performing the experiments using a 2% chitosan solution in 2% acetic acid.

FTIR scans of the samples support the results of the contact angle measurements (figure 11). The samples containing 50% and 75% PEG samples show an increase in the carbonyl peak and carbon-hydrogen stretching peak with increasing peak area. However, the carbon-hydrogen stretching peak shape changes at 75% PEG. In addition, the sample containing 25% PEG does exhibit any significant changes from the pure chitosan scan despite a major change in contact angle. This data may indicate the limitations of FTIR for this analysis. It is possible that the PEG

concentration required to alter the contact angle is below the detectable limit of FTIR. The ability to detect the PEG in low concentration may also be limited by sample geometry as the signal is dependent on the film placement during FTIR and the contact area between the FTIR crystal and the film.

Furthermore, it is counterintuitive that the contact angle would be reduced during the covalent addition of the PEG relative to the blends as the reaction did not likely result in a quantitative yield. It is possible that this is the result of increased deacetylation of the chitosan due to the increase acid concentration. The reduced ability of the low surface tension groups to segregate to the air interface during film casting might also be another factor. This concept can also be explored using angle-resolved XPS and synchrotron NEXAFS to examine the surface chemistries.
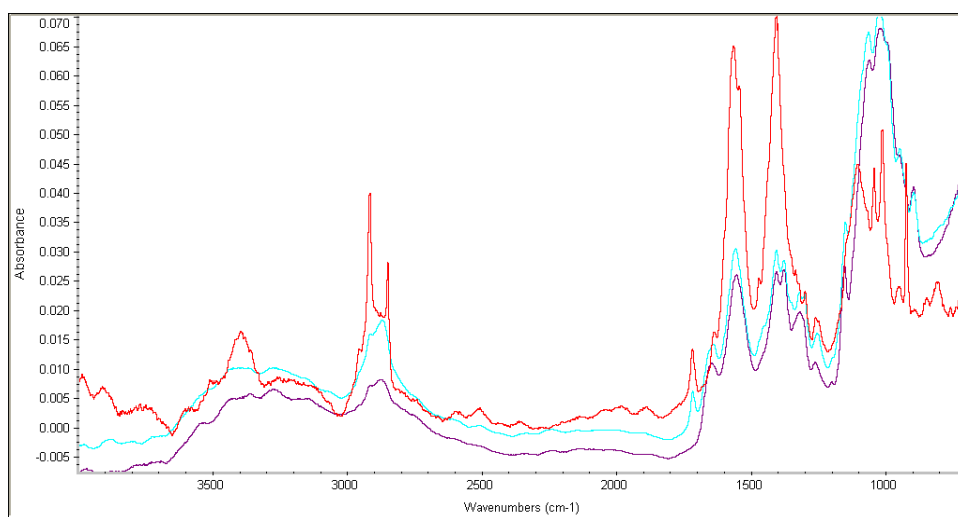
Figure 11. FTIR scans of 1% chitosan/2.0% acetic acid and 25% PEG (purple), 50% PEG (blue), or 75% PEG (red).

3.3   PPO Samples

3.3.1 2% Chitosan/0.2% Acetic Acid Samples

To determine the potential impact of PPO on the hydrophilicity of chitosan, films consisting of chitosan-PPO blends were produced where the two components are mixed but not reacted. All three concentrations of PPO exhibited similar decreases in contact angle. The 2% chitosan/0.2% acetic acid/25% PPO sample had a contact angle of $34.25° \pm 5.44°$ (figure 12a), the 50% PPO sample had $34.08° \pm 9.59°$ (figure 12b), and the 75% PPO blend had $31.24° \pm 10.05°$ (figure 12c). Similarly, the FTIR scans of the three samples closely align, as seen in figure 13, with an increase in the carbon-hydrogen stretching at 2900 nm^{-1}. This indicates that PPO has the maximum impact at 25% loading and there is no added benefit to higher concentrations.
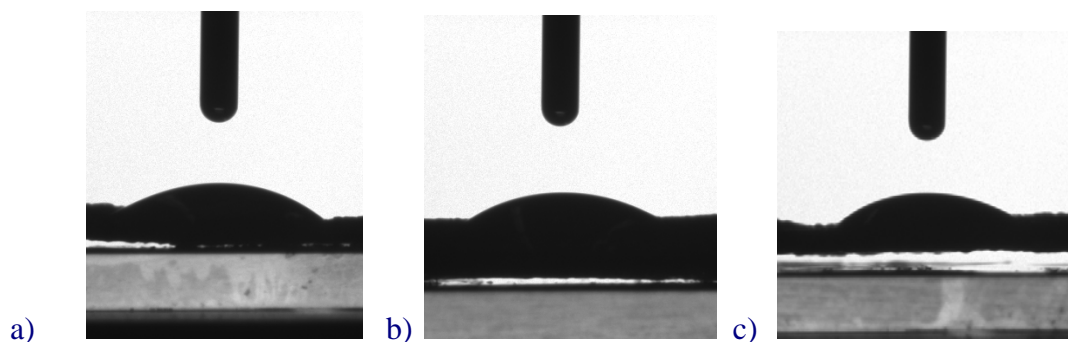
Figure 12. Contact angles of 2% chitosan/0.2% acetic acid and (a) 25% PPO (34°), (b) 50% PPO (34°), and (c) 75% PPO (31°).
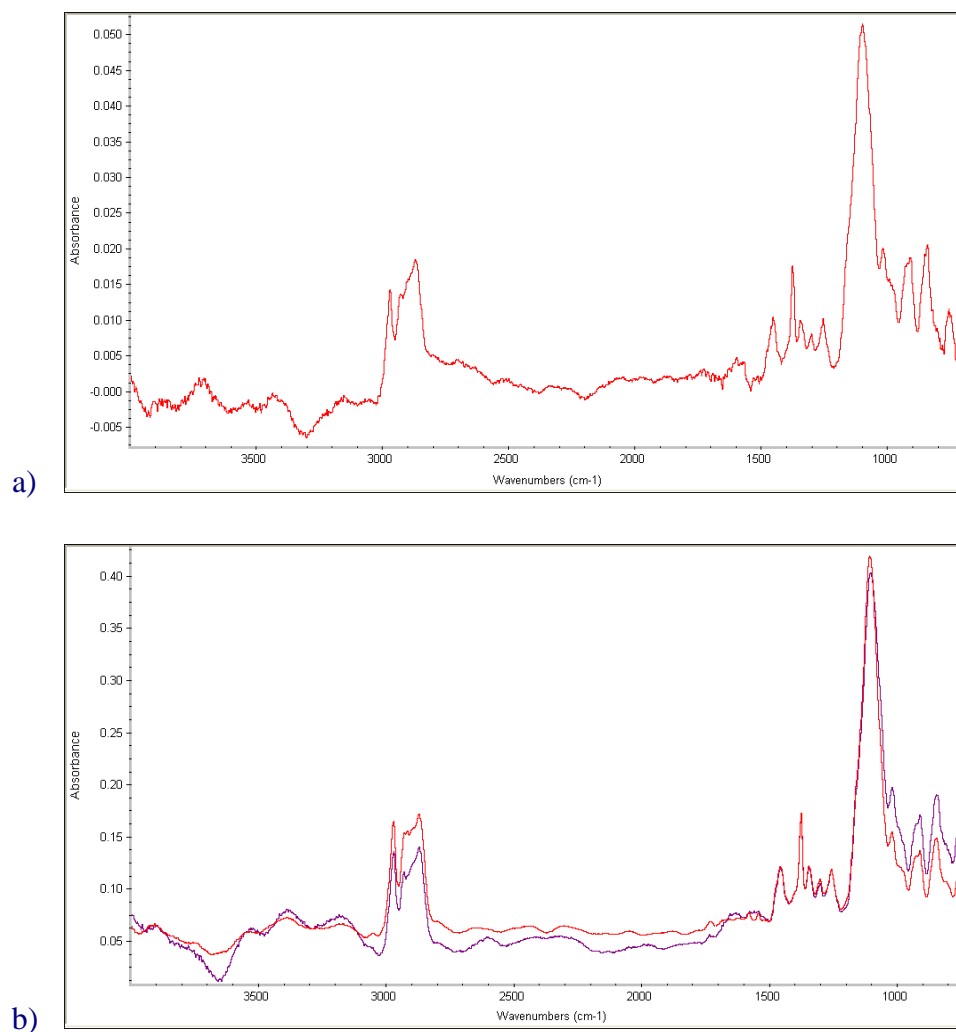
Figure 13. FTIR scans of 2% chitosan/0.2% acetic acid blends with (a) 25% PPO and (b) 50% PPO (red) and 75% PPO (purple).

3.3.2 1% Chitosan/2.0% Acetic Acid Samples

Next, 1% chitosan/2.0% acetic acid samples were created to see if there was variability in the wettability depending on the concentration of acid or chitosan. All three samples had a decrease in hydrophobicity; as seen in figure 14, the 25% PPO sample had a contact angle of 48.84° ± 21.67°, while the 50% PPO and 75% PPO samples exhibited a contact angle less than 10°, but they could not be precisely measured.

a)   b)   c)
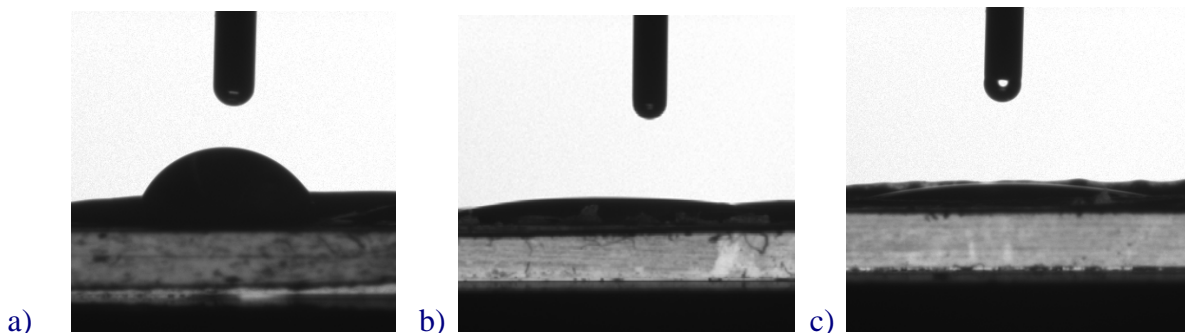
Figure 14. Contact angles of 1% chitosan/2.0% acetic acid and (a) 25% PPO (49°), (b) 50% PPO (<10°), and (c) 75% PPO (<10°).

The FTIR results shown in figure 15 indicate that the three samples had similar amounts of PPO in each sample. This result may further support that there are some limitations of FTIR for this project. While the FTIR does not exhibit any difference between the samples, the contact angle demonstrates the anticipated trend. Future work will be done to explore the viability of using nuclear magnetic resonance (NMR) to determine the extent of functionality. NMR analysis also has some significant challenges in regards to sample preparation—it is a solution technique rather than using the solid film samples employed in FTIR.
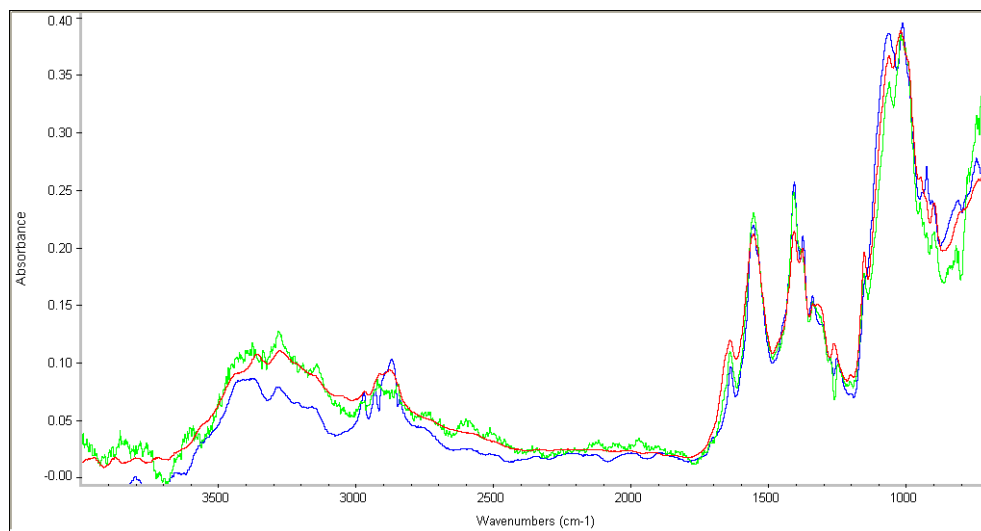
Figure 15. FTIR scans of 1% chitosan/2.0% acetic acid and 25% PPO (green), 50% PPO (red), and 75% (blue).

3.4 Epoxy Dodecane Samples

The initial epoxy dodecane reaction consisting of 1% chitosan in 0.2% acetic acid and 50% epoxy dodecane increased the hydrophilicity to 84.42° ± 6.49° (figure 16). This contradicts the theory that epoxy dodecane would make chitosan more hydrophobic because epoxy dodecane contains an excessive amount of hydrophobic methylene groups in its backbone. Additionally, the FTIR scan did not show any indication of epoxy dodecane present in the sample, as there is no change from its FTIR scan and that of pure chitosan (figure 17). The ring opening reaction for the epoxy dodecane may not have occurred if the energy in the system was not sufficient to jumpstart the reaction. In addition, the epoxy dodecane is not soluble in the acidified water and requires 70% ethanol to form a uniform mixture. While the chitosan does remain in solution, it is unclear what impact the ethanol has on the reactivity. As a result, the reaction temperature and time may have to be modified. In addition, these experiments need to be reproduced using the lower chitosan concentration and increased acid concentrations that have shown promise in previously described experiments.
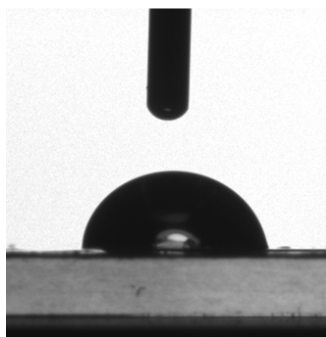
Figure 16. Contact angle of 1% chitosan/0.2% acetic acid /50% epoxy dodecane (84°).
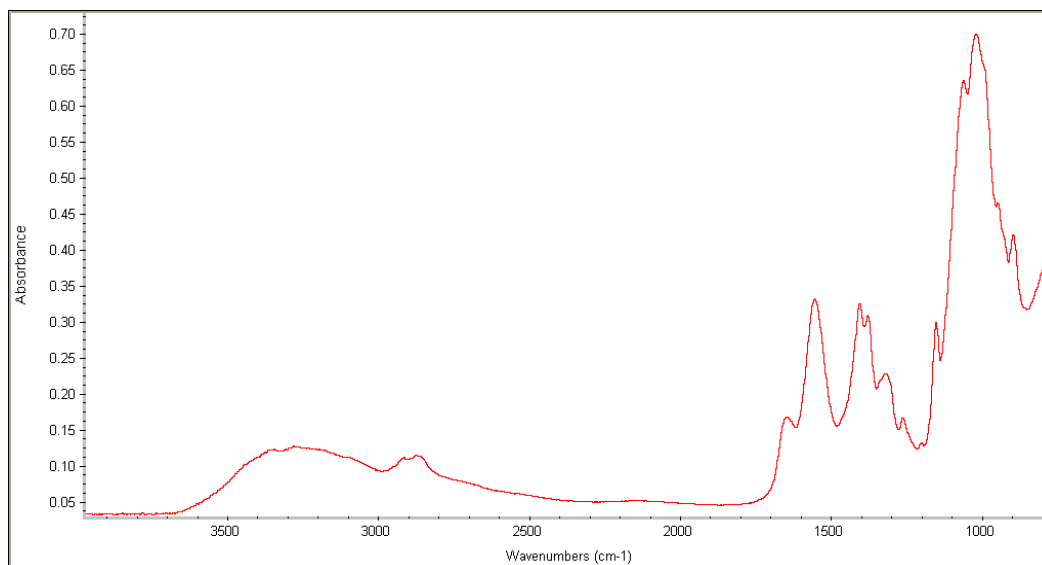
Figure 17. FTIR scan of 1% chitosan/0.2% acetic acid/50% epoxy dodecane, which has no differences compared to pure chitosan.

4. Summary/Conclusions

At this point in the project, the important experimental parameters are beginning to become apparent but will require further study to be conclusive. From the contact angle data, the acid concentration of the chitosan solution is very important. An acetic acid concentration that is too low will solubilize the chitosan but appears to hinder the chitosan reactivity. However, an increased acid concentration will enhance the reactivity, leading to significant changes in the contact angle. In many cases, FTIR supports the presence of chemical modifications but is not always quantitative. This is most prevalent at low functional densities where FTIR does not exhibit a chemical change in contrast to a large change in contact angle. This indicates that FTIR may not be the best tool to monitor the coupling reaction. Other methods for monitoring the reaction including NMR and thin layer chromatography (TLC) are currently being explored.

While the changes are apparent in the modified chitosan contact angle, there are a few inconsistencies that require further experimentation. Contrary to the anticipated outcome, the PPO exhibited a lower contact angle than PEO. We anticipate that this is due to the PPO being di-functional. In the presence of water, the unreacted epoxy ring will open, resulting in a hydroxyl termination. The ability of the hydroxyl group to hydrogen bond with the water may lead to the decreased contact angle. Depending on the ring opening timescale, it is possible that the blends still exhibited epoxy functionality leading to an increased contact angle (~30°). To determine the impact of the end group, a polymer with increased chain length can be used to minimize the impact of the end group. In addition, the impact of acid concentration and chitosan dilution needs to be further explored to identify optimum conditions.

In the near future, we will also explore the development of functional scaffold materials, including epoxy foams and soft polymer monoliths. One option is to couple the chitosan with glutaraldehyde, another common biocompatible material, which will effectively cross-link the chitosan, producing a polymer gel. These materials can then be further functionalized to provide specific interactions depending on the application. We anticipate that these methods can be readily tailored, scaled up, and implemented into a variety of Army applications.

5. References

1. Knorr, D. *Food Technology* **1991**, *45*, 114–122.

2. Macquarrie, D. J.; Hardy, J.J.E. *Industrial & Engineering Chemistry Research* **2005**, *44*, 8499–8520.

3. Radhakumary, C.; Prabha, D. N.; Reghunadhan, N.; Mathew, S. *Journal of Applied Polymer Science* **2004**¸ *114*¸ 2873–2886.

INTENTIONALLY LEFT BLANK.